

THESIS

CRITICAL STATE, DILATANCY AND PARTICLE BREAKAGE  
OF MINE WASTE ROCK

Submitted by

Zachary P. Fox

Department of Civil & Environmental Engineering

In partial fulfillment of the requirements

for the Degree of Master of Science

Colorado State University

Fort Collins, Colorado

Summer 2011

Master's Committee:

Advisor: J.A.H. Carraro

Charles D. Shackelford

Thomas Borch

Daniel D. Overton

Copyright by Zachary Paul Fox 2011

All Rights Reserved

## ABSTRACT

### CRITICAL STATE, DILATANCY AND PARTICLE BREAKAGE OF MINE WASTE ROCK

Critical state, dilatancy and particle breakage characteristics of two mine waste rock (*MWR*) materials were systematically studied in drained isotropic and axisymmetric compression. A specimen preparation technique that simulated material dumping in the field was adopted and the technique is shown to be suitable for reconstitution of uniform and repeatable specimens of *MWR* for element testing. The *MWR* types tested were unoxidized and oxidized sedimentary argillite taken from the Ordovician Vinini formation in northeastern Nevada. Acid-base accounting results indicate that the neutralization potential (*NP*) and acid-producing potential (*AP*) values decreased for the oxidized material. Static, monotonic, isotropically compressed drained triaxial tests were performed on 150-mm-diameter, 300-mm-tall cylindrical specimens with maximum particle size equal to 25.4 mm. Laboratory particle size distributions were modeled to be parallel to the collected field gradation in order to create specimens with appropriate maximum particle sizes for the testing apparatus.

The intrinsic parameters that characterize critical-state, dilatancy and particle breakage of each *MWR* material tested were determined allowing analysis of constitutive behavior to be carried out using an appropriate theoretical framework for granular soils experiencing particle breakage during testing. While the critical state friction angles were very similar between the two *MWR* types (unoxidized =  $38.3^\circ$  and oxidized =  $36.7^\circ$ ), dilatancy is much greater in the unoxidized specimens than in the oxidized specimens. Bolton's (1986) fitting parameters  $Q$  and

$R$  were determined and values agree well with those found in the literature for geomaterials with similar stress-dilatancy behavior and grain tensile strengths. Grain tensile strength was evaluated through point load strength index testing giving values for grain tensile strength for the unoxidized material that are 10 times greater than observed for the oxidized material. Particle size distributions were determined before and after testing to evaluate particle breakage due to the combined effects of isotropic and axisymmetric compression as well as evaluate the increase in surface area due to particle breakage. The fractal dimension ( $D$ ) was evaluated before and after testing in order to assess the validity of the underlying assumptions of the modified work equation presented by McDowell et al. (1996). The surface energy of the materials tested was found to be in the range of 5-24 J/m<sup>2</sup>. All of these results indicate that *in situ* weathering may degrade the shear strength characteristics of a quarried sedimentary mine waste rockfill by weakening the intrinsic shear strength parameters of the *MWR*. The only rigorous way to properly assess the strength degradation of the *MWR* materials tested involves careful assessment of the critical state, dilatancy and particle breakage characteristics.

## ACKNOWLEDGEMENTS

The author would like to express his deepest appreciation to his loving family who made college a possibility. He will be forever indebted to Dan and Lori Fox, Gary and Beth Maschoff, Lyle and Maxine Maschoff, and John and Carol Fox for all they have done. Without their eternal love and support, none of this would have been possible.

Special thanks to Professor J.A.H. Carraro for continuous guidance and support throughout the author's studies at Colorado State University. Thanks are also extended to Professor C.D. Shackelford, Professor T. Borch, and Dan Overton for their guidance throughout the research project.

Mike Henderson, Don Runnels, Mark Williamson, J. D. Fenenga, and Clint Strachan provided essential industry insight throughout project. The program would not have been possible without their dedication and support. Funding provided by the 2008 tailings and mine waste conference organizing committee is greatly appreciated.

## TABLE OF CONTENTS

	Page
LIST OF TABLES .....	ix
LIST OF FIGURES .....	xi
LIST OF SYMBOLS .....	xvi
CHAPTER 1: INTRODUCTION .....	1
1.1 Problem Statement .....	1
1.2 Research Objectives .....	4
1.3 Research Scope .....	5
1.4 Manuscript Organization .....	5
CHAPTER 2: CRITICAL STATE, DILATANCY AND PARTICLE BREAKAGE OF MINE WASTE ROCK ( <i>MWR</i> ) .....	6
2.1 Background .....	6
2.2 Large-scale Triaxial Testing .....	6
2.2.1 Dilatancy and Critical State .....	11
2.2.2 Modeled Particle Size Distributions .....	12
2.2.3 Membrane Penetration .....	18
2.2.4 Specimen Preparation and Uniformity .....	22
2.3 Particle Breakage .....	23
2.3.1 Fractal Dimension .....	30
2.3.2 Particle Strength .....	31
2.3.3 Creep in Granular Geomaterials .....	33
2.4 Acid-base Accounting .....	35
2.5 Summary .....	37
CHAPTER 3: CONCEPTUAL FRAMEWORK .....	40
3.1 Critical State Friction Angle .....	40
3.2 Stress-Dilatancy Relationship .....	43
3.3 Particle Breakage .....	46
3.3.1 Fractal Dimension .....	49
3.3.2 Creep in Granular Geomaterials .....	53
3.4 Acid-base Accounting .....	54
CHAPTER 4: EXPERIMENTAL PROGRAM .....	56
4.1 Materials .....	56
4.2 Experimental Methods .....	58
4.2.1 Modeled Particle Size Distributions .....	59
4.2.2 Maximum and Minimum Void Ratios .....	61
4.2.3 Specific Gravity .....	61
4.2.4 Modeled Particle Size Distributions .....	62
4.2.5 Specimen Preparation and Uniformity .....	62
4.2.6 Large-scale Triaxial Testing .....	64
4.2.7 Particle Strength .....	63
4.2.8 Particle Breakage and Fractal Dimension .....	75
4.2.9 Acid-base Accounting.....	76

CHAPTER 5: RESULTS .....	78
5.1 Isotropic Compression .....	78
5.2 Drained Monotonic Loading .....	80
5.3 Particle Strength .....	87
5.4 Particle Breakage .....	87
5.5 Fractal Dimension .....	88
5.6 Acid-base Accounting .....	89
CHAPTER 6: ANALYSIS .....	91
6.1 Specimen Preparation and Uniformity .....	91
6.2 Isotropic Compression .....	92
6.3 Drained Monotonic Loading .....	94
6.4 Particle Strength .....	103
6.5 Particle Breakage .....	105
6.6 Fractal Dimension .....	106
6.7 Surface Energy .....	107
6.8 Acid-base Accounting .....	109
CHAPTER 7: CONCLUSIONS .....	111
7.1 Conclusions .....	111
7.1.1 Specimen Preparation and Uniformity .....	111
7.1.2 Drained Monotonic Response .....	112
7.1.3 Particle Breakage and Fractal Dimension .....	113
7.1.4 Surface Energy .....	114
7.1.5 Acid-base Accounting .....	115
7.2 Suggestions for Future Work .....	115
APPENDIX A: EVALUATING THE MODIFIED WORK EQUATION .....	118
APPENDIX B: PARTICLE SIZE DISTRIBUTIONS .....	123
APPENDIX C: FRACTAL DIMENSION .....	130
APPENDIX D: TRANSDUCER CALIBRATIONS .....	137
LIST OF REFERENCES .....	147

## LIST OF TABLES

- Table 4.1 Index properties for modeled particle size distributions of unoxidized and oxidized Vinini *MWR* determined by standardized ASTM procedure.
- Table 4.2 Relative density of top and bottom lifts of a “dense” oxidized *LSTX* specimen using the proposed procedure. Initial values are before application of the dummy lift and final values are after application of the third “dummy” lift.
- Table 4.3 Relative density of top and bottom lifts of a “loose” oxidized *LSTX* specimen using the proposed procedure. Initial values are before application of the dummy lift and final values are after application of the third “dummy” lift and vibration.
- Table 4.4 Summary of calibration data for instruments used as a part of the *LSTX* apparatus.
- Table 4.5 Elastic modulus determined at normal strains less than 20% for each membrane used during triaxial testing.
- Table 5.1 Results for the triaxial tests completed on unoxidized *MWR*.
- Table 5.2 Results for the triaxial tests completed on oxidized *MWR*.
- Table 5.3 Point load strength values of unoxidized and oxidized *MWR* determined according to ASTM D 5731-08.
- Table 5.4 Values of  $D$  for unoxidized specimens after testing.
- Table 5.5 Values of  $D$  for oxidized specimens after testing.
- Table 5.6 Acid-base accounting results.
- Table 6.1 Critical state parameters during isotropic compression determined for each range of initial  $D_R$ .
- Table 6.2 Critical state parameters determined from the CSL in  $p'-q$  space and  $\ln(p') - v$  spaces.
- Table 6.3 Critical state friction angle and Bolton’s (1986)  $\phi_p$ -correlation fitting parameters  $Q$  and  $R$ .
- Table 6.4 Comparison of values of  $\phi_p$  predicted using Eq. 6.1 with values of  $\phi_p$  measured in individual tests for the unoxidized *MWR*.
- Table 6.5 Comparison of values of  $\phi_p$  predicted using Eq. 6.1 with values of  $\phi_p$  measured in individual tests for the oxidized *MWR*.
- Table 6.6 Values of  $\Gamma_{se}$  and  $dS$  determined for each unoxidized *LSTX* specimen.

Table 6.7 Values of  $\Gamma_{se}$  and  $dS$  determined for each oxidized *LSTX* specimen.

Table A.1 Example Calculation of  $\Gamma_{se}$

Table D.1 Pressure transducer calibration results

Table D.2 Calibration Information for the Deviatoric Load Transducer

Table D.3 Calibration Information for the Axial Displacement Transducer

Table D.4 Dimensions of membrane strips used to evaluate the elastic modulus of the membranes

Table D.5 Data used to determine the modulus of elasticity for the small membrane

Table D.6 Data used to determine the modulus of elasticity for the large membrane

## LIST OF FIGURES

- Figure 2.1 Effect of specimen diameter and maximum particle size on the drained triaxial compression response of quarried argillite materials used in the Oroville Dam tested with parallel grain size distributions at similar levels of initial  $D_R$  (modified after Marachi et al. 1972).
- Figure 2.2 Effect of maximum particle size on the peak friction angle of three different geomaterials with parallel gradations at similar initial  $D_R$  (modified after Marachi et al. 1972).
- Figure 2.3 Typical linear relationship between peak friction angle and the logarithm of normal stress across the failure plane for various uncemented geomaterials (modified after Leps 1970).
- Figure 2.4 Parallel particle-size distributions (curves a., c., d., and e.) and scalped particle-size distributions (curves b.,f., and g.) tested in DEM simulations with identical particle size, shape and initial  $D_R$  (modified after Sitharam and Nimbkar 2000).
- Figure 2.5 Friction angles for *DEM* modeled parallel and scalped particle-size distributions with identical particle size, shape and initial  $D_R$  (modified after Sitharam and Nimbkar 2000).
- Figure 2.6 Parallel particle size distributions tested by Varadarajan et al. (2003).
- Figure 2.7 Disturbed state friction angles vs.  $d_{max}$  for two well graded gravel (GW) materials tested at  $D_R = 87\%$  and  $p' = 300\text{-}1400$  kPa (modified after Varadarajan et al. 2003).
- Figure 2.8 Effects of maximum particle size and mean effective stress during isotropic compression on unit membrane penetration for five materials with different maximum particle sizes scalped from the Grand-Maison Dam filter material (modified after Dendani et al. 1988).
- Figure 2.9 Effect of nominal particle size  $d_{20}$  on the stress-normalized unit membrane penetration (modified after Nicholson et al. 1993).
- Figure 2.10 Influence of  $p'$  (confining pressure), particle size and particle shape on particle breakage for monotonic *CID* testing at  $D_R = 87\%$ . (Purulia = angular, blasted rockfill, Ranjit Sagar = rounded alluvial rockfill) (Modeled after Varadarajan et al. 2003).
- Figure 2.11 Effect of mean effective stress (after isotropic compression) on the peak friction angle and particle breakage of Fulung sand (Ueng and Chen 2000) and Latite basalt (Indraratna and Salim 2002).
- Figure 2.12  $(\phi_p - \phi_c)$  vs.  $p'$  normalized by grain tensile strength ( $\sigma_o$ ) for geomaterials with particle tensile strengths ranging from 3.5 – 54 MPa (replotted after Lee 1992).

Figure 3.1 Schematic representation of the critical state line and various peak failure envelopes for a hypothetical geomaterial (with  $Q = 10$ ,  $R = 1$  and  $\phi_c = 30^\circ$ ) for various combinations of relative density and mean effective stress.

Figure 4.1 Overhead view of open pit from which the (a) oxidized and (b) unoxidized *MWR* materials were removed.

Figure 4.2 Open pit on the day of removal showing the two shovels working in opposite sides of the pit.

Figure 4.3 Particle size distributions for the Unoxidized and oxidized field samples and the corresponding parallel particle size distributions containing particle sizes appropriate for the *LSTX* apparatus used in the study.

Figure 4.4 Photos of the (a) unoxidized and (b) oxidized *MWR* parallel gradation materials tested in this study.

Figure 4.5 *LSTX* apparatus used in the study.

Figure 5.1 Isotropic compression data for unoxidized specimens. Values of  $p'$  and  $D_R$  represent the final specimen state at the end of compression, before shearing.

Figure 5.2 Isotropic compression data for oxidized specimens. Values of  $p'$  and  $D_R$  represent the final specimen state at the end of compression, before shearing.

Figure 5.3 Axial strain  $\epsilon_a$  vs. volumetric strain  $\epsilon_p$  at the final isotropic level of  $p'$  for unoxidized and oxidized specimens with a line of best fit which was used to estimate the Poisson's ratio for each material. An isotropic line is also included to give an indication of the level of anisotropic response during an isotropic state of stress.

Figure 5.4 Deviatoric stress versus axial stain for unoxidized specimens. Values of  $p'$  and  $D_R$  represent the final specimen state at the end of compression, before shearing.

Figure 5.5 Volumetric strain versus axial stain for unoxidized specimens. Values of  $p'$  and  $D_R$  represent the final specimen state at the end of compression, before shearing.

Figure 5.6 Deviatoric stress versus axial stain for oxidized specimens. Values of  $p'$  and  $D_R$  represent the final specimen state at the end of compression, before shearing.

Figure 5.7 Volumetric strain versus axial stain for oxidized specimens. Values of  $p'$  and  $D_R$  represent the final specimen state at the end of compression, before shearing.

Figure 5.8 Unoxidized specimens in  $\ln(p') - v$  space during axisymmetric compression.

Figure 5.9 Oxidized specimens in  $\ln(p') - v$  space during axisymmetric compression.

Figure 5.10 Effective stress paths for unoxidized specimens. Values of  $p'$  and  $D_R$  represent the final specimen state at the end of compression, before shearing. The two data points for each test correspond to peak and critical state stress states.

Figure 5.11 Effective stress paths for oxidized specimens. Values of  $p'$  and  $D_R$  represent the final specimen state at the end of compression, before shearing. The two data points for each test correspond to peak and critical state stress states.

Figure 5.12 Particle size distributions of unoxidized and oxidized *MWR* specimens before and after testing.

Figure 6.1 Unloading-reloading lines for each range of initial  $D_R$ .

Figure 6.2 Deviatoric stress  $q$  versus axial strain  $\varepsilon_a$  for unoxidized and oxidized specimen compressed to an identical initial state in terms of  $D_R$  and  $p'$  (data points correspond to measured values of peak and critical state  $q$ ).

Figure 6.3 Volumetric strain  $\varepsilon_p$  versus axial strain  $\varepsilon_a$  for unoxidized and oxidized specimen compressed to an identical initial state in terms of  $D_R$  and  $p'$  (data points correspond to ranges of maximum dilatancy rate).

Figure 6.4 CSL in  $\ln(p') - v$  space for unoxidized and oxidized specimens used to determine the critical state parameters  $\Gamma_{cs}$  and  $\lambda_{cs}$ .

Figure 6.5 CSL in  $p' - q$  space for unoxidized and oxidized specimens with a linear best-fit value of  $M$  and the corresponding value of  $\phi_c$ .

Figure 6.6 Evolution of the  $D$  after triaxial shearing at various levels of  $p'$  including 2<sup>nd</sup> order polynomial lines of best fit.

Figure 6.7 Dilatancy response of unoxidized and oxidized *MWR*.

Figure 6.8  $(\phi_p - \phi_c)$  vs.  $p'/I_{s(50)}$

Figure 6.9  $(\phi_p - \phi_c)/D_R$  vs.  $p'/I_{s(50)}$

Figure 6.10 Changes in particle size distributions of unoxidized and oxidized due to the combined effect of isotropic compression and axisymmetric compression. These two specimens were isotropically compressed to identical levels of  $D_R = 81\%$  and  $p' = 200$  kPa before drained axisymmetric compression.

Figure A.1 Energy dissipation within the soil element according to Eq. A.2.

Figure B.1 Particle size distributions of unoxidized *MWR* isotropically compressed to a “loose” state ( $34\% < D_R < 47\%$ ) before drained axisymmetric compression.

Figure B.2 Particle size distributions of unoxidized *MWR* isotropically compressed to a “medium” state ( $57\% < D_R < 64\%$ ) before drained axisymmetric compression.

Figure B.3 Particle size distributions of unoxidized *MWR* isotropically compressed to a “dense” state ( $75\% < D_R < 84\%$ ) before drained axisymmetric compression.

Figure B.4 Particle size distributions of oxidized *MWR* isotropically compressed to a “loose” state ( $68\% < D_R < 89\%$ ) before drained axisymmetric compression.

Figure B.5 Particle size distributions of oxidized *MWR* isotropically compressed to to a “medium” state ( $73\% < D_R < 93\%$ ) before drained axisymmetric compression.

Figure B.6 Particle size distributions of oxidized *MWR* isotropically compressed to to a “dense” state ( $93\% < D_R < 103\%$ ) before drained axisymmetric compression.

Figure C.1 Fractal dimension ( $D$ ) of unoxidized specimens isotropically compressed to a “loose” state ( $34\% < D_R < 47\%$ ) before drained axisymmetric compression.

Figure C.2 Fractal dimension ( $D$ ) of unoxidized specimens isotropically compressed to a “medium” state ( $57\% < D_R < 64\%$ ) before drained axisymmetric compression.

Figure C.3 Fractal dimension ( $D$ ) of unoxidized specimens isotropically compressed to a “dense” state ( $74\% < D_R < 84\%$ ) before drained axisymmetric compression.

Figure C.4 Fractal dimension ( $D$ ) of oxidized specimens isotropically compressed to a “loose” state ( $68\% < D_R < 89\%$ ) before drained axisymmetric compression.

Figure C.5 Fractal dimension ( $D$ ) of oxidized specimens isotropically compressed to to a “medium” state ( $73\% < D_R < 93\%$ ) before drained axisymmetric compression.

Figure C.6 Fractal dimension ( $D$ ) of oxidized specimens isotropically compressed to to a “dense” state ( $93\% < D_R < 103\%$ ) before drained axisymmetric compression.

Figure D.1 Calibration plot for cell pressure transducer.

Figure D.2 Calibration plot for pore water pressure transducer.

Figure D.3 Calibration plot for the deviatoric load transducer.

Figure D.4 Calibration plot for the axial displacement transducer.

## LIST OF SYMBOLS

$A$  – proportionality constant

$A_c$  – corrected cross sectional specimen area ( $\text{m}^2$ )

$A_{ce}$  – cross sectional area of the specimen at the end of the test ( $\text{m}^2$ )

$A_f$  – cross sectional area at failure ( $\text{m}^2$ )

$A_o$  – cross sectional area at the end of isotropic compression ( $\text{m}^2$ )

$B_g$  – breakage factor (%)

$\beta_s$  – particle shape factor

$\beta_v$  – particle volume factor

$C_u$  – coefficient of uniformity

$C_c$  – coefficient of curvature

$d$  – particle size (mm)

$d_{max}$  – maximum particle size (mm)

$d_{50}$  – mean particle size (mm)

$dS$  – change in surface area ( $\text{m}^2$ )

$dx$  – finite displacement in the direction of shearing

$dy$  – finite displacement perpendicular to the plane of shearing, in the direction of normal loading

$D$  – fractal dimension

$D_f$  – final fractal dimension (after testing)

$D_R$  – relative density (%)

$\delta_e$  – axial strain due to movement along the shear plane (%)

$\delta\varepsilon_q$  – deviatoric strain increment

$\delta\varepsilon_p$  – octahedral mean strain increment

$e$  – void ratio

$e_{min}$  – minimum void ratio

$e_{max}$  – maximum void ratio

$E$  – elastic modulus of the membrane (kPa)

$\varepsilon_1$  – major principal strain (%)

$\varepsilon_3$  – minor principal strain (%)

$\varepsilon_a$  – axial strain (%)

$\varepsilon_{ai}$  – axial strain between peak  $q$  and the end of the test (%)

$\varepsilon_{ae}$  – axial strain at the end of the test (%)

$\varepsilon_{af}$  – axial strain at failure (%)

$\varepsilon_p$  – volumetric strain (%)

$\varepsilon_r$  – radial strain (%)

$f$  – unit friction between the membrane and dummy (kPa)

$G_s$  – specific gravity of solids

$\Gamma_{se}$  – surface energy (J/m<sup>2</sup>)

$\Gamma_{cs}$  – intercept of the critical state line at  $p' = 1$  kPa

$\phi$  – mobilized friction angle (deg.)

$\phi_c$  – critical state friction angle (deg.)

$\phi_c^*$  – apparent critical state friction angle (deg.)

$\phi_{tb}$  – friction angle excluding dilatancy and including particle breakage (deg.)

$\phi_{\dagger}$  – friction angle excluding dilatancy and particle breakage (deg.)

$\phi_p$  – peak friction angle (deg.)

$I_{a(50)}$  – point load anisotropy index

$I_D$  – relative density

$I_R$  – relative dilatancy index

$I_{s(50)}$  – size corrected point load strength index (MPa)  
 $\kappa$  – slope of a *URL*  
 $\lambda_{cs}$  – slope of the *CSL*  
 $M$  – slope of the critical state line in  $p' - q$  space (uppercase mu)  
 $M$  – dilatancy number  
 $\mu$  – coefficient of frictional resistance  
 $N$  – flow number  
 $N_f$  – normal force (kN)  
 $N_c$  – flow number at critical state  
 $N(L > d)$  – number of particles of diameter  $L$  greater than  $d$   
 $n$  – porosity  
 $\nu$  – specific volume  
 $\nu_\kappa$  – specific volume along a *URL*  
 $\nu_{cs}$  – specific volume along the *CSL*  
 $p'$  – mean effective stress, mean effective stress invariant (kPa)  
 $p_A$  – reference stress (kPa)  
 $p'_{cs}$  – mean effective stress at the critical state (kPa)  
 $p_p'$  – peak mean effective stress (kPa)  
 $P$  – concentrically applied load (kN)  
 $q$  – deviatoric stress (kPa)  
 $q_{cs}$  – deviatoric stress at critical state (kPa)  
 $Q$  – Bolton (1986) fitting parameter  
 $R$  – Bolton (1986) fitting parameter  
 $R_s$  – principal strain ratio  
 $S$  – surface area (m<sup>2</sup>)

$S_{\sigma_3}$  – stress normalized unit membrane penetration (mm/  $\Delta \log(\sigma'_r)$ )

$\sigma$  – normal stress (kPa)

$\sigma'$  – normal effective stress (kPa)

$\sigma_1'$  – major principal effective stress (kPa)

$\sigma_3'$  – minor effective stress (kPa)

$\sigma_a'$  – effective axial stress (kPa)

$\sigma_c'$  – effective confining stress (kPa)

$\sigma_r'$  – effective radial stress (kPa)

$t$  – time (hr)

$T_f$  – shearing force (kN)

$\tau$  – shear stress (kPa)

$V$  – volume ( $m^3$ )

$V_s$  – volume of solids ( $m^3$ )

$\psi$  – dilatancy angle (deg.)

## LIST OF ACRONYMS

*ABA* – acid-base accounting

*AMD* – acid mine drainage

*AP* – acid producing potential

*CID* – isotropically compressed, drained axisymmetric compression test

*CIU* – isotropically compressed, undrained axisymmetric compression test

*COV* – coefficient of variation

*CSL* – critical state line

*DEM* – discrete element modeling

*EPA* – United States Environmental Protection Agency

*LSTX* – large-scale triaxial

*MWR* – mine waste rock

*MSL* – mean sea level

*NCL* – normal compression line

*NNP* – net neutralizing potential

*NP* – neutralizing potential

*NPR* – neutralizing potential ratio

*URL* – unloading-reloading line

## CHAPTER 1: INTRODUCTION

### 1.1 Problem Statement

Mine waste rock (*MWR*) is produced during open pit mining when overburden material is removed. *MWR* is commonly stockpiled in waste rock piles or used to construct embankment dams for tailings ponds. These embankment dams typically retain volatile tailings solutions. Thus, assurance of long-term stability of these structures is essential. *MWR* typically contains maximum particle sizes ( $d_{max}$ ) larger than the  $d_{max}$  used in conventional geotechnical testing equipment such as triaxial compression, direct shear and simple shear apparatuses making evaluation of the mechanical behavior of mine waste rock challenging. Assuring long-term stability of structures built with *MWR* requires a fundamental understanding of the actual mechanical behavior of *MWR*.

*MWR* is subjected to unloading and an altered environment upon removal which may lead to time dependent changes in its mechanical behavior (Robertson and Wiles 1990). *In situ* weathering, occurring before blasting and excavation, may also influence the mechanical behavior of *MWR* as well as potential future time-dependent behavioral changes. Previous investigations have described durability and weathering of *MWR* in a qualitative manner: Slake Durability (Franklin and Chandra 1972), Point Load Strength (Broch and Franklin 1972), Abrasion pH (Grant 1969). Rigorous investigations describing changes in mechanical behavior are limited (Franke 2009). This is likely due to the fact that capturing time-dependent changes in the mechanical behavior of *MWR* is extremely difficult. Accelerated laboratory weathering techniques poorly represent field

conditions, while more accurate techniques take years to show significant changes. The natural environment typically provides multiple, concurrent weathering or degradation processes. Thus, a fundamental characterization of the mechanical response and possible degradation of *MWR* might be the first step in understanding the fundamental relationship between weathering and mechanical strength degradation of *MWR*. In addition to a fundamental mechanical characterization study, an evaluation of the natural degree of oxidation was used in this study to assess the differences in the intrinsic mechanical characteristics of two *MWR* materials derived from more and less oxidized zones of the same geologic formation (Ordovician Vinini).

In addition to the inherently challenging aspects associated with the characterization of materials with large particle sizes, another aspect that would need to be taken into account in such study is particle breakage. Particle breakage consumes irrecoverable energy during loading and has been shown to influence the mechanical behavior of geomaterials both theoretically (Bolton et al. 2008, McDowell and Harireche 2002, Lee 1992) and experimentally (Lee 1992, Marsal 1973, Vesic and Clough 1968, Lee and Farmoohand 1967). This influence may be more significant in geomaterials with large, angular, or weak particles (Varadarajan et al. 2003, Marsal 1973, Lee and Farmoohand 1967). Accounting for the effects of particle breakage is an essential step in describing the relationship between weathering and mechanical degradation of *MWR*. Due to the large, angular, and potentially weak particles found in *MWR*, a rigorous description of the mechanical behavior *MWR* requires an experimental framework that takes into account the effects of energy consumption due to particle breakage, *in situ* weathering and

sample-scaling during laboratory testing. These factors are in addition to the typical intrinsic parameters (i.e.  $\phi_c$ ,  $Q$ , and  $R$ ) required for accurate description of the triaxial response of uncemented, saturated geomaterials (i.e. sands, silts, and clays). This study was designed and carried out to increase our understanding of the interactions between all factors described above which affect the mechanical response of *MWR*.

## 1.2 Research Objectives

The overall intent of this research is to systematically evaluate the effect of the main factors that influence the mechanical response of *MWR*. In a more fundamental way, these main factors may be classified as either: (1) state variables or (2) intrinsic variables. Different combinations of state variables were systematically evaluated in order to describe their influence on the overall mechanical response and determine the intrinsic parameters of *MWR*. Specifically, differences in the intrinsic parameters of unoxidized and oxidized *MWR* were used to elucidate effects of *in situ* weathering on their shear strength and triaxial response.

The effects of state variables such as mean effective stress ( $p'$ ) and relative density ( $D_R$ ) were varied to assess the effect of each variable on the mechanical response of the materials tested. The effects of changes in state variables were observed over a wide range of mean effective stresses, strains, and densities.

Specific objectives of the study were to:

1. Determine the reduction of shear strength between unoxidized and oxidized *MWR* and determine the causes for this reduction;
2. develop an appropriate method for reconstitution of uniform *MWR* specimens;
3. conduct an experimental program to determine the intrinsic parameters of *MWR*;
4. characterize the drained response of each material in monotonic axisymmetric compression;
5. quantify the effect of particle breakage on the mechanical response and intrinsic parameters of *MWR*; and
6. incorporate the experimental data into a rigorous theoretical framework.

### 1.3 Research Scope

This study focuses on the triaxial compression response of unoxidized and oxidized *MWR*. The two *MWR* types referred to as ‘unoxidized’ and ‘oxidized’ were removed from an open pit mine simultaneously from similar elevations. However, the pre-sampling, natural hydrogeologic conditions led to one of the samples being more oxidized than the other. Bulk field samples were collected and tested in a large-scale triaxial device (*LSTX*) device in order to characterize the mechanical response of each material. These bulk field samples contained particles that were too large even for the *LSTX* apparatus used, so particle size distributions parallel to their respective field gradation were used to maintain maximum particle sizes appropriate for the apparatus (Varadarajan 2003, Sitharam and Nimbkar 2000). Unoxidized and oxidized specimens were tested in drained monotonic under axisymmetric compression, where  $p'$  at the start

of shearing was equal to 100, 200 or 400 kPa. Particle-size distributions were determined after testing for all specimens tested to quantify particle breakage during testing. More specific description of maximum particle-size restrictions and scaling methods for triaxial specimens is discussed in Chapter 4.

#### 1.4 Manuscript Organization

This thesis contains six additional chapters, as well as four appendices, which cover numerous aspects of the mechanical response of two *MWR* types. In Chapter 2, a comprehensive literature review of previous investigations into the mechanical response of geomaterials containing large particle sizes, such as *MWR*, rockfill and other coarse aggregates is presented. Chapter 3 presents the theoretical framework used in this study. Chapter 4 describes the experimental program used to characterize, prepare, and test specimens. Also contained in Chapter 4, is a description of the geologic unit from which the *MWR* samples were taken. Results from this experimental program are presented in Chapter 5 and these results are analyzed in Chapter 6. The seventh and final chapter provides a summary of the main conclusions and recommendations that were revealed during the research program. Appendix A presents a step-by-step example calculation of the surface energy ( $\Gamma_{se}$ ) of the *MWR* materials. Appendix B presents the particle size distributions before and after testing, which were used to quantify the change in surface area ( $dS$ ) of a specimen due to testing. Appendix C presents the plots used to calculate the fractal dimension ( $D$ ) of the *MWR* materials. Appendix D presents calibration information for the transducers used in the testing program.

## CHAPTER 2: MECHANICAL BEHAVIOR OF MINE WASTE ROCK (*MWR*)

### 2.1 Background

Proper characterization of the mechanical response of geomaterials with large particle sizes such as mine waste rock (*MWR*), rockfill and coarse aggregates is challenging. The triaxial apparatus is one of the most widely used devices to evaluate the shear strength and stiffness of geomaterials. However, geomaterials used in a wide range of geotechnical and mining applications have particle sizes much larger than the  $d_{\max}$  tested in a conventional triaxial apparatus with specimen diameter ( $d_{sp}$ ) ranging from 50-70 mm. These limitations led to the development of large-scale triaxial (*LSTX*) devices with  $d_{sp}$  values ranging from 100-1000 mm to assess the mechanical behavior of geomaterials with very large particle sizes. Due to the limited amount of systematic research specifically regarding *MWR*, this chapter provides a summary of the literature pertaining to *LSTX* investigations for all types of geomaterials with large particle sizes.

### 2.2 Large-scale Triaxial Testing

In triaxial testing, the sample-size ratio can be defined as the ratio  $d_{sp}/d_{\max}$  of specimen diameter to maximum particle size (Vallerga et al. 1957, Marachi 1969, Indraratna 1993). The use of sample-size ratios smaller than five has been shown to introduce testing errors due to particle size effects (Marsal 1969, Leslie 1969, Nitchiporovitch et al. 1969), especially when “more than 30% of the sample mass is retained on the largest sieve size” (Marachi 1969). Use of a minimum sample-size ratio of six is recommended by ASTM D4767 for consolidated isotropically undrained triaxial (*CIU*) testing. This sample-size ratio leads to a maximum particle size of 12 mm for a 70-mm-diameter specimen. A

maximum particle size of 12 mm may represent a small portion of geomaterials with large particle sizes such as *MWR*, rockfill, and coarse aggregates. Quine (1993) evaluated the mechanical behavior of sixteen *MWR* materials from six mines in north-central Nevada, all of which classified as well graded gravel (GW) according to the Unified Soil Classification System (USCS) (ASTM D 2487). The maximum particle size for a conventional triaxial apparatus (12-mm) typically corresponded to the finest 20% - 30% of the *MWR* materials by mass. These shortcomings lead to uncertainties associated with the assignment of shear strength and stiffness parameters for such materials during modeling and design.

Limitations of the conventional triaxial apparatus with regard to maximum particle size were first addressed by Holtz and Gibbs (1956) who tested various mixtures of sand and gravel-size particles in an *LSTX* apparatus over a wide range of relative density ( $D_R$ ) and mean effective stress [ $p' = (\sigma'_1 + 2\sigma'_3)/3$ ] where  $\sigma'_1$  and  $\sigma'_3$  are the effective major and minor principal stresses, respectively. Results of 183 tests indicated that peak friction angles increased with increasing particle size and angularity as well as with increasing gravel content up to around 50-60% for similar initial  $D_R$  and range of  $p'$ . Above this threshold gravel content, the peak shear strength of the specimens decreased with increasing gravel content.

Marachi et al. (1972) investigated particle-size effects on shear strength by testing parallel gradations of three rockfill materials. Parallel gradations maintain a constant ratio between particle sizes at a given percent passing in a conventional particle size distribution. This ratio may be defined by the ratio of maximum field particle size to

maximum particle size that can be tested in a given triaxial apparatus. Tests were completed on materials of similar mineralogical composition and geologic history with specimen diameters equal to 70, 305 and 914 mm using a constant sample-size ratio of six. As both specimen diameter and maximum particle size decreased, the measured peak friction angles increased and volumetric strains became more dilative (or less contractive) in triaxial compression (Fig. 2.1). All tests shown in Figure 2.1 were isotropically consolidated to the  $p'$  equal to 210 kPa and similar levels of  $D_R$ . The corresponding volumetric strain [ $\varepsilon_p = \varepsilon_1 + 2\varepsilon_3$ ] in triaxial (or, perhaps more rigorously, axisymmetric) compression shown in Figure 2.1 can then be consistently defined and associated with changes of the octahedral mean stress invariant  $p'$ , where  $\varepsilon_1$  and  $\varepsilon_3$  are the major and minor principal strains, respectively. Marachi et al. (1972) also noted relatively minor effects of specimen size on volumetric strains during isotropic compression for similar initial relative densities. Use of conventional triaxial testing equipment with a specimen diameter of 70 mm led to an overestimation of the peak friction angle ( $\phi_p$ ) of about 3-4° (6-8%), as it may be deduced from the data shown in Figure 2.1.

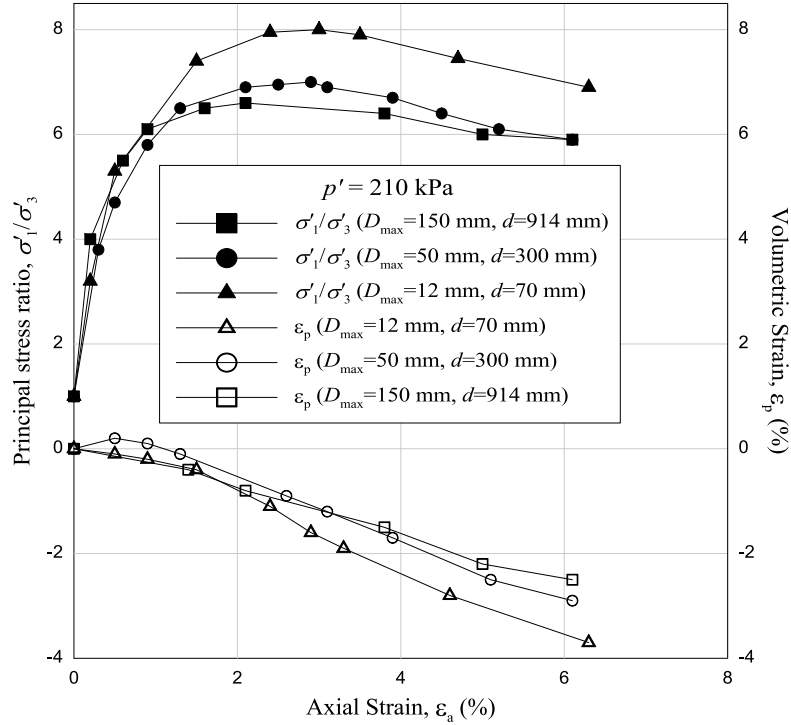


Figure 2.1 Effect of specimen diameter and maximum particle size on the drained triaxial compression response of quarried argillite materials used in the Oroville Dam tested with parallel grain size distributions at similar levels of initial  $D_R$  (modified after Marachi et al. 1972).

Differences in the  $\phi_p$  of geomaterials with large particle sizes, relative to the corresponding  $\phi_p$  of similar geomaterials with smaller particle sizes, may be pronounced (Fig. 2.2). These differences make the *LSTX* apparatus an important and necessary tool to characterize the shear strength and stiffness parameters of geomaterials with large particle sizes such as those used to construct dams and other geotechnical structures.

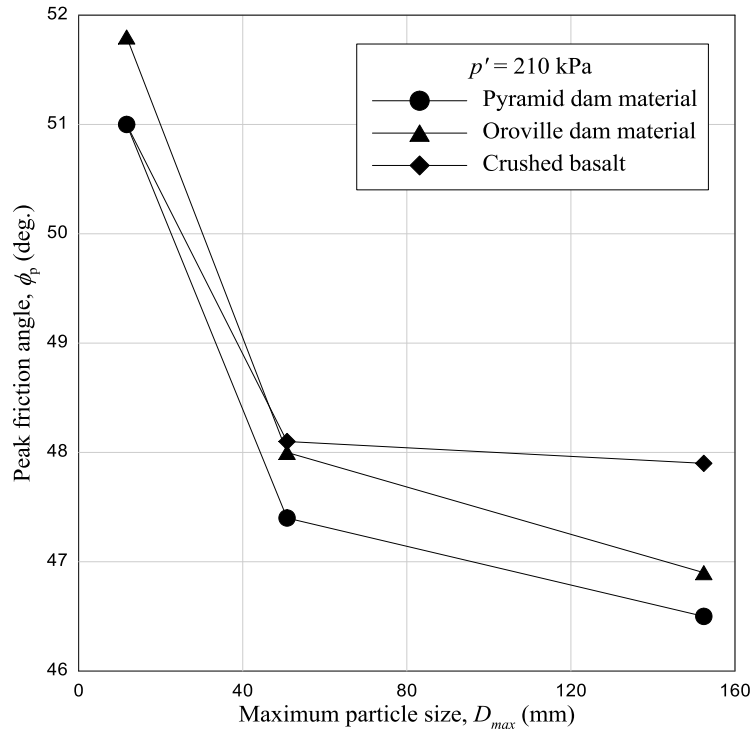


Figure 2.2 Effect of maximum particle size on the peak friction angle of three different geomaterials with parallel gradations at similar initial  $D_R$  (modified after Marachi et al. 1972).

In many cases, characterization of the true field-scale shear strength parameters may not be possible, due to the limited specimen diameters and maximum particle sizes that can be practically used during testing, even when using the largest triaxial apparatus available. In order to assess this limitation, the three different geomaterials with parallel grain-size distributions tested by Marachi et al. (1972) may be used to estimate the potential variation in  $\phi_p$  values resulting from testing samples with maximum particle sizes of at least 12 mm taken from original field-scale samples with maximum particle sizes equal to 150 mm (Fig. 2.2). As shown in Figure 2.2, the difference in  $\phi_p$  values measured using conventional 70-mm-diameter specimens with 12-mm maximum particle sizes or 914-mm-diameter specimens with 150-mm maximum particle sizes may be as large as  $5^\circ$  ( $\sim 11\%$ ). If 150-mm-diameter specimens with 25-mm maximum particle sizes

were prepared using the same parallel gradation criterion and tested at the same  $p' = 210$  kPa and sample-size ratio of six used by Marachi et al. (1972), this error would be reduced by half to about  $2-3^\circ$  ( $\sim 5\%$ ).

### 2.2.1 Dilatancy and Critical State

Reynolds (1885) coined the term dilatancy after observing the effect of density on the volumetric response of sands during shearing. For  $p'$  levels associated with most typical geotechnical applications, loose sands contract during shearing until critical state is reached at constant shear stress and constant volume (Schofield and Wroth 1968). On the other hand, dense sands dilate and mobilize peak shear stress before critical state is reached at large strains. Dilation, which is primarily affected by the soil state (density and effective stress), is the main factor responsible for the curvature of the failure envelope of uncemented geomaterials with strong grains used in most geotechnical applications.

Leps (1970) reviewed the literature regarding the shear strength of rockfill and compiled a large amount of *LSTX* results to show the linear dependence of  $\phi_p$  on the logarithm of the “normal stress across the failure plane” for sands and rockfill materials (Fig. 2.3). From a more rigorous, conceptual standpoint,  $\phi_p$  determined from triaxial tests may be related to the peak mean effective stress  $p'_p$  (Bolton 1986). For Ottawa sand, for example, additional lower and upper bounds with different slopes could be identified and superimposed to the data shown in Figure 2.3 for  $D_R$  levels equal to 0 and 100%, respectively, as  $\phi_p$  depends not only on  $p'_p$  but also on density. Likewise, additional upper

and lower bounds can be defined for density states varying between the loosest and densest states possible to be achieved for any material, such as those shown in Figure 2.3.

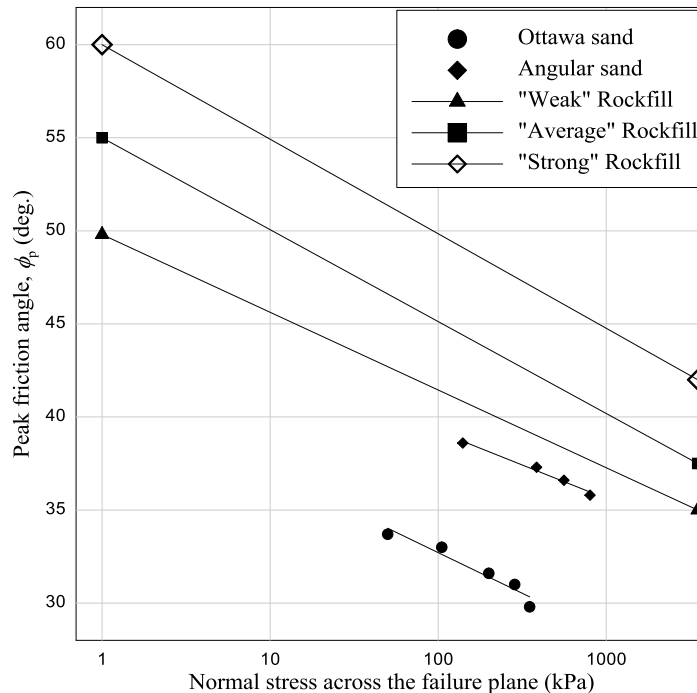


Figure 2.3 Typical linear relationship between peak friction angle and the logarithm of normal stress across the failure plane for various uncemented geomaterials (modified after Leps 1970).

Unlike dilatancy, the critical state of a geomaterial is considered to be related to its intrinsic characteristics such as particle shape, mineralogy and grain size distribution (Schofield and Wroth 1968). For a more comprehensive and thorough discussion of critical state soil mechanics concepts, the reader may refer to Schofield and Wroth (1968) and Muir-Wood (1990).

### 2.2.2 Modeled Particle Size Distributions

Varadarajan et al. (2003) summarized previously established modeling techniques used to reduce particle size distributions into four basic types: (1) scalping (Zeller and Wulliman 1957), (2) parallel gradations (Lowe 1964), (3) quadratic particle size distributions

(Fumagalli 1969), and (4) replacement (Frost 1973). Scalping is the simplest technique in which particles too large for testing are simply excluded during testing. Parallel gradations maintain a constant ratio between particle sizes at a given percent passing in a conventional particle size distribution. Quadratic particle size distributions may be described by Eq. 2.1. The replacement technique aims to maintain consistent limiting void ratios between laboratory compaction tests and actual field gradations which contain particle sizes too large for the compaction mold. Results from a number of rockfill dam sites illustrate the wide variation in particle sizes and index densities between lab and field data.

$$P(\%) = 100 \cdot \sqrt{\frac{d}{d_{\max}}} \quad (2.1)$$

where  $P(\%)$  is the percent passing a sieve of size  $d$  and  $d_{\max}$  is the maximum testing particle size.

Sitharam and Nimbkar (2000) noted the lack of any clear mechanistic validation for these techniques and instead proposed *DEM* modeling as a systematic approach to understand the factors and mechanisms affecting the constitutive behavior of various assemblages of particles. Results were twofold and may be best described by Figures 2.4 and 2.5. First, samples with parallel gradations and identical particle shape and  $D_R$  have the same fabric, which theoretically makes them behave similarly if not identically under identical boundary conditions. On the other hand, samples at a similar initial state subjected to the same boundary conditions with reduced maximum particle sizes and the same minimum particle size (i.e. prepared by the scalping technique) show an increase in peak friction angle as the maximum particle size is reduced. This difference is attributed to the altered fabric and increased coordination number for the non-parallel particle size distributions.

Coordination number is defined as the number of interparticle contacts for a given particle in a soil matrix (McDowell et al. 1996). Conclusions of the numerical model suggest parallel gradations to be the best particle size reduction technique for achieving consistent mechanical response between field-scale materials and laboratory test specimens as the measured friction angle is more consistent. The slope of the two best fit lines in Fig. 2.5 may be estimated as being equal to 0.07-deg./mm for the parallel gradations and -0.15-deg./mm for the scalped gradations.

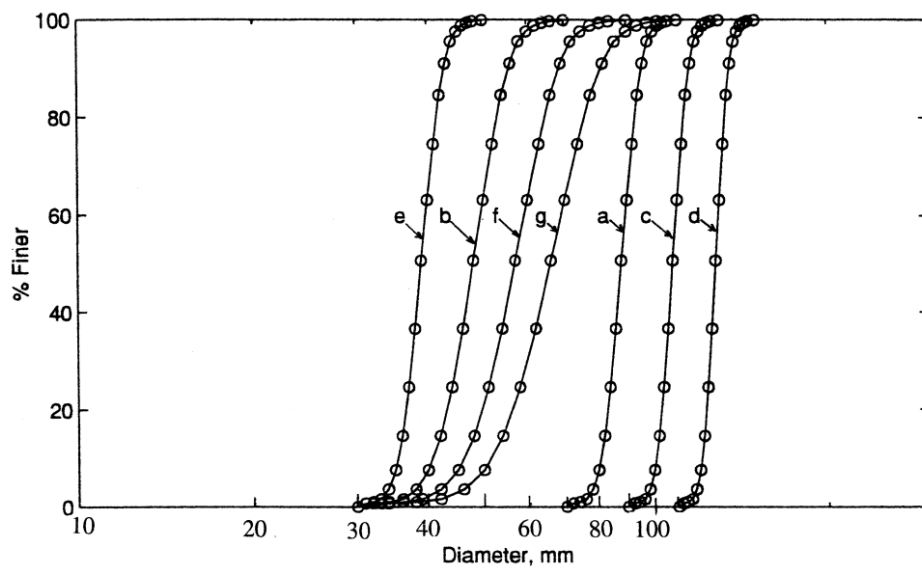


Figure 2.4 Parallel particle-size distributions (curves a., c., d., and e.) and scalped particle-size distributions (curves b.,f., and g.) tested in DEM simulations with identical particle size, shape and initial  $D_R$  (modified after Sitharam and Nimbkar 2000).

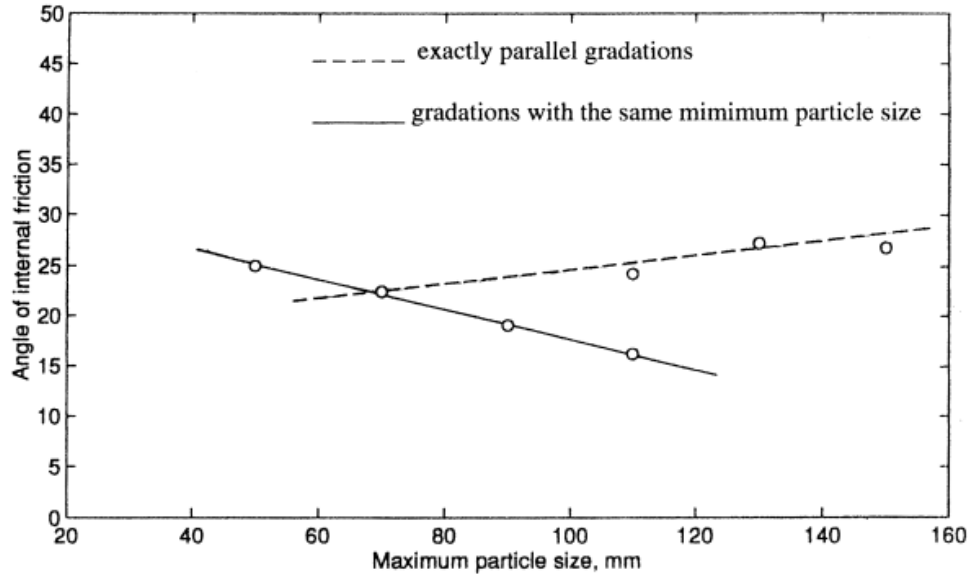


Figure 2.5 Friction angles for *DEM* modeled parallel and scalped particle-size distributions with identical particle size, shape and initial  $D_R$  (modified after Sitharam and Nimbkar 2000).

In an attempt to confirm these numerical simulations, Varadarajan et al. (2003) tested three reduced parallel particle size distributions of two geomaterials in a *LSTX* apparatus with  $d_{max}$  equal to 25, 80, and 120 mm. The Purulia Dam material was a sub-rounded alluvial fill and the Ranjit Sagar Dam materials was an angular, blasted, sedimentary rockfill. As seen in the particle size distributions of the two materials in Figure 2.6, the Purulia Dam material contained some fines, and the modeled gradations were maintained parallel up to the 0.075 mm (#200) sieve. This means the same minimum particle sizes were tested for all triaxial tests for the finest fractions ( $d_0 - d_{14}$ ) which lead to a small amount of “scalping” of the parallel gradations. The Ranjit Sagar Dam materials contained no fines, and therefore perfectly parallel gradations were maintained for all test specimens.

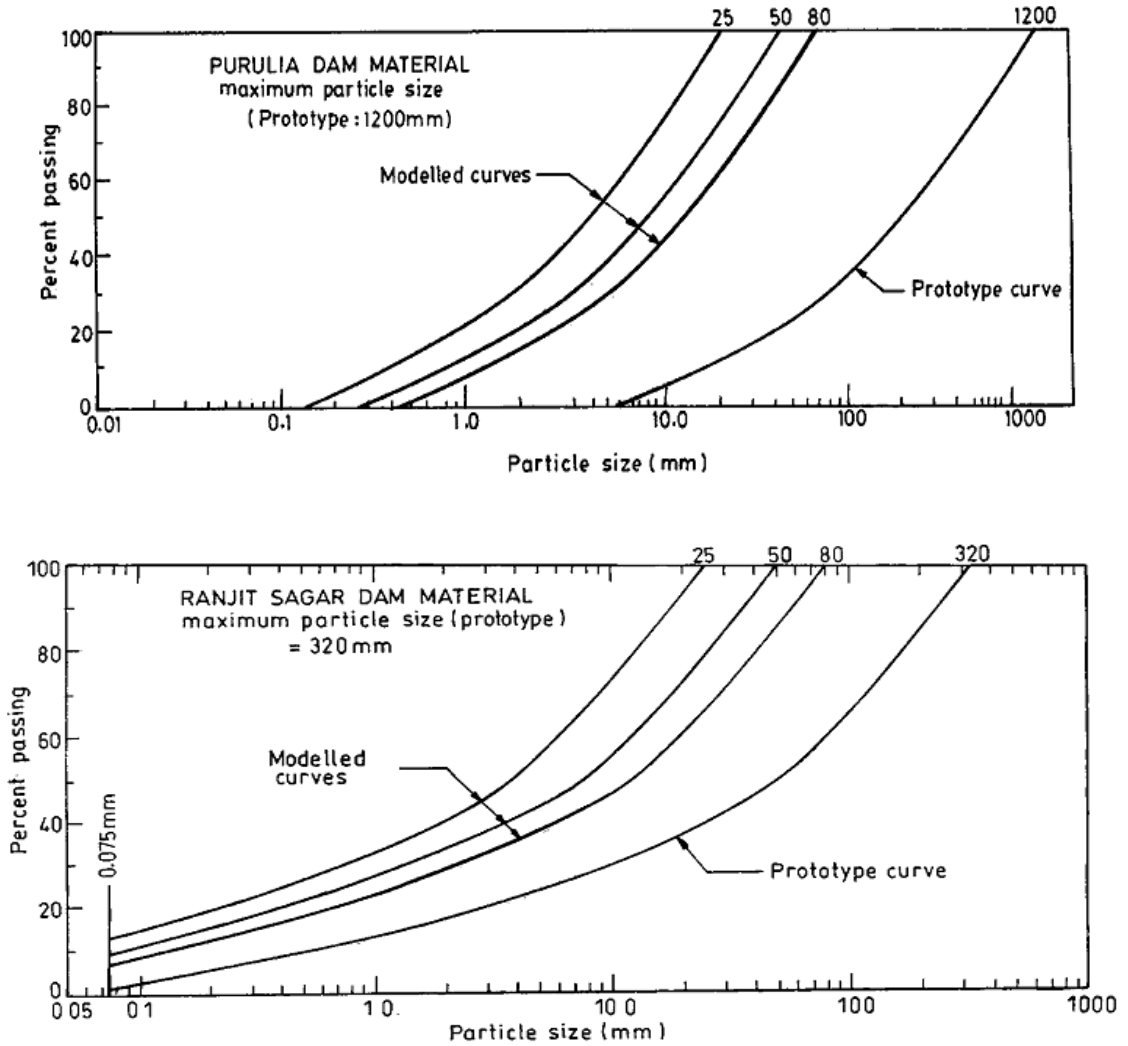


Figure 2.6 Parallel particle size distributions tested by Varadarajan et al. (2003).

Results of the study (Figure 2.7) are somewhat consistent with those from the numerical modeling from Sitharam and Nimbkar (2000) showing slight differences in disturbed state friction angle in tests with perfectly parallel particle-size distributions, and more pronounced differences in disturbed state friction angle in tests with particle size distributions containing the same minimum particle size. This may be demonstrated by comparing the slopes of the best fit lines in Fig. 2.5 ( $-0.15\text{-deg./mm}$  for scalped gradations and  $0.07\text{-deg./mm}$  for parallel gradations) with the slopes of the best fit lines

in Fig. 2.7 which give values of -0.034-deg./mm for the parallel gradations and 0.071-deg./mm for scalped gradations. One less consistent conclusion between the two studies is that although these slopes of best fit lines are less for parallel gradations, the slopes of these best fit lines are opposite directions between the two studies. Friction angles of perfectly parallel particle-size distributions (Purulia Dam Material) decrease with increasing  $d_{max}$ , while particle-size distributions with the same minimum particle size (Ranjit Sagar Material) increase with increasing  $d_{max}$ . In the numerical modeling the opposite was true, as friction angles of perfectly parallel particle-size distributions increase slightly with increasing  $d_{max}$ , while particle-size distributions with the same minimum particle size decrease with increasing  $d_{max}$ . These observations may be caused by wide variations in particle shapes between the Ranjit Sagar (rounded) and Purulia Dam (angular) materials. Furthermore, neither real-world material will have the same particle shapes as the assemblies of identically shaped disc-shaped particles modeled by Sithram and Nimbkar (2000). However, regardless of the direction of the slopes of the best fit lines in Figs. 2.5 and 2.7, parallel particle-size distributions appear to be the best particle size reduction technique for achieving consistent mechanical response between field-scale materials and laboratory test specimens.

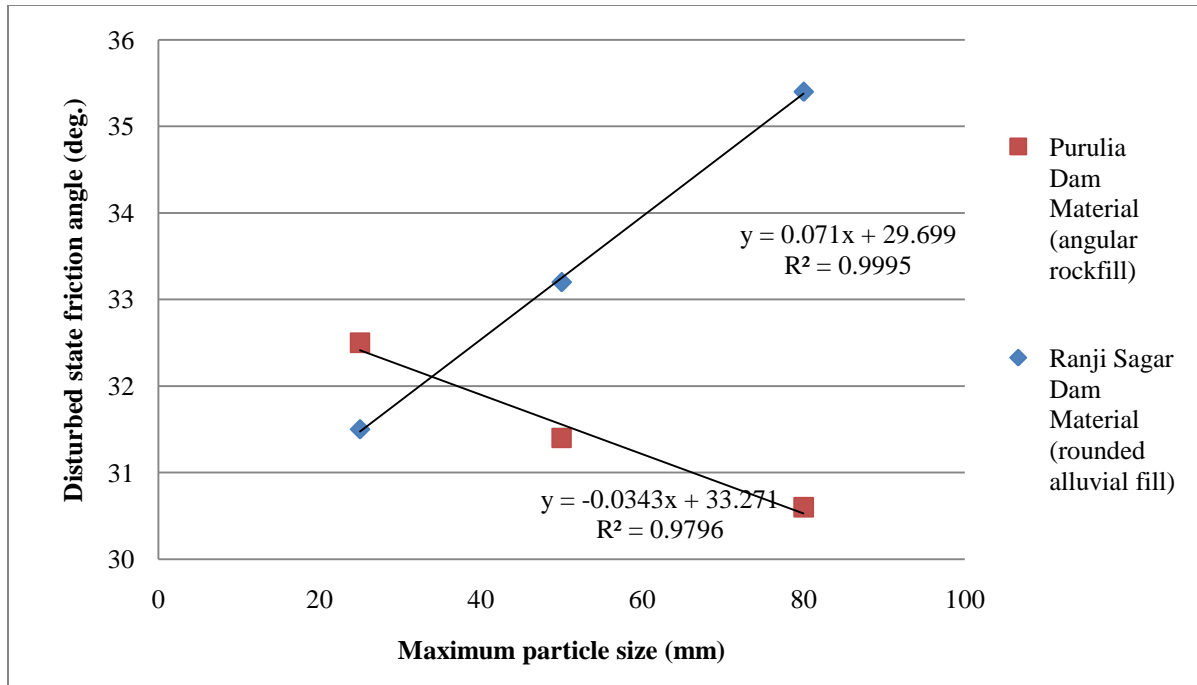


Figure 2.7 Disturbed state friction angles vs.  $d_{max}$  for two well graded gravel (GW) materials tested at  $D_R = 87\%$  and  $p' = 300 - 1400$  kPa (modified after Varadarajan et al. 2003).

### 2.2.3 Membrane Penetration

An aspect that makes LSTX testing more challenging than conventional triaxial testing involves properly accounting for penetration of the rubber membrane into the specimen voids during saturation, consolidation and shearing. Large void spaces between particles commonly exist at the lateral boundary of specimens containing large particle sizes, regardless of their density. Drainage of the pore water originally filling these voids due to the deformation of the membrane into the specimen voids with increasing  $p'$  during consolidation may result in measurement of artificially large  $\varepsilon_p$  values. Results of numerous studies on this topic have identified particle size, specimen size, effective confining stress ( $\sigma'_c$ ), and membrane characteristics as significant factors associated with membrane penetration (Sivathayalan and Vaid 1998, Ansal and Erken 1996, Nicholson et

al. 1992, Choi and Ishibashi 1992, Kramer et al. 1990, Dendani et al. 1988, Baldi and Nova 1982, Molenkamp and Luger 1981, Frydman et al. 1973).

Failure to correct for these artificially high  $\varepsilon_p$  values may lead to additional errors. For example, errors related to the measurement of the actual effective axial stress ( $\sigma'_a$ ) applied to the specimen may arise if uncorrected  $\varepsilon_p$  values are used in the calculations. This is because the specimen cross sectional area during consolidation and drained triaxial compression is conventionally updated based on current levels of radial strain ( $\varepsilon_r$ ), which, in turn, is typically deduced from current values of  $\varepsilon_p$  and axial strain ( $\varepsilon_a$ ) if local axial and radial strain transducers are not used. During drained triaxial compression, the effective radial stress ( $\sigma'_r$ ) remains constant, which keeps the amount of membrane penetration at relatively constant levels at this stage. However, significant errors would remain in undrained triaxial compression (when changes in  $\sigma'_r$  may not be negligible) as pore pressure measurements at this stage would still be affected by membrane penetration (Ansal and Erken 1996, Molenkamp and Luger 1981).

The total pore water volume drained out of the specimen due to membrane penetration normalized by the initial contact area between the membrane and the lateral surface of the specimen is defined as the unit membrane penetration or unit normalized penetration (Choi and Ishibashi 1992, Kramer 1989, Dendani et al. 1988, Baldi and Nova 1984, Frydman et. al 1973). Early experimental methods attempting to quantify this error invoked many assumptions regarding true specimen deformation in the triaxial apparatus. While the magnitude of unit membrane penetration estimated by different early studies

may be pronounced (Choi and Ishibashi 1992), some studies have observed a linear relationship between the logarithm of  $p'$  and unit membrane penetration (Dendani et al. 1988, Frydman et al. 1973).

Dendani et al. (1988) discussed the overwhelming effect of particle size on unit membrane penetration. Results demonstrate the potential errors associated with assumptions of linear relationships between unit membrane penetration and changes in the logarithm of  $p'$  during consolidation which do not take particle size effects into consideration (Figure 2.8).

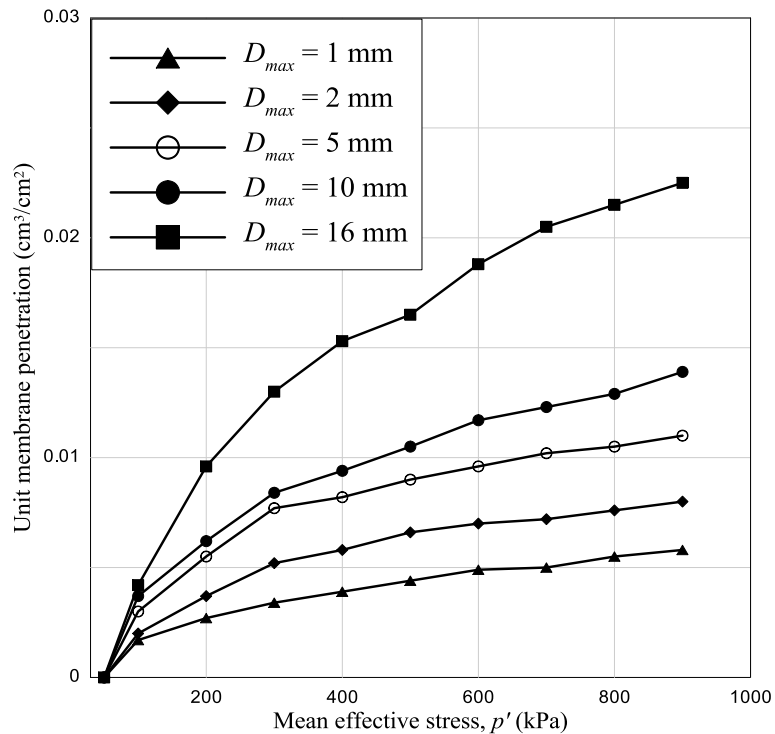


Figure 2.8 Effects of maximum particle size and mean effective stress during isotropic consolidation on unit membrane penetration for five materials with different maximum particle sizes scalped from the Grand-Maison Dam filter material (modified after Dendani et al. 1988).

Other analytical methods have represented the lateral surface of a triaxial specimen as an array of spheres of varying diameters related to the grain size distribution of an actual soil (Sivathayalan and Vaid 1998, Ansal and Erken 1996, Nicholson et al. 1992, Kramer et al. 1990, Molenkamp 1981, Baldi and Nova 1982). These studies showed similar observations of linear semi-logarithmic plots of unit membrane penetration with the logarithm of effective stress for sands and glass beads alike. Various empirical relations have been presented to predict membrane penetration based on experiments which take the most influential factors affecting membrane penetration (particle size, effective confining stress, membrane thickness) into account. However, large differences in the proposed corrections remained, especially for grain sizes larger than 3 mm, until Nicholson et al. (1993) showed the nominal particle size  $d_{20}$  (in mm) is the most accurate parameter to estimate the stress-normalized unit membrane penetration ( $S_{\sigma'3}$ ) after isotropic compression. In this format, the measured volume change due to membrane penetration is normalized by the lateral surface area of the specimen as well as the change in the logarithm of effective radial stress. Results are based on a wide range of experimental data including specimens tested in a 300-mm-diameter *LSTX* apparatus equipped with internal radial transducers, Nicholson et al. (1993) proposed that  $S_{\sigma'3}$  (mm/ $\Delta \log(\sigma'_r)$ ) be estimated according to:

$$S_{\sigma'3} = 0.0019 + 0.0095 d_{20} - 0.0000157 d_{20}^2 \quad (2.2)$$

The specimens tested by Nicholson et al. (1993) were subjected to isotropic compression  $p'$  levels as high as 1200 kPa to encompass the usual testing ranges for which membrane-

compliance effects may be of concern. Conventional scale triaxial and *LSTX* apparatuses were each used in the study with latex membranes with thicknesses equal to 0.35 mm and 3 mm, respectively. Initial relative density was in the range of 50-60% for all specimens. Data used to develop Eq. 2.1 is shown in Figure 2.9.

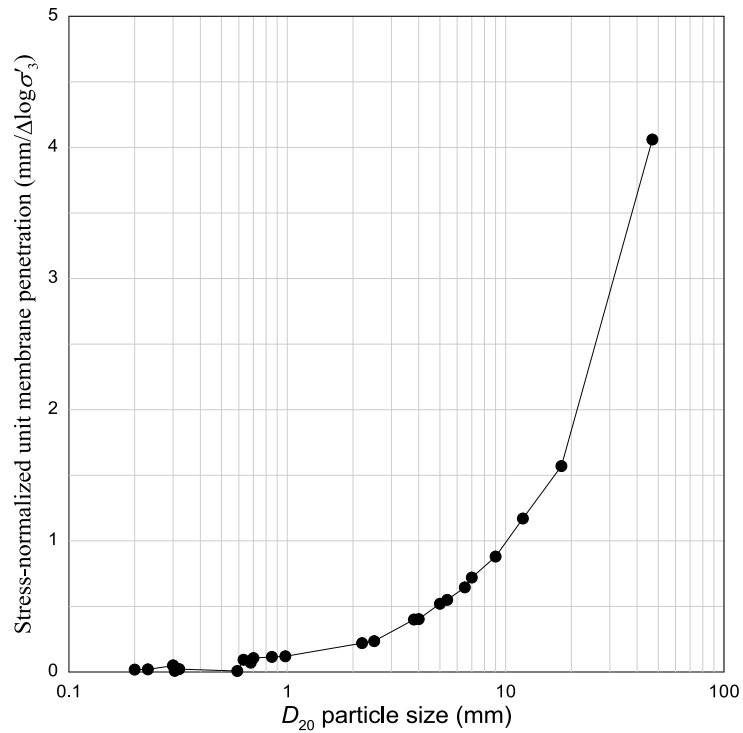


Figure 2.9 Effect of nominal particle size  $d_{20}$  on the stress-normalized unit membrane penetration (modified after Nicholson et al. 1993).

The ideal method to evaluate membrane penetration relies upon direct measurement of the true radial strain in the specimen. In the absence of local strain transducers, Eq. 2.2 is superior to all other methods presented in the literature to evaluate membrane penetration during *LSTX* testing of geomaterials with particle sizes larger than 3 mm.

### 2.2.5 Specimen Preparation and Uniformity

It is well known that the mechanical response of a geomaterial is significantly affected by the method of reconstitution (Vaid et al. 1999). In geomaterials with a wide range of particle sizes, such as *MWR*, these effects are more pronounced due to the difficulty in avoiding segregation (or maintaining homogeneity) in/of the finer fractions filling the larger void spaces within the soil matrix.

Commonly used reconstitution techniques for *LSTX* specimens of granular soils with large particle sizes are: (1) Moist tamping (Bathhurst and Kapurapu 1993, Alva-Hurtado et al. 1981); (2) air (or dry) pluviation (Bathhurst and Kapurapu 1993); and (3) vibratory compaction (Chavez et al. 2009, Sevi et al. 2009, Varadarajan 2003, Indraratna 1993). Experimental evidence has shown that loose specimens of sand reconstituted to the exact same state in terms of relative density and mean effective confining stress behave differently depending upon the method of reconstitution (Vaid et al. 1999). Air pluviation creates relatively loose specimens, while vibratory compaction is typically required to achieve high relative density ( $D_R > 60\%$ ) in geomaterials with large particle sizes, such as *MWR* (Chavez et al. 2009, Sevi et al. 2009, Varadarajan 2003, Indraratna 1993).

### 2.3 Particle Breakage

Traditionally, peak shearing resistance mobilized in soil is considered to be primarily dependent upon: (1) inter-particle friction and (2) the geometry of volumetric deformation that is necessary for shearing to occur. Taylor (1948) considered shearing resistance to be a question of energy consumption such that external work is dissipated by

internal friction and volumetric changes. Rowe (1962) developed Taylor's original work equation into a stress-dilatancy relationship in which the components of shearing resistance due to inter-particle friction and volumetric changes are described mathematically by the critical state friction angle and dilatancy angle, respectively. However, in the presence of particle crushing, Taylor's work equation is invalidated as energy consumption due to particle breakage leads to additional work being dissipated within the soil element (Tarantino and Hyde 2005). In soil that may exhibit significant changes in particle size and/or shape during loading, a third component associated with energy dissipation due to particle breakage is required for an accurate analysis of the mechanical response.

Vesic and Clough (1968) identified an isotropic "breakdown stress" which is defined as the point where the effect of the initial void ratio is completely destroyed as grains crush instead of dilating during axisymmetric compression. After this breakdown stress is exceeded, an initially dense soil element will exhibit contractive, strain hardening behavior. Beyond the breakdown stress, the sand behaves as a linearly deformable solid, with a modulus of deformation that is proportional to  $p'$ . This breakdown stress was measured to be about 20,000 kPa for Chattahooche River sand. The peak friction angle ( $\phi_p$ ) is shown to have a linear dependence on the logarithm of  $p'$  until the point where the breakdown stress is achieved. After this point,  $\phi_p$  becomes constant with respect to  $p'$ .

Varadarajan et al. (2003) tested three reduced parallel particle size distributions of two geomaterials (Fig. 2.10) in a *LSTX* apparatus over a range of  $p' = 300 - 1400$  kPa with

$d_{max}$  equal to 25, 80, and 120 mm with constant  $D_R = 87\%$ . The Purulia Dam material was a sub-rounded alluvial fill and the Ranjit Sagar Dam materials was an angular, blasted, sedimentary rockfill. As seen in the particle size distributions of the two materials in Figure 2.10, the alluvial fill contained some fines, and the modeled gradations were maintained parallel up to the 0.075 mm (#200) sieve.

Varadarajan et al. (2003) quantified particle breakage through the breakage factor ( $B_g$ ) presented by Marsal (1969).  $B_g$  requires a sieve analysis before and after testing and is defined as the sum of the increases in the percent mass retained on each sieve size used to perform the gradations (Marsal 1973).  $B_g$  may also be defined as the sum of the decreases in the percent mass retained for each sieve size used to perform the gradations (Marsal 1973).  $B_g$  was shown to increase with increasing particle size, mean effective stress, and angularity for specimens containing parallel particle size distributions of an angular, blasted sedimentary rockfill subjected to *CID LSTX* testing (Figure 2.10). This is interesting since the *MWR* tested in this study is a relatively weak sedimentary rock material with large, angular particles.

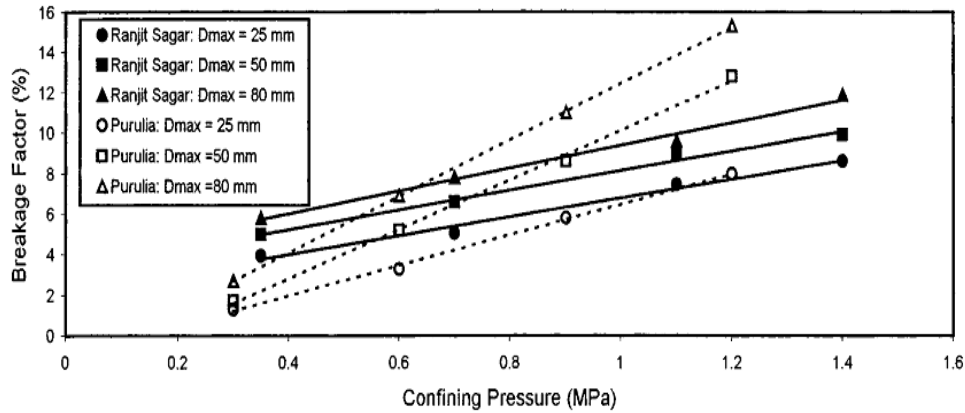


Figure 2.10 Influence of  $p'$  (confining pressure), particle size and particle shape on particle breakage for monotonic  $CID$  testing at  $D_R = 87\%$ . (Purulia = angular, blasted rockfill, Ranjit Sagar = rounded alluvial rockfill) (Modeled after Varadarajan et al. 2003).

Particle breakage has been shown previously (Hardin 1985, Marsal 1973) to increase with: (1) increasing uniformity of the particle size distribution, (2) increasing particle angularity, (3) increasing mean effective stress, (4) increasing initial density, (5) decreasing particle strength and (6) decreasing saturation conditions. Particle breakage has been shown to occur during  $LSTX$  testing of geomaterials, which can further influence their mechanical response (Marsal 1973, Marachi 1969, Lee and Farmoohand 1967, Varadarajan 2003). The critical state of a geomaterial is conceptually defined as the equilibrium state where no further changes in volume or stress state occur with increased deformation (Muir-Wood 1990, Schofield and Wroth 1968). In geomaterials with crushable grains, the apparent critical state friction angle ( $\phi_c^*$ ) measured in triaxial testing at maximum levels of strain does not always satisfy these constant volume and stress state conditions (Tarantino and Hyde 2005). Observed constant volume conditions may be nothing more than transient equilibrium between contractive strains due to particle breakage and dilative strains due to particle interlocking (Coop et al. 2004).

Ueng and Chen (2000) separated the  $\phi_p$  components of for two different sands (Fulung River and Tamsui River sands) and a decomposed granite previously tested by Miura and O-hara (1979) into: (1) the friction angle excluding both particle breakage and dilatancy ( $\phi_c$ ), thus equivalent to the critical state friction angle ( $\phi_c$ ), and (2) the friction angle excluding dilatancy and including particle breakage ( $\phi_{tb}$ ), to determine the actual contribution of particle breakage (i.e.,  $\phi_{tb} - \phi_c$ ) on  $\phi_p$ . The relative effect of particle breakage on the  $\phi_p$  values of the three different materials studied by Ueng and Chen always increased with increasing initial  $p'$  (after isotropic compression) used in the tests (Fulung sand results are shown in Fig. 2.11), whereas the magnitude of particle breakage was inversely proportional to the grain tensile strength of the material (Ueng and Chen 2000).

Indraratna and Salim (2002) followed a procedure similar to that outlined by Ueng and Chen (2000) to evaluate the amount of particle breakage of latite basalt with maximum particle size of 53 mm using a 300-mm-diameter LSTX apparatus. The relative effect of particle breakage on the  $\phi_p$  values of the latite basalt with large particle sizes was of the same order of magnitude as that reported by Ueng and Chen (2000) for the Fulung sand, which had strong grains. This effect may be quantified by evaluating the  $(\phi_{tb} - \phi_c)/\phi_p$  ratio for some of the highest  $p'$  levels used in the tests for both the Fulung sand and the latite basalt ( $p' \approx 300$  to 383 kPa), which yields a  $(\phi_{tb} - \phi_c)/\phi_p$  ratio of about 8-9% for both materials. This value is much lower than the typical  $(\phi_{tb} - \phi_c)/\phi_p$  ratio of about 16-21%

observed for the other two materials with weak grains (Tamsui River sand and dense decomposed granite) studied by Ueng and Chen.

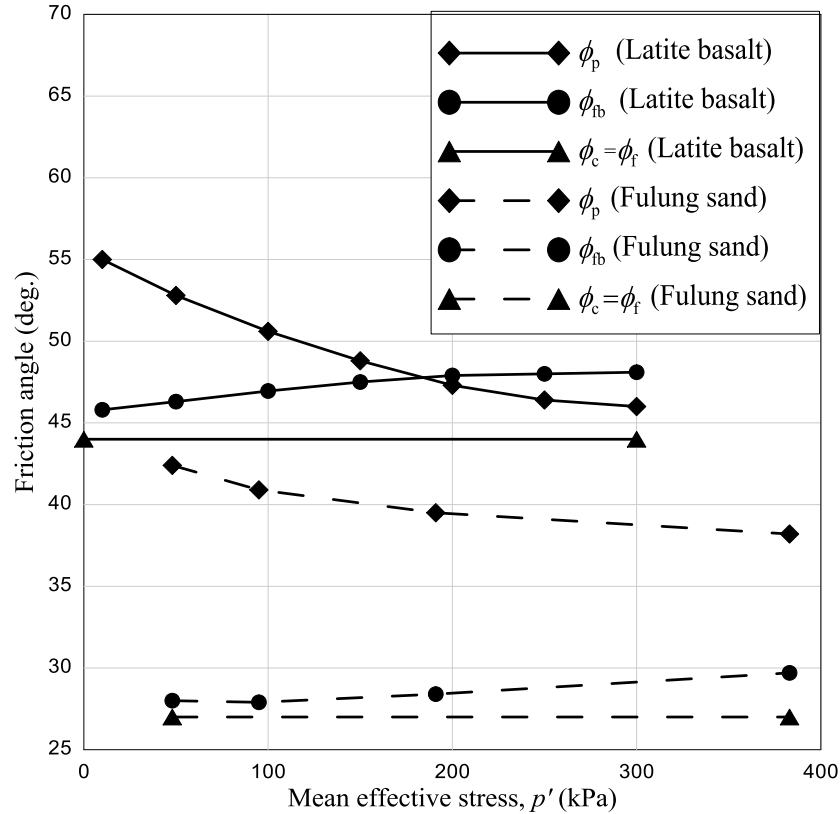


Figure 2.11 Effect of mean effective stress (after isotropic compression) on the peak friction angle and particle breakage of Fulung sand (Ueng and Chen 2000) and Latite basalt (Indraratna and Salim 2002).

For geomaterials with low grain strength and/or subjected to higher  $p'$  levels, the procedure outlined by Ueng and Chen (2000) can be used to systematically quantify the impact of particle breakage on the shear strength of a material at any level of deformation. However, one of the challenges associated with the approach outlined by Ueng and Chen (2000) is the necessity to complete an extensive amount of tests.

Coop et al. (2004) completed ring shear tests on Dog's Bay sand and showed that particle breakage increased until a 'true' critical state friction angle was achieved at strain levels between 2000% and 11000%. However, this 'true' critical state friction angle was of the same magnitude (+/- 2°) as that mobilized at shear strains of about 30%.

McDowell et al. (1996) used a micromechanics approach to identify some of the more fundamental factors affecting the crushing strength of individual grains within a soil matrix. Coordination number, particle size, and macroscopic stress state are identified as more fundamental factors affecting particle breakage observed for a wide range of geomaterials (in terms of mineralogy, particle size, particle shape, particle strength) loaded with a wide range of boundary conditions (Hardin 1985). Using a theory of successive fractal failure of the smallest grain sizes due to the macroscopic stress applied to the surface of the grain, a numerical model of crushable aggregates was developed and results of the model were compared with previously published 1-D consolidation test data. The model is based upon Weibull fracture statistics which requires evaluation of the Weibull modulus. The Weibull modulus increases with increasing variability in material strength. Results from the modeling and literature each show particle size distributions approaching a constant uniformity coefficient ( $C_u$ ) and also illustrate the effect of grain strength on the linear semi-logarithmic relationship between  $\phi_b$  and  $p'$  by normalizing  $p'$  by grain tensile strength. The authors modified Taylor's 1948 work dissipation equation to include a term for particle breakage (Eq. 2.3) by assuming that particles evolve toward a constant fractal dimension

$$q\delta\varepsilon_q^p + p'\delta\varepsilon_p^p = Mp'\delta\varepsilon_q^p + \frac{\Gamma dS}{V_s(1+e)} \quad (2.3)$$

where  $\Gamma_{se}$  = surface energy, and  $dS$  is the change in surface area of a volume of solids,  $V_s$ , distributed throughout a total specific volume of  $(1+e)$ .

### 2.3.1 Fractal Dimension

Fuller and Thompson (1907) noted a maximum-density particle size distribution curve which could be used as a boundary value for concrete design. The shape of this particle size distribution is similar to the shape of particle size distribution curves noted by Lade and Overton (1989) for many previous studies involving triaxial testing at very high levels of  $p'$  (10 - 100 MPa). Triaxial testing at these levels of  $p'$  (10 - 100 MPa) was shown to create very uniquely shaped particle size distributions after testing (Lade and Overton 1989, Vesic and Clough 1968). The shape of this curve is independent of the maximum particle size and the initial particle size distribution. The shape of this curve is also related to the so-called fractal dimension. Fractal dimensions are used to quantify scale-invariant processes shown to exist throughout the universe (Mandelbrot 1982). A wide range of crushed materials were shown by Turcotte (1986) to contain a fractal dimension in the distribution of particles after subjecting the materials to a wide variety of crushing forces ranging from underground nuclear explosions to shattered ceramics. The modified work equation (Eq. 2.3) presented by McDowell et al. (1996) assumes that crushable materials evolve towards a constant, maximum fractal dimension. Evaluating Eq. 2.3 requires determination of the fractal dimension of the material after testing. Determining the fractal dimension of a distribution of particles requires knowledge of the specific gravity, total mass and relative distribution of mass between characteristic particle sizes (i.e. particle size distribution). Using a sieve analysis to determine the

particle size distribution before and after application of any state of stress to a crushable soil allows the evolution of the fractal dimension to be evaluated. Tarantino and Hyde (2005) confirmed the McDowell et al. (1996) modified work equation with experimental data for monogranular distributions of crushable carbonate sand (Dog's Bay sand). Using direct shear tests, a constant fractal dimension was established after shearing specimens at the highest normal stresses (1200-1400 kPa). This allowed the 'true' critical state friction angle to be evaluated, which would be, conceptually speaking, independent of particle breakage effects and does not require mobilization of strain levels on the order of 11,000%.

### 2.3.2 Particle Strength

It is generally accepted that failure of a spherical particle under compressive loading is a tensile failure (McDowell and Bolton 1998). The grain tensile strength of particle is typically measured in one of two ways: (1) point load strength (Broch and Franklin 1972) and (2) diametral compression between flat platens (Jaeger 1967). Each method involves a form of Eq. 2.4

$$\sigma = \left( \frac{F}{d^2} \right) \quad (2.4)$$

where  $F$  = compressive load,  $d$  = particle diameter, and  $\sigma$  = grain tensile stress induced in the particle. Broch and Franklin (1972) presented the point load strength test, which eventually became an ASTM standard for determining the relative strength of rocks. Billam (1972) noted the linear log-log relationship between  $d$  and  $\sigma$ , thus ASTM D5731-08 requires that the point load strength index values be normalized to a specific grain diameter (50-mm) in order to maintain comparable results according to Eq. 2.5

$$I_{s(50)} = \left( \frac{P}{D_e^2} \right) \cdot \left( \frac{D_e}{50} \right)^{0.45} \quad (2.5)$$

where  $I_{s(50)}$  = size corrected point load strength index calculated for an equivalent 50-mm core sample,  $P$  = compressive load required for failure and  $D_e$  = equivalent particle diameter. Results are normalized to a 50-mm diameter due the common use of 50-mm core samples in rock quality designations. Determination of  $D_e$  depends on the particle shape and failure surface noted in the particle after the test. ASTM D 5731-08 also presents a qualitative range of rock strengths based on  $I_{s(50)}$ : Extremely High ( $I_{s(50)} > 10$  MPa), Very High ( $3 > I_{s(50)} > 10$  MPa), High ( $1 < I_{s(50)} < 3$  MPa), Medium ( $1 < I_{s(50)} < 0.3$  MPa), Low ( $0.1 < I_{s(50)} < 0.3$  MPa), Very Low ( $0.03 < I_{s(50)} < 0.1$  MPa) and Extremely Low ( $I_{s(50)} < 0.03$  MPa). Due to the standardized nature and the large amount of data found in the literature, size corrected point load strength indices were considered to be the preferred method of determining the grain tensile strength of particles of unoxidized and oxidized *MWR*.

Lee (1992) noted that the difference ( $\phi_p - \phi_c$ ) is linearly dependent on the logarithm of  $p'$  normalized by grain tensile strength for specimens tested at the same initial  $D_R = 87\%$  (Figure 2.12).

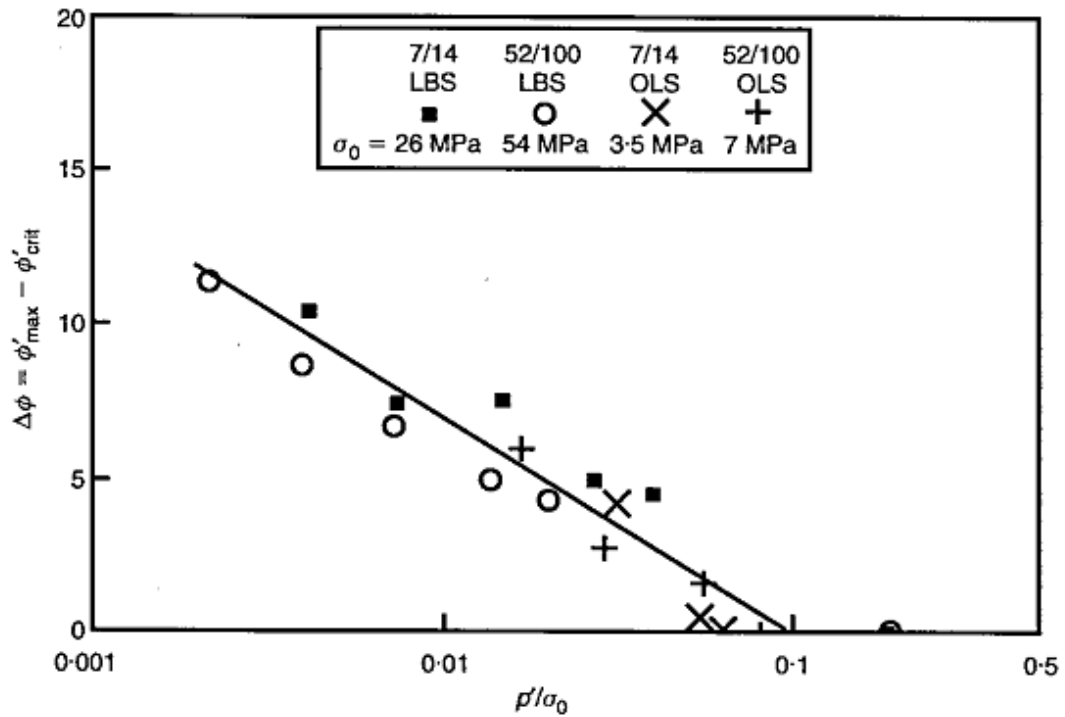


Figure 2.12 ( $\phi_p - \phi_c$ ) vs.  $p'$  normalized by grain tensile strength ( $\sigma_0$ ) for geomaterials with particle tensile strengths ranging from 3.5 – 54 MPa (replotted after Lee 1992).

### 2.3.3 Creep in granular Geomaterials

While the previous sections (2.1-2.3.2) are concerned with aspects of the mechanical behavior of geomaterials deformed at rates slow enough to avoid substantial excess pore pressure build up, much study has also been focused on understanding the long-term time-dependent mechanical properties of geomaterials with weak or degradation-prone particles. “Strength degradation” observed at various mine field sites related to physical and chemical degradation of *MWR* is an extremely complicated but important occurrence that is still not well understood.

Simple, qualitative testing procedures have been developed to give indication of potential physical degradation for *MWR* by describing material behavior when exposed to abrasion

or wetting (e.g. Slake Durability, L.A. Abrasion, Jar Slake, Free-swell, Micro-Deval, Sulfate Soundness). None give any quantitative description of how a testing procedure may change the intrinsic factors affecting the mechanical response of a given geomaterial, nor how these effects relate to actual field degradation. Observed effects typically depend more upon changes induced by the testing procedure, not those induced by years of exposure to a field environment. None of these procedures have been shown to be adequate for accurately describing the time-dependent strength degradation of *MWR*.

Aside from any physical or chemical weathering processes, the long-term time-dependent mechanical behavior of these geomaterials subjected to sustained loading is still not fully understood (Karimpour and Lade 2010, Oldecorp and Alonso 2007, McDowell and Bolton 1998). Oldecorp and Alonso (2007) presented a framework rooted in the phenomena of crack propagation induced by stress corrosion mechanisms to explain observed long-term time-dependent macroscopic deformations in large-scale 1-D consolidometer tests. This deformation is described through a closed-form relationship between the compressibility coefficient ( $\lambda$ ), the coefficient of delayed deformation ( $\lambda^t$ ), with a number of other parameters which are used to describe the rate of crack propagation. Experimental data are also presented confirming the applicability of the proposed concept (Oldecorp and Alonso 2007). Karimpour and Lade (2010) focused on time dependent compressibility due to delayed fracture or static fatigue. Loading conditions in triaxial tests were sustained for varying periods of time and long-term deformations were monitored. Particle-size distributions were taken before and after each

tested loading condition and time period. Experimental results indicate the relationship between particle breakage and loading time may be significant. This fact makes the evaluation of long-term mechanical degradation even more complicated. The mechanical response of some geomaterials seems to be inherently time dependent, aside from any chemical or physical weathering processes.

With these results in mind, all loading times must be held constant between all triaxial tests if comparable results are expected. Also, observed “degradation” in the field may in fact be nothing more than constant loading deformations described by Karimpour and Lade (2010) and Oldecorp and Alonso (2007) for materials with crushable grains.

#### 2.4 Acid-base Accounting

When referring to geomaterials, the term “weathering” has many meanings (Ollier 1969). Chemical weathering may be defined as a “natural soil process which occurs under prevailing environmental conditions resulting in the transfer of matter from unstable mineral phases to more stable mineral phases” (Essington 2004). Chemical weathering typically occurs due to hydrolysis, oxidation, dissolution, or biological processes. Mechanical or physical weathering is related to the breakdown of rocks and soils due to abrasive contact with environmental elements, such as heat water, ice and air (Ollier 1969). Freeze-thaw, salt wedging, unloading, and thermal stress are typical physical weathering processes. As mentioned in Section 2.3, these processes often occur concurrently, making the establishment of a link between a single weathering process and the degradation of mechanical strength associated with that weathering process a difficult

task. The *MWR* materials tested in this study are referred to as “oxidized” and “unoxidized”. These designations are based upon visual observations that the “oxidized” material appeared to be heavily weathered by oxidation relative to the unoxidized material even though the materials were blasted from the same geologic unit on the same day. These differences may be due to the massive faulting and hydrothermal intrusions which occurred in the area during mineralization of the precious metals beneath the overburden Ordovician Vinini geologic unit which the *MWR* materials were taken from (Jory 1999, Albino 1993), although the exact difference in the hydrogeologic history of the two *MWR* materials is unknown. The differences between the two *MWR* materials may also be partially due to other weathering processes (such as hydrolysis and dissolution) and the differences between the two *MWR* materials may not necessarily be limited to weathering by oxidation alone.

In the most fundamental definition, oxidation may be referred to as a process of electron transfer. Oxidation in geomaterials typically involves oxidation of metals into metal oxides and hydroxides in the presence of water, oxygen and unoxidized mineral surfaces. In *MWR* materials which typically overlie a precious metal deposit, sulfide minerals, such as pyrite, are common and quite susceptible to weathering by oxidation. Oxidation of pyrite may be one of the primary weathering processes in a *MWR* material and is considered to be the primary contributor to acid mine drainage (Ardua et al. 2008, Essington 2004, Kargbo and He 2004, Sobek et al. 1972). A common method for characterizing the acid producing capacity of geologic materials is termed acid-base accounting (*ABA*). *ABA* may also be used to evaluate the relative level of weathering by

oxidation between two originally similar geomaterials (Ardua et al. 2008, Essington 2004, Kargbo and He 2004, Sobek et al. 1972).

## 2.5 Summary

Main conclusions of the comprehensive literature review presented in this chapter are as follows.

*LSTX* testing:

- (1) Parallel particle-size distributions have been shown to be the best particle size reduction technique for achieving consistent mechanical response between field-scale materials and laboratory test specimens.
- (2) Adoption of a minimum sample size ratio of six and specimen diameters of at least 150 mm, along with the use of parallel gradations allow reasonable estimation of the peak friction angle of mine waste rock, rockfill, coarse aggregates and other geomaterials with large particle sizes.
- (3) Critical state and dilatancy are the two most fundamental aspects associated with the proper evaluation of the shear strength of geomaterials. Proper evaluation of these important aspects of geomaterial behavior can be carried out by systematically taking into account the effects of the main state variables (density and mean effective stress) during characterization of the intrinsic parameters (e.g., critical-state friction angle, Bolton's correlation parameters  $Q$  and  $R$  for the peak friction angle, and the maximum and minimum void ratios) of the material.

- (4) Determination of the intrinsic parameters mentioned above requires the use of an appropriate large-scale triaxial protocol. In turn, this more rigorous and fundamental approach would allow robust and more comprehensive predictions of the shear strength of mine waste rock, rockfill, coarse aggregates and other geomaterials with large particle sizes to be made for the most relevant combinations of density and mean effective stress encountered in geotechnical and mining applications.
- (5) Properly accounting for volume change due to membrane penetration is an essential component of *LSTX* testing.
- (6) Particle breakage increases with particle size and has been shown to be a significant component of the mobilized friction angle ( $\phi$ ) in materials with relatively weak particles.

#### Particle Breakage:

- (1) The stress-dilatancy relationship may be significantly affected by particle crushing in geomaterials with large, weak or very angular particles.
- (2) Dilatancy is reduced as particle breakage increases.
- (3) Particle crushing leads to dissipation of energy which is not accounted for in the classic Taylor (1948) work equation.
- (4) Energy consumption due to particle breakage may be accounted for using a form of Taylor (1948) work equation modified by McDowell et al. (1996).
- (5) Time dependent particle crushing may explain observed “strength degradation” in embankments constructed using *MWR* materials.

Acid-base accounting (*ABA*):

- (1) The relative level of weathering by oxidation between two originally similar geomaterials may be quantified with *ABA* and may be described using *NP* and *AP*.
- (2) Comparing *AP* and *NP* values may also be helpful in describing differences in the mechanical response of an originally similar geomaterials which have been subjected to varying levels of weathering by oxidation.

## CHAPTER 3: CONCEPTUAL FRAMEWORK

Critical state soil mechanics was used in this study as a starting point to develop a framework to systematically evaluate differences in the intrinsic mechanical characteristics of unoxidized and oxidized mine waste rock (*MWR*). A systematic, rigorous analysis of the mechanical behavior of *MWR* will provide a better understanding of the effects of *in situ* weathering on the mechanical response of *MWR*. Due to the nature of *MWR*, a rigorous conceptual framework is needed to evaluate aspects of energy consumption during shearing due to (1) intrinsic, frictional material characteristics, (2) interlocking or dilatancy, and (3) particle breakage. The relationship between dilatancy and particle breakage depends on the particle tensile strengths (McDowell et al. 2002, Lee 1992, Billam 1972), while intrinsic frictional characteristics may be best described through the critical state friction angle ( $\phi_c$ ). A rigorous framework should carefully consider both state variables and intrinsic parameters known to significantly affect the mechanical behavior of geomaterials. Intrinsic parameters are uniquely defined for a specific geomaterial and remain independent of its current state. On the other hand, stress, density, and fabric represent typical examples of state variables that fundamentally affect the mechanical behavior of geomaterials (Salgado 2008).

### 3.1 Critical State Friction Angle

Rowe (1962) extended the original Taylor (1948) work equation into a stress-dilatancy relationship in which the components of shearing resistance due to constant-volume inter-

particle friction and interlocking are described mathematically by the critical state friction angle ( $\phi_c$ ) and dilatancy angle ( $\psi$ ), respectively, resulting in Eq. 3.1:

$$\phi = \phi_c + \psi \quad (3.1)$$

where  $\phi$  = the mobilized friction angle.

Eq 3.1 may also be expressed in terms of the stress components acting on the plane of shearing using Eq 3.2:

$$\left( \frac{\tau}{\sigma'} \right) = \tan(\phi) = \tan(\phi_c + \psi) \quad (3.2)$$

where  $\tau$  = shear stress and  $\sigma'$  = normal effective stress.

For axisymmetric conditions, such as those associated with triaxial testing,  $\phi$  of an uncemented geomaterial may be deduced from the Mohr's circle of stress through Eq. 3.3:

$$\sin(\phi) = \frac{\frac{\sigma'_1}{\sigma'_3} - 1}{\frac{\sigma'_1}{\sigma'_3} + 1} \quad (3.3)$$

where  $\sigma'_1$  = major principal effective stress,  $\sigma'_3$  = minor principal effective stress, and  $\sigma'_1 / \sigma'_3 = N$  = flow number, stress obliquity, or effective principal stress ratio.

The mobilized friction angle represents the frictional resistance which may be mobilized in a soil element at a specific level of deformation.  $\phi$  may contain indistinguishable components of shearing strength associated with: (1) intergranular friction and (2) interlocking or dilatancy. The critical state friction angle,  $\phi_c$  is more rigorously defined as

the friction angle mobilized in a soil element when the rate of change in both volume and state of stress approach zero with continued deformation. This so-called critical-state is observed to occur in triaxial specimens of typical geomaterials (e.g. sands, silts, and clays) at the highest levels of axial strain (typically 20-30%).

The so-called critical state line (CSL) represents a line in  $p' - q - v$  space which is considered to be unique to a given soil (Schofield and Wroth 1968). This CSL is described using two simple equations (Eqs. 3.4 and 3.5) defined at critical state conditions:

$$q_{cs} = M \cdot p'_{cs} \quad (3.4)$$

and

$$v_{cs} = \lambda_{cs} \cdot \ln(p'_{cs}) + \Gamma_{cs} \quad (3.5)$$

where  $q_{cs}$  = deviatoric stress invariant,  $p'_{cs}$  = mean effective stress at the critical state,  $v_{cs}$  = specific volume at the critical state,  $M$  and  $\lambda_{cs}$  = critical state soil parameters describing the slope of the CSL in  $p' - q$  and  $p' - v$  space, respectively, and  $\Gamma_{cs}$  = critical state soil parameter describing the intercept of the CSL at  $p' = 1$  kPa (Muir-Wood 1990).

Soil elements subjected to normal isotropic compression at sufficiently high  $p'$  follow a unique normal compression line (NCL) in  $p' - v$  space which may be described (Eq 3.6) in a similar manner as the CSL:

$$v = N - \lambda \cdot \ln(p') \quad (3.6)$$

where  $\lambda$  and  $N$  are critical state parameters describing the slope and intercept of the NCL in  $p'$ - $v$  space at  $p' = 1$  kPa, respectively (Muir-Wood 1990).

Soil elements which are subjected to levels of  $p'$  which are not sufficiently elevated to approach a unique NCL are considered to follow the unloading-reloading line (*URL*) according to Eq. 3.7:

$$v = v_{\kappa} - \kappa \cdot \ln(p') \quad (3.7)$$

where  $\kappa$  and  $v$  are critical state parameters describing the slope and intercept of the *URL* at  $p' = 1$  kPa (Muir-Wood 1990).

### 3.2 Stress-Dilatancy Relationship

A stress-dilatancy relationship for plane strain based on minimum energy assumptions (Rowe 1962, De Josselin de Jong 1976) can be described using Eq. 3.8 as:

$$N = M \cdot N_c \quad (3.8)$$

where  $N_c$  = flow number at critical state;  $M$  = dilatancy number =  $1 - d\varepsilon_p/d\varepsilon_1$ , with  $d\varepsilon_1$  and  $d\varepsilon_p$  = major principal strain and volumetric strain increments, respectively;  $N_c$  and  $M$  can be expressed in terms of  $\phi_c$  and the dilatancy angle ( $\psi$ ) according to Eq. 3.9 and Eq. 3.10 as:

$$N_c = \frac{1 + \sin \phi_c}{1 - \sin \phi_c} = \tan^2 \left( 45^\circ + \frac{\phi_c}{2} \right) \quad (3.9)$$

$$M = \frac{1 + \sin \psi}{1 - \sin \psi} = \tan^2 \left( 45^\circ + \frac{\psi}{2} \right) \quad (3.10)$$

The value of  $\psi$  is observed to approach a maximum at the maximum dilatancy rate in typical granular geomaterials (Schofield and Wroth 1968) and can be deduced for axisymmetric conditions (Eq. 3.11) from the Mohr's circle of strain as:

$$\sin \psi = -\frac{\frac{d\varepsilon_1}{2d\varepsilon_3} + 1}{\frac{d\varepsilon_1}{2d\varepsilon_3} - 1} \quad (3.11)$$

where  $d\varepsilon_3$  = minor principal strain increment.

Bolton (1986) observed the overestimation of  $\psi$  when comparing the theoretical stress-dilatancy relationship proposed by Rowe (1962) with a large database of actual laboratory tests completed on 17 different clean sands. These tests were completed on sands by independent research groups in both plane strain and axisymmetric loading conditions, showing an overestimation of about 20% for values of  $\psi$ . In other words, Bolton proposed Eq. 3.12 as a more appropriate expression for distinguishing between the peak and critical state components of shearing resistance.

$$\phi_p = \phi_c + 0.8 \psi \quad (3.12)$$

Bolton (1986) further proposed that the relationship between  $\phi_c$  and the mobilized friction angle at peak conditions,  $\phi_p$ , be expressed (Eq. 3.13) for plane-strain and axisymmetric conditions using the relative dilatancy index,  $I_R$ :

$$\phi_p - \phi_c = A_\psi I_R \quad (3.13)$$

where  $A_\psi$  is equal to 3 and 5, for axisymmetric and plane-strain conditions, respectively.

For each set of boundary conditions,  $I_R$  is expressed through Eq. 3.14 as:

$$I_R = -\frac{10}{3} \left( \frac{d\varepsilon_p}{d\varepsilon_1} \right)_{\max} \quad (3.14)$$

and may be related to state variables of relative density ( $D_R$ ) and the peak mean effective stress, ( $p'_p$ ) through Eq. 3.15:

$$I_R = \left[ \frac{D_R}{100} \left( Q - \ln \left( \frac{100 p'_p}{p_A} \right) \right) - R \right] \quad (3.15)$$

where  $p_A$  = reference stress (=100 kPa, for  $p'_p$  in kPa);  $Q$ ,  $R$  and  $\phi_c$  are intrinsic parameters that can be determined for various geomaterials such as clean sands (Bolton 1986), nonplastic silty sands (Salgado et al. 2000), and mixtures of sands with either plastic or nonplastic fines (Carraro et al. 2009). Equations 3.14 and 3.15 are valid for  $0 \leq I_R \leq 4$ . For higher values of  $I_R$ , the value of peak friction angle is taken as the value calculated from Eq. 3.14 with  $I_R = 4$ .

By performing a series of *LSTX* tests over a wide range of controlled levels of state variables, these intrinsic parameters ( $\phi_c$ ,  $Q$  and  $R$ ) can also be determined for any uncemented geomaterial to allow prediction of the  $\phi_p$  of the material under any state, even in the presence of particle breakage. Figure 3.1 schematically illustrates this point for a hypothetical geomaterial with  $Q$ ,  $R$  and  $\phi_c$  equal to 10, 1 and  $30^\circ$ , respectively, where the axisymmetric (or triaxial) deviatoric stress invariant is defined as  $q = \sigma'_a - \sigma'_r$  where  $\sigma'_a$  = effective axial stress and  $\sigma'_r$  = effective radial stress. The critical state line (CSL) and the peak failure envelopes were synthetically determined using these assumed parameters. This procedure is also outlined in detail by Salgado (2008), showing actual experimental data at various combinations of  $D_R$  and  $p'$  (Fig. 3.1).

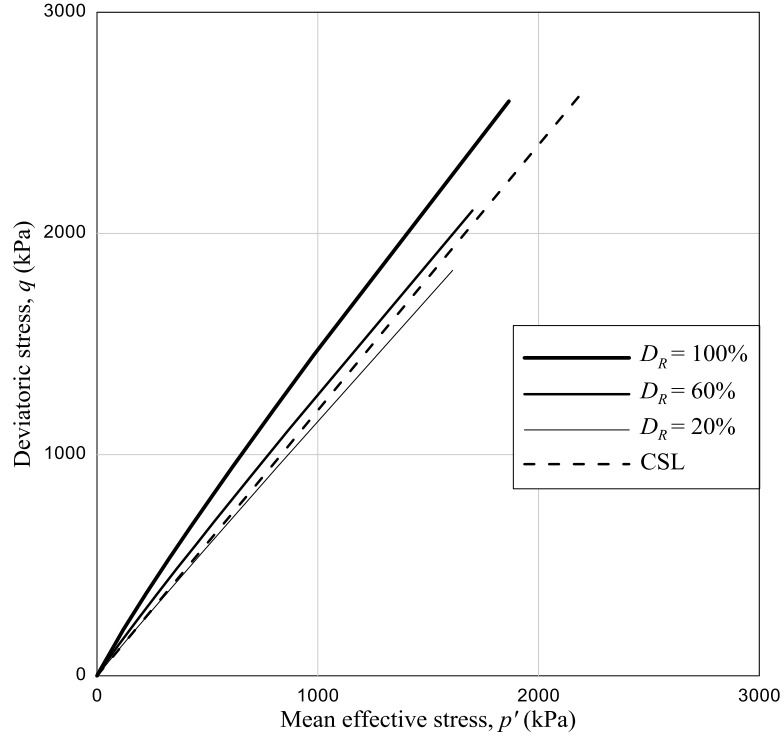


Figure 3.1 Schematic representation of the critical state line and various peak failure envelopes for a hypothetical geomaterial (with  $Q = 10$ ,  $R = 1$  and  $\phi_c = 30^\circ$ ) for various combinations of relative density and mean effective stress

### 3.3 Particle Breakage

Particle breakage suppresses dilatancy and also increases the friction angle mobilized within a soil element (Tarantino and Hyde 2005, Coop et al. 2004). Dilatancy is also suppressed with increasing  $p'$  (Bolton 1986, Leps 1970). Conversely, dilatancy increases with increasing density. Bolton (1986) accounted for the effects of state variables ( $D_R$  and  $p'_p$ ) and particle breakage together through the relative dilatancy index,  $I_R$ . Using the intrinsic parameters  $Q$ ,  $R$  and  $\phi_c$  the relationship between peak and critical state friction angles of uncemented sands in axisymmetric (triaxial) compression can be described by rearranging Eq. 3.15 into:

$$I_R = \frac{\phi_p - \phi_c}{3} = I_D [Q - \ln(p'_p)] - R \quad (3.16)$$

The value of  $Q$  is related to the  $p'$  required to suppress dilatancy (Salgado 2000, McDowell and Bolton 1998) and is calculated to be less than 10 for geomaterials with weak grains. The relative grain tensile strength of geomaterials may be described both qualitatively and quantitatively by following ASTM D5731-08 “Determination of the Point Load Strength Index of Rock and Application to Rock Strength Applications” where particle strength is classified according to the measured value of size corrected point load strength ( $I_{s(50)}$ ) (see section 2.3.2 for more on particle strength). Bolton (1986) suggested a value of  $Q$  equal to 10 for quartz, 8 for limestone, 7 for anthracite, and 5.5 for chalk based on triaxial tests completed by Billam (1972) which show the reduction in  $p'$  required to suppress dilatancy for geomaterials with weaker particle strengths. Billam (1972) also established a link between the suppression of dilatancy and the grain tensile strength by determining values of  $I_{s(50)}$  for these materials (quartz, limestone, anthracite, and chalk). Lee (1992) also noted that the dilatancy angle  $\psi$  is linearly dependent on the logarithm of  $p'$  normalized by grain tensile strength for crushable materials.

While the Bolton (1986) equation does not explicitly account for energy consumption due to particle breakage effects,  $I_R$  describes the suppression of dilatancy due to combined increases in  $p'$  and particle breakage together empirically through the intrinsic material parameters  $Q$  and  $R$ . In the absence of particle breakage, increases in  $p'$  suppress dilation for geomaterials with relatively high grain strength, whereas increases in  $D_R$  increase dilatancy. In the presence of particle breakage, the effects of  $p'$ ,  $D_R$  and particle breakage on dilatancy are indistinguishable components of  $I_R$ .

Taylor (1948) considered the constitutive behavior of a soil element from the perspective of energy consumption such that the externally applied work induced during loading is dissipated by internal friction and volumetric changes as described by Equation 3.17, where  $T_f$  = shearing force,  $N_f$  = normal force,  $\mu$  = coefficient of frictional resistance,  $dx$  = finite displacement in the direction of shearing, and  $dy$  = finite displacement perpendicular to the plane of shearing, in the direction of normal loading.

$$T_f dx - N_f dy = \mu N_f dx \quad (3.17)$$

Equation 3.17 may also be represented through the Cam Clay model (Eq. 3.18) (Roscoe et al. 1963, Schofield and Wroth 1968), using the octahedral mean stress invariant  $p'$ , deviatoric stress invariant  $q$ , and the corresponding plastic-strain increments,  $\delta\varepsilon_q^p$  and  $\delta\varepsilon_p^p$

$$q\delta\varepsilon_q^p + p'\delta\varepsilon_p^p = Mp'\delta\varepsilon_q^p \quad (3.18)$$

By assuming elastic strains are equal to zero, the Cam Clay work equation (Roscoe et al. 1963) reduces to the following Granta gravel work equation (Eq. 3.19) (McDowell and Bolton 1998, Schofield and Wroth 1968):

$$q\delta\varepsilon_q + p'\delta\varepsilon_p = Mp'\delta\varepsilon_q \quad (3.19)$$

where  $\delta\varepsilon_q$  = deviatoric strain increment and  $\delta\varepsilon_p$  = octahedral mean strain increment.

In the presence of particle breakage, Taylor's work equation is invalidated as energy consumption due to particle breakage leads to additional work being dissipated within the soil element (Tarantino and Hyde 2005). McDowell et al. (1996) added an additional term to the Granta gravel work equation in order to account for energy consumption due to particle breakage. This revised relationship assumes that an element of crushable

particles subjected to compressive loading will evolve toward a fractal dimension  $D$  through Eq. 3.20:

$$q\delta\varepsilon_q + p'\delta\varepsilon_p = Mp'\delta\varepsilon_q + \frac{\Gamma_{se}dS}{V_s(1+e)} \quad (3.20)$$

where  $\Gamma_{se}$  = surface energy; and  $dS$  is the change in surface area of a volume of solids,  $V_s$  distributed throughout a specific volume of  $(1+e)$ .

### 3.3.1 Fractal Dimension

An accurate description of the mechanical behavior of geomaterials that experience particle breakage during compressive loading requires distinguishing between the components of particle breakage and dilatancy due to the time dependence of particle breakage (Karimpour and Lade 2010). This distinction requires evaluation of the so-called fractal dimension,  $D$ , of the material before and after loading in order to evaluate Eq. 3.20. Fractal dimensions are used to quantify scale-invariant processes shown to exist throughout the universe (Mandelbrot 1982). A wide range of crushed materials were shown by Turcotte (1986) to contain a fractal dimension in the distribution of particles after subjecting the materials to a wide variety of crushing forces ranging from underground nuclear explosions to shattered ceramics. The fractal dimension of a crushed material defines a simple power law relationship between the number of particles and their size (McDowell and Bolton 1998). If a distribution of particles satisfies a log-linear relationship between a given characteristic particle size  $d$  and the number of particles with a characteristic particle size greater than  $d$ ,  $N(L>d)$ , then the material has a fractal character and the fractal dimension may be defined using Eq. 3.21:

$$N(L>d)=Ad^{-D} \quad (3.21)$$

where  $A$  is a constant of proportionality and  $D$  is the fractal dimension.

Determining the fractal dimension of a distribution of particles requires knowledge of the specific gravity, total mass, and the relative distribution of mass between particles with a characteristic particle size (Tarantino and Hyde 2005). Determination of  $D$  may be completed for a soil mass by calculating the particle-size distribution, specific gravity and average particle shape of the soil mass. Analysis of particle-size distributions before and after application of any state of stress to a crushable soil allows for the evolution of  $D$  to be evaluated if the particle shapes are assumed to remain relatively constant. If the fractal dimension approaches a constant value at the highest levels of loading, a truly intrinsic, critical state friction angle, which is independent of any dilatancy or particle breakage effects may be determined for any geomaterial (Tarantino and Hyde 2005). The approach outlined by Tarantino and Hyde (2005) is based on the modified Granta gravel work equation (Eq. 3.20) presented by McDowell et al. (1996), which includes a term for particle breakage by assuming that particles evolve towards a constant  $D$  during compressive loading. Particle breakage will be evaluated in this study by measuring changes in the particle-size distribution of *LSTX* specimens after drained axisymmetric triaxial compression allowing for changes in the  $D$  to be evaluated as well. If a constant  $D$  is in fact approached, an independent evaluation of energy consumption due to (1) dilatancy and (2) particle breakage may be evaluated during drained axisymmetric loading of the *MWR* tested in this study.

### 3.3.1.1 Surface Energy

A reliable estimate for the value of the surface energy  $\Gamma_{se}$  will be necessary in order to evaluate the modified work equation (Eq. 3.20). While determining the surface energy of a liquid is a relatively simple task, determining the surface energy of solids has eluded understanding and evaded measurement (Kendall et al. 1987). Classical approaches proposed by Griffith (1920) and Barenblatt (1962) have been shown to be inadequate, while more recent approaches have significant limitations, such as temperature range during measurement (Yudin and Hughes 1994). Freidman et al. (1972) also noted the differences in the value of  $\Gamma_{se}$  calculated for single crystals ( $0.2 - 10 \text{ J/m}^2$ ) is much less than the value calculated for larger rock pieces ( $3 - 50 \text{ J/m}^2$ ). Shaevich (2007) recognized that even in this day and age “measurement of surface energy for solids is a problem that is difficult to resolve.”

### 3.3.1.2 Surface Area

Evaluating the change in surface area ( $dS$ ) of a volume of soil requires a relationship between the mass, volume and surface area for particles retained on a given sieve. The simplest approach is the assumption that particles have perfectly spherical shapes before and after testing, although this assumption is likely not valid for the angularly shaped *MWR* tested in this study. In the development of Eq. 3.20, McDowell and Bolton (1998) presented two simple parameters (Eqs. 3.22 & 3.23) to link the relationships between the volume, mass, surface area and nominal particle size  $d$  (i.e. sieve size) for particles with non-spherical shapes:

$$\beta_v = \frac{V}{d^3} \tag{3.22}$$

and

$$\beta_s = \frac{S}{d^2} \quad (3.22)$$

where  $\beta_v$  = the volume shape factor;  $\beta_s$  = the surface shape factor;  $V$  = the volume of a particle and  $S$  = surface area of a particle.

Perfectly spherical particle shapes give  $\beta_v = 0.52$  and  $\beta_s = 3.14$ . Golithy (1989) evaluated the sphericity, roundness and length/width ratios of particles of Dog's Bay sand, which is a widely tested crushable carbonate beach sand consisting of angular, flakey, platey grains (Tarantino and Hyde 2005). Data from Golithy (1989) can be used to determine  $\beta_v = 0.2$  and  $\beta_s = 5.6$  for Dog's Bay sand (Tarantino and Hyde 2005).

Marsal (1973) described slightly different forms of shape and volume factors for angular rockfill materials with particle shapes which are observed to be very similar to the particle shapes of the *MWR* investigated in this study. Converting the Marsal (1973) shape and volume factors into the corresponding forms of shape and volume factors ( $\beta_v$  and  $\beta_s$ ) presented by McDowell and Bolton (1998) yields average values of  $\beta_v = 0.43$  and  $\beta_s = 3.46$  for six gradations of angular rockfill with a standard deviations between values of  $\beta_v$  and  $\beta_s$  equal to 0.04 and 0.72, respectively. These values of standard deviation indicate that values of  $\beta_v$  and  $\beta_s$  determined by Marsal (1973) are quite consistent between the six gradations of angular rockfill material and lie between what could be

considered limiting values of  $\beta_v$  and  $\beta_s$  determined for perfectly spherical and angular, flakey, platey particle shapes.

In this study, particle shape and volume factors were assumed to be equal to the average values reported by Marsal (1973) for six angular rockfills. By comparing final calculated values of  $dS$  and  $D$  calculated with  $\beta_v$  and  $\beta_s$  varying over the somewhat limiting values of  $\beta_v$  and  $\beta_s$  reported for spherical and platey particle shapes, the assumption of  $\beta_v = 0.43$  and  $\beta_s = 3.46$  was shown to have a relatively small impact on the final calculated values of  $dS$  and  $D$ .

### 3.3.2 Creep in Granular Geomaterials

Continued volume change observed after full dissipation of excess pore pressures due to compressive loading of soils with crushable grains has been well described by many authors (Karimpour and Lade 2010, Lade 2007, Oldecorp and Alonso 2007, Fabre and Pellet 2006, McDowell and Khan 2003, McDowell 2003, Lade 1994). Volume change due to creep is commonly observed to occur linearly with the logarithm of time. In this study, drained creep was evaluated during isotropic consolidation by monitoring changes in the triaxial specimen volume at specified time increments after the end of primary consolidation. Creep was monitored until the time rate of volumetric strain ( $\delta\varepsilon_p/\delta t$ ) was less than 0.05%/hour. Once this rate was achieved, consolidation was continued and  $p'$  was increased to the subsequent consolidation pressure. Achieving this rate typically required between 2 and 6 hours of drainage after full dissipation of excess pore pressures,

with the required time of drainage dependent upon the loading increment, specimen density, as well as the current and previous levels of  $p'$ .

### 3.4 Acid-base Accounting

A common method for characterizing the acidity and basicity of geologic materials is termed acid-base accounting (*ABA*) (Essington 2004). *ABA* considers net neutralization potential (*NNP*) (Eq. 3.24) or neutralization potential ratio (*NPR*) (Eq. 3.25):

$$NNP = NP - AP \quad (3.24)$$

and

$$NPR = NP/AP \quad (3.25)$$

where  $NP$  = neutralization potential and  $AP$  = acid-producing potential, all expressed in units of equivalent mass of  $\text{CaCO}_3$  per equivalent mass of material. An  $NNP$  values less than zero generates acidic leachates, whereas a positive value leads to alkaline leachates. Both  $NP$  and  $AP$  may be determined using the standardized procedure presented in the 1978 Report No. 600/2-78/054 from the United States Environmental Protection Agency (*EPA*) (Sobek et al. 1978). The procedure was initially developed to predict the potential for a material to produce acid mine drainage (*AMD*) at coal mines due to oxidation of pyrite. *ABA* may also be used to evaluate the relative level of weathering by oxidation between two originally similar geomaterials (Ardua et al. 2008, Essington 2004, Kargbo and He 2004, Sobek et al. 1972). Although a multitude of chemical indices describing geomaterial weathering exist, *ABA* characterization may be of particular interest due to its

simplicity, reliability, and the large amount of available *ABA* data for the area from which the *MWR* used in this study was obtained. Independent *ABA* testing was also performed as part of the testing program and results are presented and discussed in Chapters 4 and 5. While more extensive study could focus on intrinsic differences in mineralogy and weathering potentials between the unoxidized and oxidized *MWR*, the focus of this study is on differences in the mechanical response of these materials and *ABA* is used as an initial index for relative levels of *in situ* weathering by oxidation between the two materials by comparing the mechanical response of the two *MWR* types studied. Establishing the effects of weathering on the intrinsic mechanical properties may lay the groundwork for development of a more rigorous description of the relationship between general mechanical behavior and time-dependent weathering.

## CHAPTER 4: EXPERIMENTAL PROGRAM

A systematic experimental program was conducted to (1) characterize the mechanical behavior and (2) determine the intrinsic mechanical parameters for the two *MWR* materials tested in this study. This approach will allow us to gain insight into the extent to which *in situ* weathering may influence these intrinsic characteristics. Index properties, such as specific gravity ( $G_s$ ), particle size distribution, and limiting void ratios ( $e_{max}$  and  $e_{min}$ ), were determined in the exact same manner for the two *MWR* materials. This chapter describes the properties measured and the experimental methods used to determine these properties for each *MWR* material studied.

### 4.1 Materials

Materials tested in this study are from the Ordovician Vinini formation in northern Eureka County, Nevada. The Ordovician classification describes the second of six geologic time periods in the Paleozoic era, which occurred between  $488.3 \pm 1.7$  and  $443.7 \pm 1.5$  million years ago. The Vinini formation is a sedimentary rock formation overlying the Deep Star sediment-hosted gold deposit in north-central Nevada. The Vinini formation is composed of black and gray siltstone and cherty mudstone with planar to wavy bands of 1 to 5-mm-thick alternating dark gray and black siltstone beds (Jory 1999, Albino 1993).

The two *MWR* materials tested in this study were blasted and removed from the floor of an open pit mine on the same day (March 15, 2010). On the day the materials were

removed from their natural condition, two shovels were removing materials from the Northern and Southern areas of the Northwest expansion of the open pit.

The oxidized material was removed from the Northern area (circle (a) in Figs.4.1 & 4.2) at an elevation of 1585 m above mean sea level (*MSL*), which corresponded to approximately 18.3 m below the original ground surface (before mining activities began). The unoxidized material was removed from the same elevation of 1585 m above *MSL*, however this location corresponded to a depth of approximately 24.4 m below the original ground surface (circle (b) in Figs. 4.1 & 4.2).



Figure 4.1 Overhead view of open pit from which the (a) oxidized and (b) unoxidized *MWR* materials were removed.

Figure 4.2 displays a photograph of the open pit on the day of removal with the two shovels working in the approximate area where the materials used in this study were obtained. The terminology used to distinguish between the field samples is “oxidized”

and “unoxidized” because natural hydrogeologic conditions led to one of the samples being more oxidized than the other. As discussed in detail in Section 2.4, oxidation of geomaterials may be the dominant process in the weathering of some minerals and sedimentary rocks (Ollier 1969). This weathering can occur *in situ* (typically in the form of an oxidation front) as well as after a *MWR* material is removed from the ground and used in the construction of embankment dams and waste rock piles.



Figure 4.2 Open pit on the day of removal showing the two shovels working in opposite sides of the pit.

## 4.2 Experimental Methods

### 4.2.1 Modeled Particle Size Distributions

A field sample of each material type was collected and the particle size distribution was determined by sieving the entire sample according to ASTM D 6913 Method B. These field samples contained particle sizes as large as 75 mm, which is larger than the maximum particle size of 25 mm that could be tested in the *LSTX* apparatus used in this study. As discussed in Section 2.2.3, parallel particle size distributions were created to contain maximum particle sizes equal to the maximum particle size that may be tested in the *LSTX* apparatus. Particle size distributions of the unoxidized and oxidized field samples, as well as the modeled parallel particle size distributions are presented in Figure 4.3. Particle size distributions of the test specimens were modeled to be identically parallel to the particle size distribution of the collected field sample for sieves up to the #200 (0.075 mm) sieve. For particle sizes smaller than 0.075 mm, a mass of material passing the #200 sieve was added to each triaxial specimen. The actual distribution of particle sizes smaller than 0.075 mm is unknown. However, these particle sizes comprise of 2 - 5 % of all triaxial specimens by dry mass. Photos of the unoxidized and oxidized *MWR* gradations tested in triaxial compression are shown in Figure 4.4.

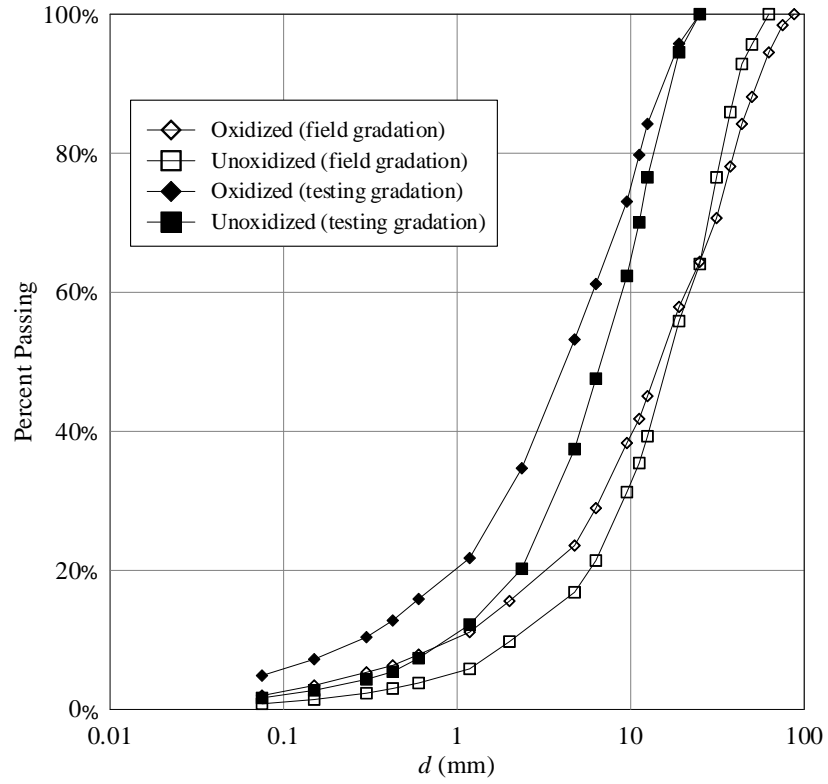


Figure 4.3 Particle size distributions for the unoxidized and oxidized field samples and the corresponding parallel particle size distributions containing particle sizes appropriate for the *LSTX* apparatus used in the study.

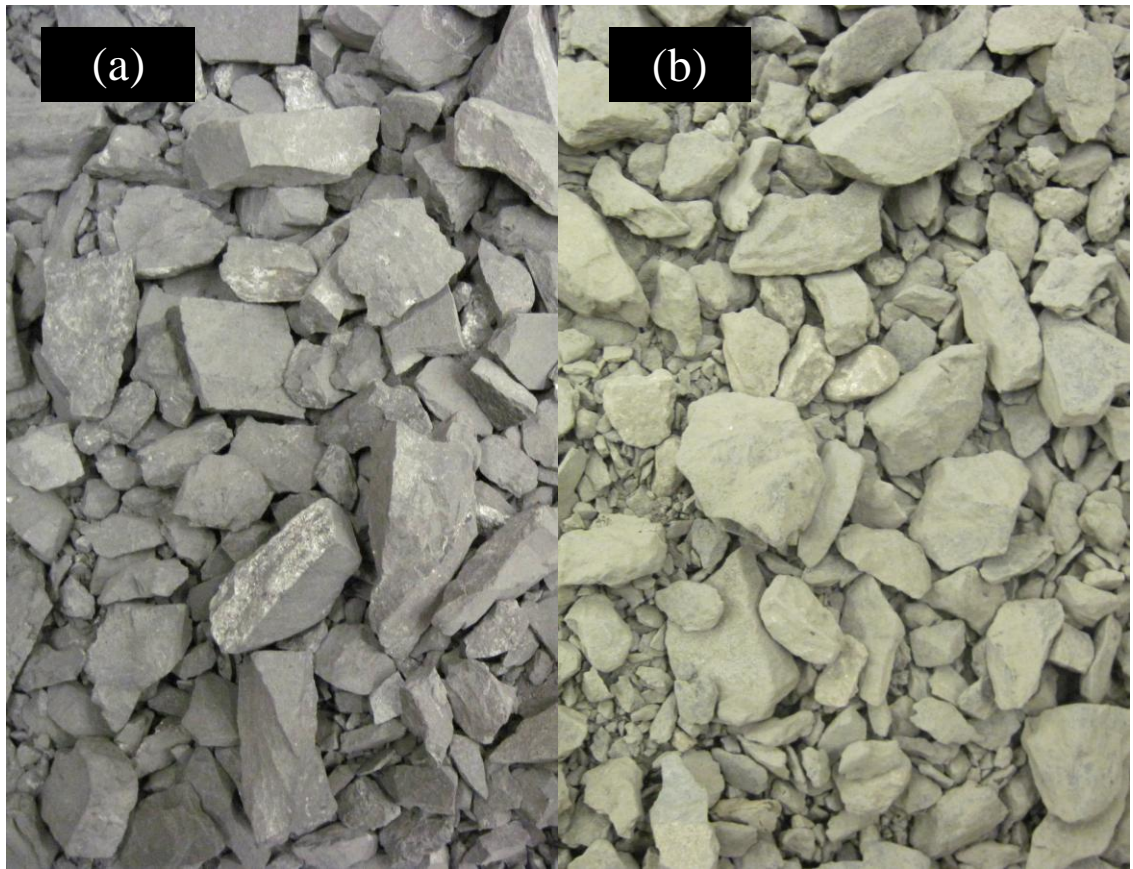


Figure 4.4 Photos of the (a) unoxidized and (b) oxidized *MWR* parallel gradation materials tested in this study.

Quantitative test results from ASTM D6913-04 Method B are presented in Table 4.1, along with the Unified Soil Classification System (USCS) classification for the two materials, where  $C_u$  = coefficient of uniformity,  $C_c$  = coefficient of curvature, and  $D_{50}$  = mean particle size.

#### 4.2.2 Maximum and Minimum Void Ratios

The maximum ( $e_{max}$ ) and minimum ( $e_{min}$ ) void ratios were determined according to ASTM D 4254-00 and ASTM D4253-00, respectively, for the particle size distributions of *MWR* tested in the *LSTX* apparatus. Results are presented in Table 4.1.

### 4.2.3 Specific Gravity

The specific gravity ( $G_s$ ) of each *MWR* sample was determined for materials passing the #4 (4.75-mm) sieve according to ASTM D 854-02. The specific gravity ( $G_s$ ) of each *MWR* sample was determined for materials retained on the #4 (4.75-mm) sieve according to ASTM C127-07. The value of  $G_s$  used to calculate *LSTX* test results was determined by a weighted average of the results from the two methods. This weighted average corresponded to the appropriate dry mass proportion of materials passing and retained on the #4 sieve for each specimen. Results are presented in Table 4.1.

Table 4.1 Index properties for modeled particle size distributions of unoxidized and oxidized Vinini formation *MWR* determined by standardized ASTM procedure.

	$C_u$	$C_c$	$D_{50}$ (mm)	USCS Classification (field gradation)	USCS Classification (triaxial specimen gradation)	$e_{max}$	$e_{min}$	$G_s$
Unoxidized Vinini	9.1	1.6	6.8	GW	GW	0.753	0.360	2.63
Oxidized Vinini	21.6	2.2	4.3	GW	SW	0.803	0.420	2.67

### 4.2.4 Modeled Particle Size Distributions

While parallel particle size distributions have been shown to be the preferred method of sample size reduction (Varadarajan et al. 2003, Sithram and Nimbkar 2000), the technique has been shown to lead to peak and critical state friction angles that are not necessarily identical between two parallel particle size distributions (Varadarajan et al. 2003, Sithram and Nimbkar 2000).

Both field samples of *MWR* classify as well graded gravel with sand (GW) according to ASTM D 2487-10. The particle size distributions modeled to fit the *LSTX* apparatus used in this study classify as well-graded sand with gravel (SW) for the oxidized specimen and well graded gravel with sand (GW) for the unoxidized specimen. The unoxidized and oxidized particle shapes were each observed to be angular according to ASTM D2488-09.

#### 4.2.5 Specimen Preparation and Uniformity

In an effort to (1) properly recreate the soil fabric from the field in the test specimens, and (2) create uniform (in terms of  $D_R$ ) and reproducible triaxial test specimens, a standardized procedure (ASTM D4253-00 Method B) was slightly modified to allow triaxial specimen preparation for a wide range of relative densities (i.e.  $23 < D_R < 96\%$ ). The ASTM D 4253-00 Method B is typically used to evaluate the minimum index density of granular soils in a 152.4-mm-diameter, 152.4-mm-tall cylindrical mold. To create the 152.4-mm-diameter, 304.8-mm-tall triaxial specimens tested in this study, *MWR* samples were split into two identical halves. The first lift was placed into a 152.4-mm-diameter vacuum split mold lined with a latex membrane in the same manner used in ASTM D4253-00 Method B (a.k.a. rapid tube withdrawal method). Then, the second lift was placed on top of the first lift using the same procedure. A third “dummy” lift was placed in the exact same manner on top of the second lift and then subsequently removed. This third “dummy” lift was used to reconstitute the second lift at a loose state that is identical to the state of the first (lowermost) lift. To create denser specimens, an 80-N surcharge

was applied to the top of each lift and vibration was applied in evenly timed increments to the top and sides of the split mold using a hand-held vibrator. Experimental evidence (Tables 4.2 & 4.3) is presented in terms of average values and the corresponding coefficients of variation (*COV*) giving an indication of the relative repeatability and uniformity of *LSTX* specimens. These results indicate that these two reconstitution methods described previously lead to either loose or dense specimens containing two lifts with very similar relative densities.

Table 4.2 Relative density of top and bottom lifts of a “dense” oxidized *LSTX* specimen using the proposed procedure. Initial values are before application of the dummy lift and final values are after application of the third “dummy” lift

<i>Trial</i>	Lift 1 (initial)	Lift 2	Lift 1 (final)	Average	Coefficient of Variation
	$D_R$	$D_R$	$D_R$	$D_R$	(%)
1	82%	90%	82%	86%	7%
2	82%	93%	82%	87%	9%
Average	82%	92%	82%		
Coefficient of Variation (%)	0%	2%	0%		

Table 4.3 Relative density of top and bottom lifts of a “loose” oxidized *LSTX* specimen using the proposed procedure. Initial values are before application of the dummy lift and final values are after application of the third “dummy” lift and vibration

	Lift 1 (initial)	Lift 2	Lift 1 (final)	Average	Coefficient of Variation
<i>Trial</i>	$D_R$	$D_R$	$D_R$	$D_R$	(%)
1	35%	38%	33%	36%	10%
2	29%	22%	29%	25%	18%
3	23%	32%	27%	29%	14%
4	13%	23%	18%	21%	19%
Average	25%	29%	27%		
Coefficient of Variation (%)	36%	26%	24%		

#### 4.2.6 Large-Scale Triaxial Testing

Eighteen triaxial tests were completed as a part of this study. Triaxial specimens were reconstituted to “loose”, “medium” and “dense” initial levels of  $D_R$  which were isotropically compressed to levels of  $p' = 100, 200, \text{ and } 400$  kPa before being sheared in drained axisymmetric compression. Test designations were assigned to systematically compare test results. These designations give: (1) the type of *MWR* material used (unoxidized or oxidized) (2) the level of  $D_R$  achieved after isotropic compression and (3) the level of  $p'$  at the end of isotropic compression. For example, an unoxidized specimen isotropically compressed to  $D_R = 57\%$  and  $p' = 100$  kPa will be referred to as U57-100.

The *LSTX* cell used in this study was manufactured by Research Engineering LLC, Grass Valley, CA and is capable of testing triaxial specimens with diameters equal to 152.4 mm (6 in). As prescribed by ASTM D4767-04, the ratio of specimen height to specimen diameter was equal to 2 for all specimens leading to a target initial specimen height of 304.8 mm. The cell water pressure and back pressure were each pressurized using manual air pressure regulators. These air pressure regulators apply pressure through panel board burettes which serve as an air-water interface between the cell/specimen pore water and the applied air pressure. The burettes were also calibrated to allow volume change measurements to be read manually for the cell pressure and back pressure lines during any test stage. The panel board was manufactured by Trautwein Soil Testing Equipment, Houston, TX, while the computer-controlled load frame used to apply axial loads to the specimen was manufactured by GCTS Inc., Tempe, AZ. Table 4.4 provides a summary of calibration data for specific testing instruments which make up the *LSTX* apparatus. All of

the equipment described above can also be seen in Figure 4.5 with a specimen set up in the cell.

Table 4.4 Summary of calibration data for instruments used as a part of the *LSTX* apparatus.

	Cell Pressure Transducer	Pore Pressure Transducer	Axial Load Cell	Axial Displacement Transducer	Volume Change Burettes
unit	kPa	kPa	kN	mm	mL
Calibration Factor (unit/V/V <sub>s</sub> )	69280.77	138420.44	26.5657	65.43796	N/A
Excitation Voltage (V <sub>e</sub> )	9.9593	9.9593	3.0000	10.0000	N/A
Accuracy (%)	0.073%	0.092%	0.59%	0.27%	0.37%
Resolution (unit)	0.499	0.628	0.29	0.07	0.5

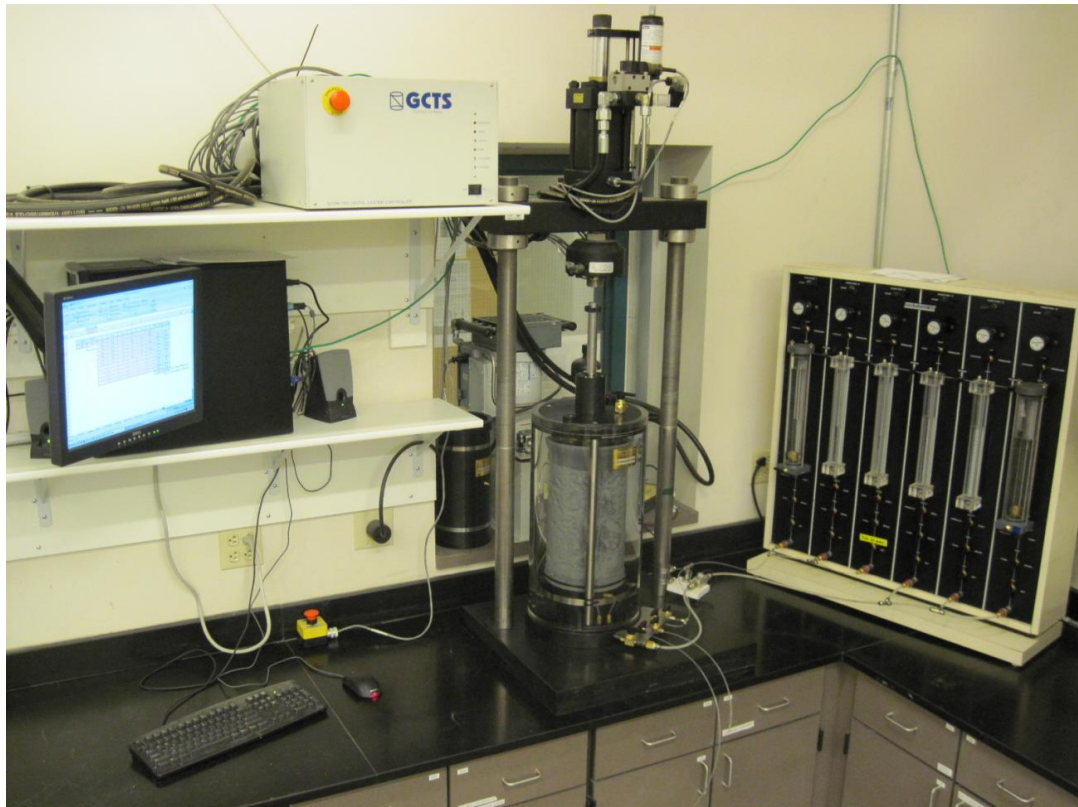


Figure 4.5 *LSTX* apparatus used in the study.

Procedures used during the testing program were based upon standardized ASTM testing procedures when a standardized procedure was available. In the absence of a standardized ASTM testing procedure, such as a procedure for isotropically consolidated drained (*CID*) triaxial testing, well-established techniques developed to test triaxial specimens containing clean sands were used (Head 1986).

#### 4.2.4.1 Flushing

After the triaxial specimens were reconstituted according to the procedure outlined in 4.2.3, the initially-dry specimens were flushed slowly (from the bottom to the top of the specimen) with fresh de-aired water. A hydraulic gradient less than 1.5 and an effective radial stress ( $\sigma_r'$ ) equal to 30 kPa was maintained during flushing for all specimens. A volume of water equal to 3-10 of the specimen pore volumes was flushed through the specimen until no additional entrapped air bubbles were observed to exit from the specimen with continued flushing.

#### 4.2.4.2 Back Pressure Saturation

After flushing the specimens with de-aired water, back pressure saturation was conducted manually according to the procedure outlined in Head (1986). Back pressure increments equal to 30 kPa and an initial  $p'$  equal to 30 kPa were used at this stage. Back pressure saturation was completed until a  $B$  value (Skempton 1954) greater than or equal to 0.98 was achieved. Final  $B$  values are reported for each triaxial test in Tables 5.1 & 5.2. Achieving this level of saturation required a back pressure level of 300-500 kPa depending upon the initial level of saturation at the end of flushing and the number of

pore volumes flushed (Head 1986). The axial strain ( $\varepsilon_a$ ) of each specimen was measured during both the flushing and back pressure saturation processes. This axial strain was used to estimate the level of volumetric strain ( $\varepsilon_p$ ) occurring during flushing and back pressure saturation. This approximation assumes that the principal strain ratio ( $R_s$ ) of the specimen during flushing and back pressure saturation is equal to the  $R_s$  measured subsequently on the saturated specimen during isotropic compression. The parameter  $R_s$  may be defined for axisymmetric conditions as:

$$R_s = \frac{\varepsilon_3}{\varepsilon_1} \quad (4.1)$$

where  $\varepsilon_3$  = minor principal strain and  $\varepsilon_1$  = major principal strain.

#### 4.2.4.3 Isotropic Compression

After back pressure saturation, *LSTX* specimens were subjected to incremental increases in isotropic  $p'$  equal to 30, 50, 100, 200, and 400 kPa. Final levels of isotropic  $p'$  equal to 100, 200, and 400 kPa were subsequently tested in drained axisymmetric compression. The volumetric strains ( $\varepsilon_p$ ) during the isotropic compression stage were manually recorded using a burette which was connected to the back-pressure line. Axial strains ( $\varepsilon_a$ ) were recorded throughout flushing, saturation, consolidation and shearing steps using an external LVDT (Linear variable differential transformer) which was securely connected to the axial actuator and piston rod.

#### 4.2.4.4 Creep in Granular Geomaterials

The development of additional  $\varepsilon_p$  after full dissipation of excess pore pressure during isotropic compression was noted during initial pilot tests. These values of  $\varepsilon_p$  varied from less than 0.1% to a maximum of 2.1%, with the value depending upon the initial  $D_R$ , final  $p'$  and material type. This creep behavior has been shown previously to be related to particle breakage on granular geomaterials (Lade and Karimpour 2010, Lade 1994). Although particle breakage was observed after isotropic and axisymmetric compression, no tests were terminated before the end of shearing ( $\varepsilon_a \approx 30\%$ ). Therefore, the potential development of particle breakage during isotropic compression and how it might relate to observed creep was not quantified. Regardless of the source of the creep behavior, it was considered to be an important step to allow volumetric changes during isotropic compression to stabilize to a rate of volumetric strain less than 0.05%/hour before the drained axisymmetric compression stage was initiated.

#### 4.2.4.5 Drained Axisymmetric Compression

In order to determine the intrinsic variables  $\phi_c$ ,  $Q$  and  $R$  associated with the critical state and dilatancy response of *MWR*, drained static monotonic axisymmetric compression tests were completed to levels of  $\varepsilon_a$  equal to or greater than 30%. Specimens were reconstituted over a wide range of relative densities ( $D_R$ ) and isotropically compressed to a wide range of  $p'$  in order to better characterize the mechanical response of the *MWR* materials.

All tests were conducted at this stage under strain-controlled conditions, with an axial strain rate equal to 0.13 %/min. This rate was conservatively determined using the approach outlined in Head (1986) in which volumetric strains or excess pore pressures are plotted against the logarithm or square root of time in minutes.

#### 4.2.4.5.1 Membrane Corrections for Triaxial Results

Triaxial test results were corrected for the effect of membrane restraint according to the detailed procedure outlined in LaRochelle et al. (1988). Due to the large particle sizes of the *MWR* materials tested, buckling of the membrane due to membrane penetration was observed during the isotropic compression stage of every test, thus the membrane imposed an increase in  $\sigma_r'$  as the specimen bulged during drained axisymmetric compression to peak deviator stress ( $q$ ). In tests which exhibited only bulging failure,  $\sigma_r'$  increased steadily throughout the test due to the hoop stresses induced in the membrane according to Eq. 4.2 (LaRochelle et al. 1988). In tests which experienced a combination of bulging and shear plane failure, correction for membrane restraint was made using Eq. 4.2 up to peak  $q$  and using Eq. 4.4 after peak  $q$  (LaRochelle et al. 1988):

$$\Delta\sigma_r' = 0.75 \frac{E\sqrt{\varepsilon_a}}{d_o} \quad (4.2)$$

where  $\Delta\sigma_r'$  = increase in radial effective stress due to membrane restraint,  $E$  = elastic modulus of the membrane (kN/m),  $\varepsilon_a$  = axial strain (%) and  $d_o$  = specimen diameter at the end of consolidation (m).

The value of  $E$  was estimated according to the procedure outlined in Head (1986) over a range of circumferential strains ranging from 0 to 20%. These strain levels corresponded to the range of circumferential strains experienced by the membrane in an actual test. A linear elastic modulus was also observed over these levels of strain. With this in mind, the value of  $E$  used in Eqs. 4.2-4.4 was held constant throughout each triaxial test.

The initial confining stress applied to the specimen when the membrane is stretched around the specimen ( $p_{om}$ ) was estimated according to Eq. 4.3 where  $d_{im}$  is the inner diameter of the membrane (LaRochelle et al. 1988).

$$p_{om} = 2E \frac{d_o - d_{im}}{d_o \cdot d_{im}} \quad (4.3)$$

Due to the dimensions of the membrane and specimen diameters at the end of isotropic compression, the value of  $p_{om}$  ranged from 0 to 2.5 kPa, with the value depending on the material type, final level of isotropic  $p'$ , and the initial  $D_R$ . As described by LaRochelle et al. 1988, the effect of  $p_{om}$  is significant in tests at low confining pressures on soft soils and becomes insignificant at magnitudes less than 1 kPa (LaRochelle et al. 1988).

According to the LaRochelle et al. (1988) framework, the formation of a shear plane (typically observed after peak  $q$ ) impacts the appropriate membrane corrections to be made after peak  $q$  is mobilized. In tests which exhibit a combination of bulging and shear plane failure, the effect of membrane restraint was taken into account by correcting  $\sigma_r'$  up to peak deviator stress  $q = \sigma_a' - \sigma_r'$  in the exact same manner as in the case of pure bulging. This assumes that membrane penetration prevented the membrane from

supporting any axial load during the shearing stage. After peak  $q$  the effect of the membrane on the actual stress state of the specimen was taken into account by correcting the value of  $q$  due to straining of the membrane along the direction of the shear plane (as opposed to correcting  $\sigma_r'$  throughout the test in the case of only bulging) according to Eq. 4.4:

$$\Delta(\sigma_a - \sigma_r)A_c = 1.5 \cdot \pi \cdot d_o \sqrt{E \cdot f \cdot d_o \cdot \delta_e} \quad (4.4)$$

where  $f$  = unit friction between the membrane and dummy tested by La Rochelle et al. (1988) (kPa), and  $\delta_e$  = axial strain due to movement along the shear plane (%).

The elastic modulus of each membrane was determined for the two membranes used in triaxial testing according to the procedure outlined in Head (1986). Average results are summarized in Table 4.5 and a complete set of data is presented in Appendix D. The small membrane was a relatively thin (0.6-mm-thick) membrane which was used to facilitate specimen reconstitution. The second was a 5-mm-thick membrane which was shown during initial pilot testing to be necessary to prevent membrane puncture due to membrane penetration.

Table 4.5 Elastic modulus of each membrane used during triaxial testing.

	Small Membrane	Large Membrane
thickness (mm)	0.6	5.0
$E$ (kN/m)	0.6	6.9
$E$ (kPa)	950	1387

#### 4.2.4.5.2 Area Corrections for Triaxial Results

Correcting for changes in the cross sectional area of the triaxial specimen was completed according to the framework outlined in LaRochelle et al. (1988). In tests which exhibited

pure bulging failure, the corrected cross sectional area was calculated according to Eq. 4.5 which assumes that the specimen deforms as a right cylinder:

$$A_c = A_o \left( \frac{1 - \varepsilon_p}{1 - \varepsilon_a} \right) \quad (4.5)$$

where  $A_o$  = cross sectional area of the specimen after isotropic compression,  $\varepsilon_p$  = volumetric strain during axisymmetric compression,  $\varepsilon_a$  = axial strain during axisymmetric compression, and  $A_c$  = cross sectional area corrected for deformation of the specimen.

According to the LaRoche et al. (1988) framework, the formation of a shear plane (typically observed after peak  $q$ ) impacts the appropriate area corrections to be made to the cross sectional area after peak  $q$ . The cross sectional area may be calculated up to peak  $q$  using Eq. 4.5 and after peak  $q$  according to Eq. 4.6:

$$A_c = A_f + (A_{ce} - A_f) \left( \frac{\varepsilon_{ai} - \varepsilon_{af}}{\varepsilon_{ae} - \varepsilon_{af}} \right) \quad (4.6)$$

where  $A_c$  = corrected cross sectional area,  $A_f$  = cross sectional area at peak strength determined from Eq. 4.5,  $\varepsilon_{af}$  = axial strain at peak strength,  $\varepsilon_{ae}$  = axial strain at the end of the test,  $\varepsilon_{ai}$  = axial strain between peak  $q$  and the end of the test, and  $A_{ce}$  = the cross sectional area of the specimen at the end of the test.  $A_{ce}$  may be calculated using Eq. 4.7:

$$A_{ce} = \frac{\pi}{4} d_a d_b \quad (4.7)$$

where  $d_a$  and  $d_b$  are perpendicular cross sectional specimen diameters at the end of the test, which are perpendicular and parallel to the motion of the horizontal projection of the shear plane, respectively. Four of the eighteen triaxial tests presented in this study (U76-100, U83-200, U59-100 and O105-400) were observed to fail along a well-defined shear

plane (See Tables 5.1 and 5.2). For these tests  $d_a$  and  $d_b$  were estimated from photographs taken during each test at the highest levels of  $\varepsilon_a$  from three locations surrounding the specimen. In tests with visible shear plane failures, the specimen was observed to come into contact with the triaxial cell wall at the highest levels of  $\varepsilon_a$ . Knowledge of the inner diameter of the triaxial cell wall allowed for a second estimate of the specimen diameter at the end of the test. Since actual measurements were not able to be carried out on these specimens at the end of the tests, large-strain responses are shown in dashed lines in Figures 5.4 and 5.6 and should be used for general illustration purposes only.

While the La Rochelle et al. (1988) framework is one of the most comprehensive and thorough approaches to correcting triaxial test results, the formation of shear bands is an extremely complex interaction which is idealized by observing the behavior of dummy specimens. In the presence of pure bulging (typically observed in tests reconstituted to the loosest levels of  $D_R$  and compressed to the highest levels of  $p'$ ), test corrections are easier to carry out. With this in mind, the actual critical state friction angle ( $\phi_c$ ) reported for each *MWR* material was systematically evaluated by excluding tests that contained shear bands. Thus,  $\phi_c$  was preferentially evaluated in the unoxidized and oxidized *MWR* materials by considering tests U48-400 and O87-400, respectively. These results give the same values of  $\phi_c$  as if  $\phi_c$  were determined from the *CSL* in  $p'-q$  space, which includes all tests exhibiting bulging failure. However, the individual results obtained for each test are still presented in Tables 5.1 and 5.2.

#### 4.2.7 Particle Strength

It is widely accepted that compressive fracture of a single soil particle results from a tensile failure (McDowell and Bolton 1998). The tensile strength of individual soil particles is one of the numerous microscopic influences on the macroscopic mechanical behavior of geomaterials observed in a triaxial apparatus (Lee 1992, Billam 1972). While a number of methodologies exist regarding the proper measurement of the tensile strength of soil particles, the tensile stresses induced in a particle of diameter  $d$  loaded concentrically between two points are typically represented by  $\sigma = P/d^2$  where  $P$  is the concentrically applied load and  $\sigma$  is the tensile stress induced within the particle. Broch and Franklin (1972) presented the point-load strength test as an index test rock strength classification which eventually became an ASTM standard test method. In this study, point load strength index values ( $I_{s(50)}$ ) were determined for the larger (30-75 mm) particles of unoxidized and oxidized *MWR* according to ASTM D 5731 “Determination of the Point Load Strength Index of Rock and Application to Rock Strength Applications”. Due to the sedimentary nature of the *MWR*, planes of weakness were identified as being parallel to the bedding planes noted by Jory (1999) and Albino (1993). With this in mind,  $I_{s(50)}$  was determined perpendicular and parallel to the planes of weakness in order to determine the point load anisotropy index  $I_{a(50)}$  for each *MWR* type. ASTM D 5731 also presents a classification system for typical  $I_{s(50)}$  values which contains four categories: Extremely High, Very High, High, Medium, Low, Very Low, and Extremely Low. Point load strength index is a simple, standardized method for characterizing the tensile strength of rocks and has been implemented in other studies

involving particle breakage in triaxial testing (Indraratna et al. 1998, Indraratna et al. 1993, Lee 1992, Billam 1972).

#### 4.2.8 Particle Breakage and Fractal Dimension

Determining the fractal dimension  $D$  of a distribution of particles requires knowledge of the specific gravity, total mass and “relative distribution of mass between a characteristic particle dimension” (Turcotte 1986) which is commonly determined through a particle size distributions (McDowell and Bolton 1998, Lee 1992, Hardin 1985). Analysis of particle size distributions before and after application of any state of stress to a crushable soil allows for the evolution of the fractal dimension to be evaluated. The total amount of particle breakage due to the combined effect of isotropic and drained axisymmetric compression was determined in this study by measuring the particle-size distributions at the end of each triaxial test according to ASTM D 6913-04 Method B. The initial particle size distributions, which were modeled to be identical and parallel to the field gradation, had a constant initial fractal dimension for each *MWR* type (Oxidized = 2.79, Unoxidized = 2.53) before testing. If a constant fractal dimension is achieved during testing, the modified work equation (Eq. 3.20) may be evaluated for the two *MWR* materials (Tarantino and Hyde 2005).

#### 4.2.9 Acid-base Accounting

Although a multitude of chemical indices describing geomaterial weathering exist, *ABA* characterization may be of particular interest due to its simplicity, reliability, and the large amount of available *ABA* data for the area from which the *MWR* used in this study

was obtained. *ABA* testing was conducted by ACZ Laboratories Inc., Steamboat Springs, CO as part of the testing program according to the standardized United States Environmental Protection Agency (*EPA*) methodology (Sobek et al. 1972) and results are presented Chapter 5. *ABA* considers net neutralization potential (*NNP*) or neutralization potential ratio (*NPR*):

$$NNP = NP - AP \quad (4.8)$$

and

$$NPR = NP/AP \quad (4.9)$$

where *NP* = neutralization potential and *AP* = acid-producing potential, all expressed in units of equivalent mass of  $\text{CaCO}_3$  per equivalent mass of material. An *NNP* values less than zero generates acidic leachates, whereas a positive values leads to alkaline leachates.

## CHAPTER 5: RESULTS

### 5.1 Isotropic Compression

After back pressure saturation, specimens were isotropically compressed to  $p'$  equal to 100, 200, or 400 kPa. All tests follow the same isotropic compression steps with  $p' = 30, 50, 100, 200,$  and  $400$  kPa. Results of isotropic compression are presented for the unoxidized and oxidized *MWR* specimens in specific volume  $v$  versus the natural logarithm of  $p'$  space in Figures 5.1 and 5.2, respectively.

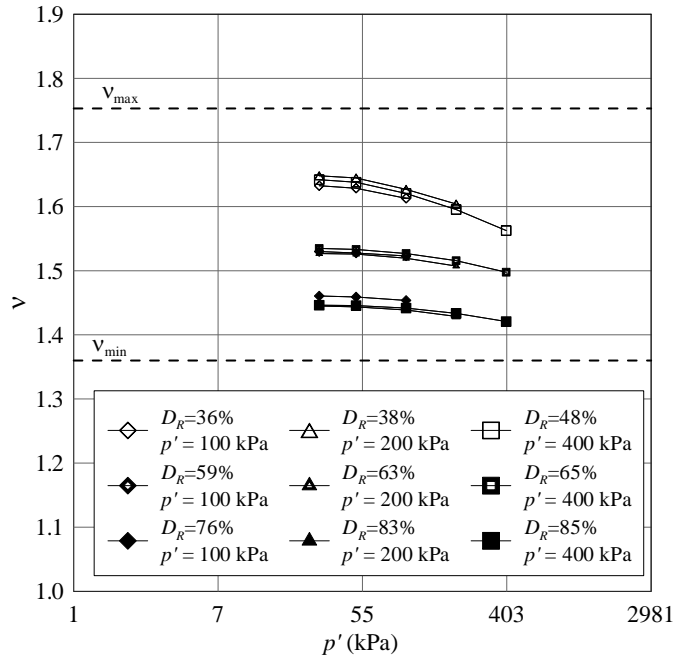


Figure 5.1 Isotropic compression data for unoxidized specimens. Values of  $p'$  and  $D_R$  represent the final specimen state at the end of isotropic compression, before shearing.

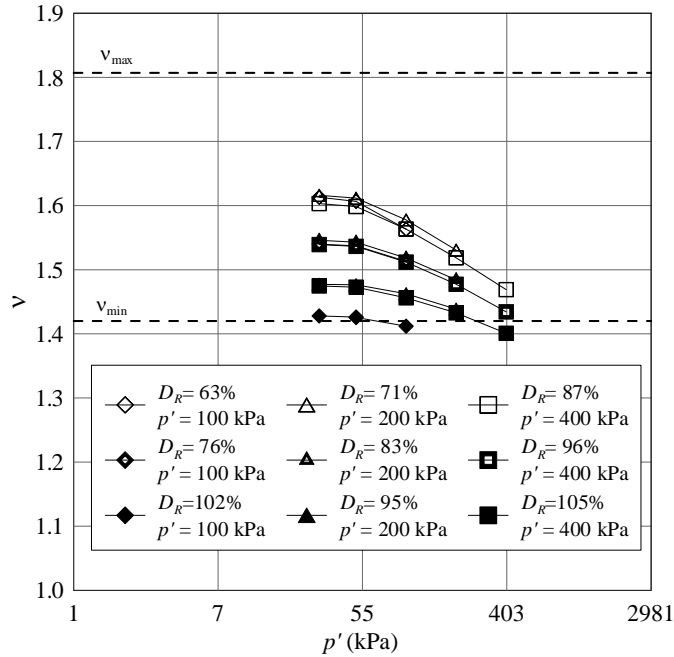


Figure 5.2 Isotropic compression data for oxidized specimens. Values of  $p'$  and  $D_R$  represent the final specimen state at the end of isotropic compression, before shearing.

As mentioned in Chapter 4, due to the lack of radial deformation transducers, specimen volume changes during flushing, back pressure saturation were estimated by assuming that the principal strain ratio ( $R_s$ ) ratio is constant for a given material during flushing, back pressure saturation, and isotropic compression. The  $R_s$  of each material was determined using a linear best fit regression which included isotropic compression data for every test. This data and the lines of best fit are presented in Figure. 5.3.

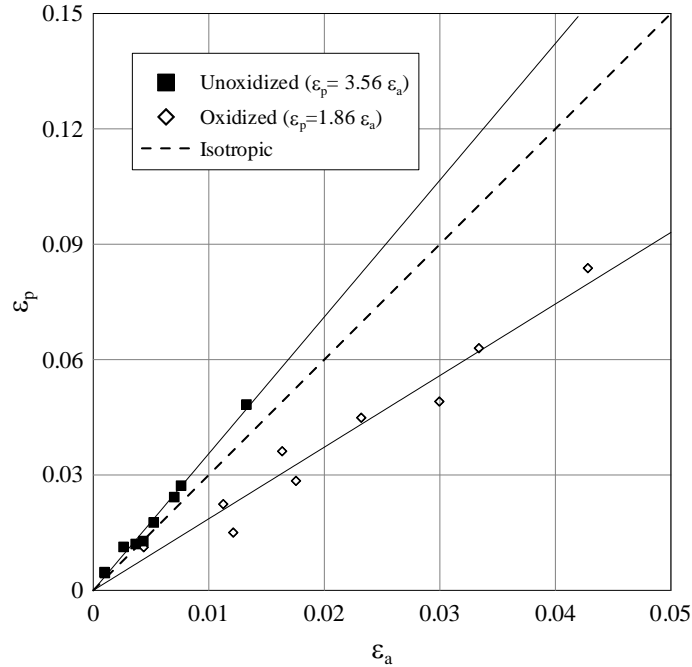


Figure 5.3 Axial strain  $\epsilon_a$  vs. volumetric strain  $\epsilon_p$  at the final isotropic level of  $p'$  for unoxidized and oxidized specimens with a line of best fit (used to estimate the principal strain ratio for each material). An isotropic line is also included to give an indication of the level of anisotropic response during an isotropic state of stress increment.

## 5.2 Drained Monotonic Loading

Drained axisymmetric compression tests were carried out on isotropically compressed specimens over a wide range of combinations of  $p'$  and  $D_R$  in order to describe a wide range of mechanical response. Specimens were subjected to drained loading up to an axial strain  $\epsilon_a$  of approximately 30%. The displacement rate was held at 0.4 mm per minute for all tests, which corresponded to an axial strain rate equal to 0.13 – 0.14%/minute, with the actual value depending upon the final consolidated height of the specimen which was similar but not constant for all specimens. This displacement rate was conservatively determined from the procedure outlined in Head (1986).

Plots of the variation of the deviatoric stress invariant  $q$  versus  $\varepsilon_a$  are presented for the unoxidized and oxidized specimens in Figures 5.4 and 5.6, respectively. Dashed lines shown after peak deviator stress indicate the formation of a shear band during the test. As mentioned previously, the formation of a shear band leads to uncertainties in the membrane and area corrections to be made. With this in mind, tests which exhibited shear bands have dashed lines to indicate the uncertainty of the results after peak deviator stress. Plots of volumetric strain  $\varepsilon_p$  versus  $\varepsilon_a$  are presented for the unoxidized and oxidized specimens in Figures 5.5 and 5.7, respectively. Critical state was defined for all tests as the final data point at maximum axial strain, which corresponds to the best estimates that could be made of the critical state conditions of the specimens for each test as they approach a state of constant stress (in terms of  $p'$  and  $q$ ) and specific volume  $v$  and with continued axial deformation.

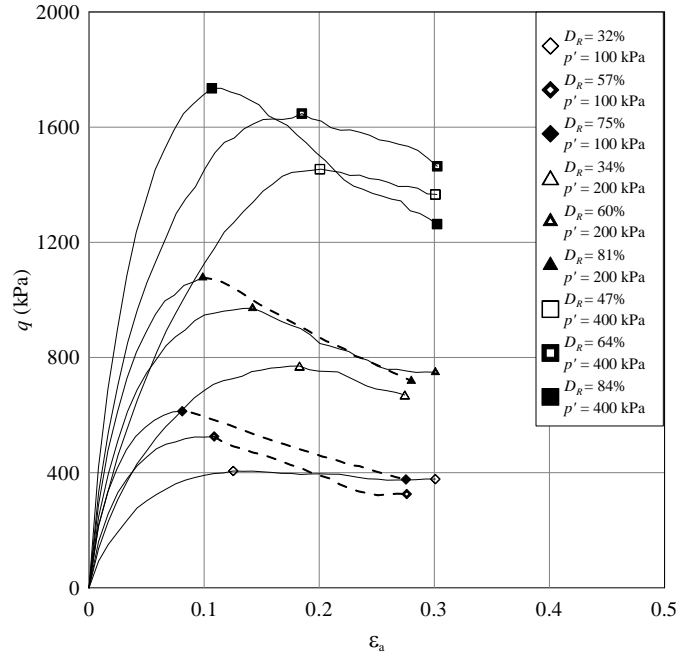


Figure 5.4 Deviatoric stress versus axial strain for unoxidized specimens. Values of  $p'$  and  $D_R$  represent the final specimen state at the end of isotropic compression, before shearing.

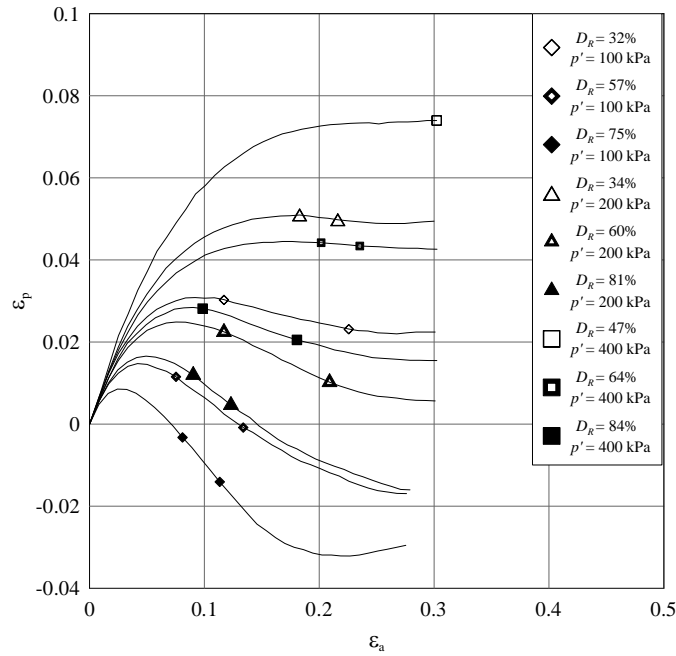


Figure 5.5 Volumetric strain versus axial strain for unoxidized specimens. Values of  $p'$  and  $D_R$  represent the final specimen state at the end of isotropic compression, before shearing.

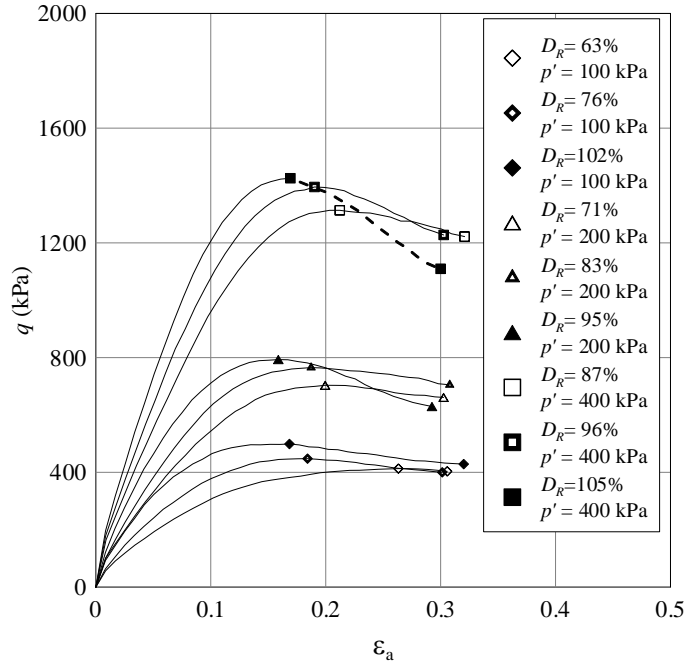


Figure 5.6 Deviatoric stress versus axial strain for oxidized specimens. Values of  $p'$  and  $D_R$  represent the final specimen state at the end of isotropic compression, before shearing.

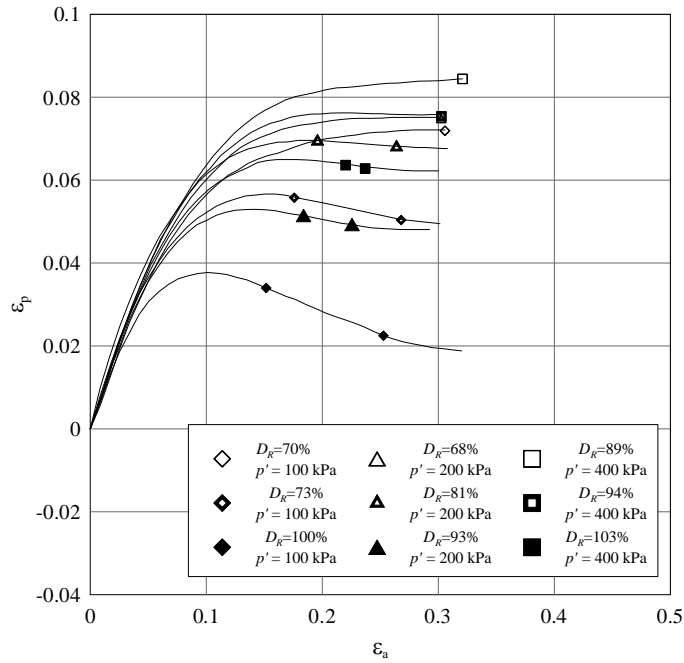


Figure 5.7 Volumetric strain versus axial strain for oxidized specimens. Values of  $p'$  and  $D_R$  represent the final specimen state at the end of isotropic compression, before shearing.

Test results are presented in  $\ln(p')$  versus  $v$  space during compression and shearing for unoxidized and oxidized specimens in Figures 5.8 and 5.9, respectively.

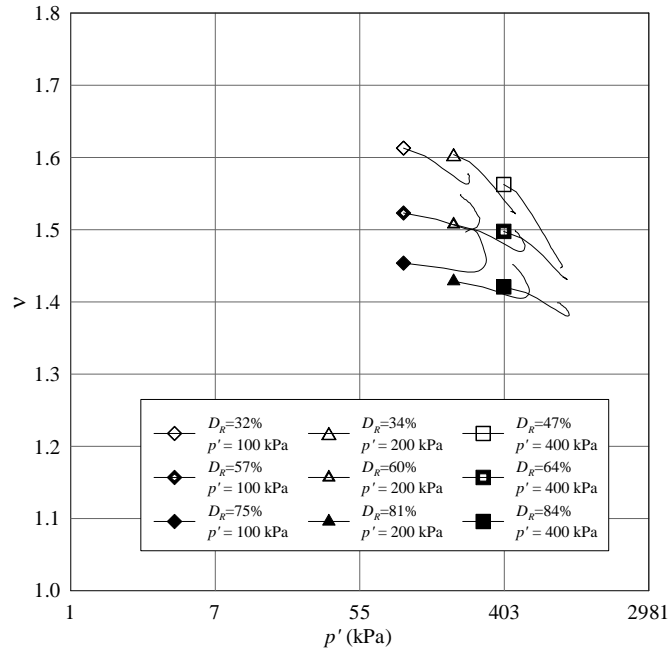


Figure 5.8 Unoxidized specimens in  $\ln(p')$  –  $v$  space during axisymmetric compression.

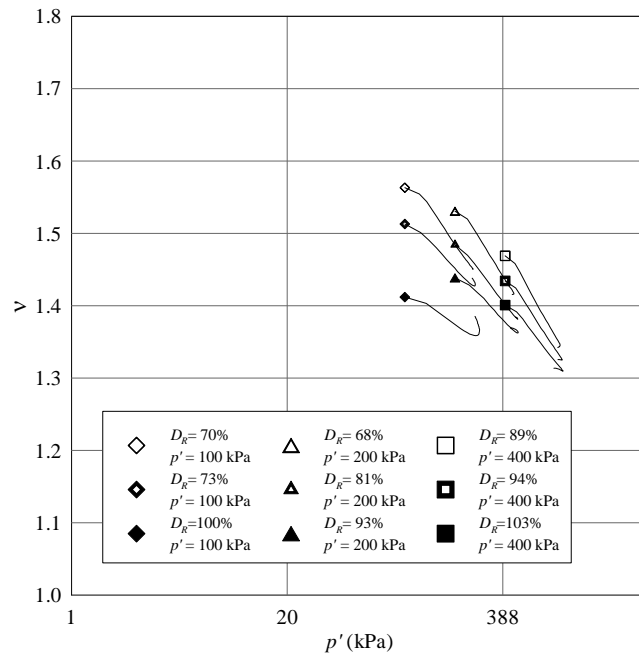


Figure 5.9 Oxidized specimens in  $\ln(p')$  –  $v$  space during axisymmetric compression.

Effective stress paths are presented in terms of the stress invariants  $p'$  and  $q$  for the unoxidized and oxidized specimens in Figures 5.10 and 5.11, respectively.

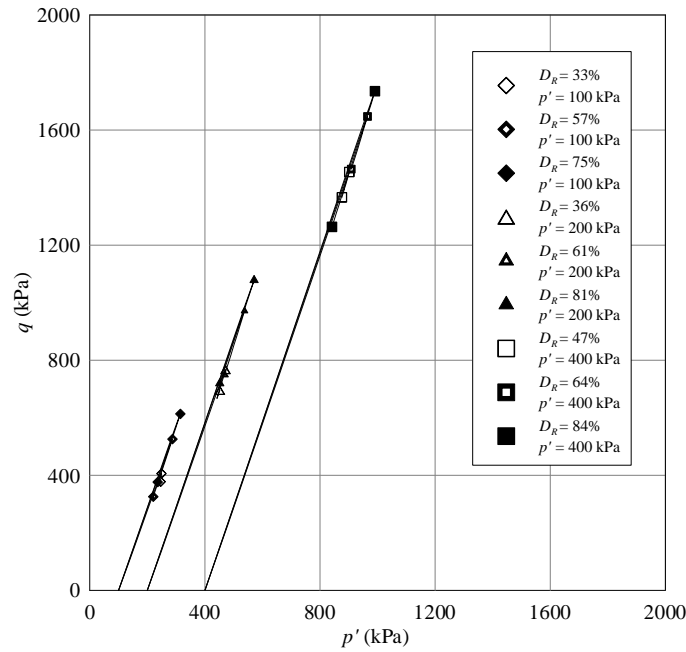


Figure 5.10 Effective stress paths for unoxidized specimens. Values of  $p'$  and  $D_R$  represent the final specimen state at the end of isotropic compression, before shearing. The two data points for each test correspond to peak and critical state stress states.

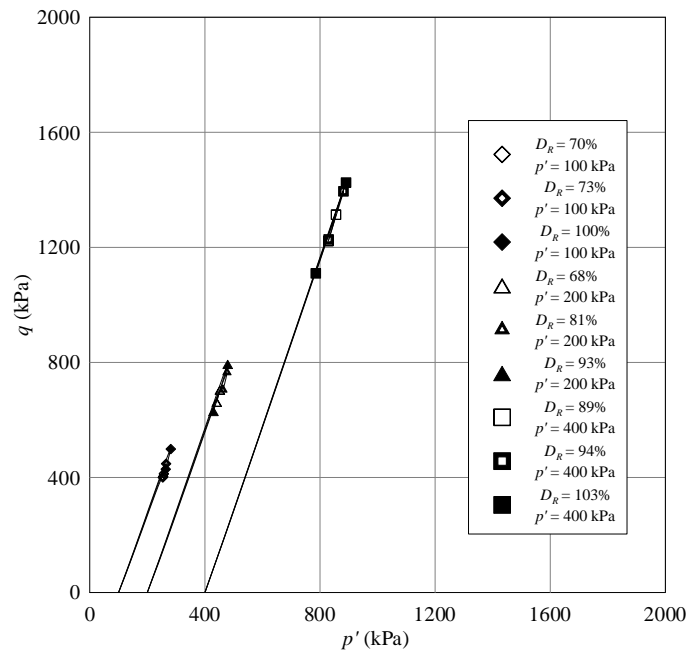


Figure 5.11 Effective stress paths for oxidized specimens. Values of  $p'$  and  $D_R$  represent the final specimen state at the end of compression, before shearing. The two data points for each test correspond to peak and critical state stress states.

Results are presented in Tables 5.1 and 5.2 for the peak and critical state friction angles ( $\phi_p$  and  $\phi_c$ ) mobilized in each individual test alongside their corresponding state (in terms of  $p'$  and  $D_R$ ) after specimen setup, after flushing and back pressure saturation, and at the start of axisymmetric compression. All critical state values for  $p'$ ,  $q$  and  $v$  were defined in Tables 5.1 and 5.2 at the point of maximum shear strain mobilized in the tests and are referred to as  $p'_{cs}$ ,  $q_{cs}$  and  $v_{cs}$ . In Tables 5.1 and 5.2,  $D_{R, Initial}$  = initial  $D_R$  as reconstituted,  $D_{R, Flush \& BP}$  =  $D_R$  after flushing and backpressure saturation,  $D_{R, AC}$  =  $D_R$  after isotropic compression,  $(-\delta\varepsilon_p / \delta\varepsilon_a)_{max}$  = maximum dilatancy rate observed in the test.

Table 5.1 Results for the triaxial tests completed on unoxidized MWR

Test	$p'$ (kPa)	$D_{R, Initial}$	$D_{R, Flush \& BP}$	$D_{R, AC}$	$\phi_p$	$\phi_c$	$v_{cs}$	$p'_{cs}$ (kPa)	$q_{cs}$ (kPa)	$(\delta\varepsilon_p / \delta\varepsilon_a)_{max}$	$B$
U36-100	100	30%	31%	36%	40	38	1.58	246	378	0.067	0.99
U59-100	100	57%	57%	59%	44	36	1.55	221	326	0.212	0.99
U76-100	100	74%	74%	76%	47	39	1.50	236	376	0.336	0.99
U38-200	200	52%	27%	38%	40	38	1.52	452	695	0.035	0.99
U63-200	200	57%	58%	63%	44	39	1.50	470	749	0.136	0.98
U83-200	200	77%	77%	83%	46	39	1.46	452	719	0.221	0.99
U48-400	400	28%	28%	48%	39	38	1.45	876	1366	0.000	0.99
U65-400	400	56%	56%	65%	42	39	1.43	908	1464	0.023	0.99
U85-400	400	77%	78%	85%	43	37	1.40	842	1264	0.099	0.98

Table 5.2 Results for the triaxial tests completed on oxidized *MWR*

Test	$p'$ (kPa)	$D_{R, Initial}$	$D_{R, Flush \& BP}$	$D_{R, AC}$	$\phi_p$	$\phi_c$	$\nu_{cs}$	$p'_{cs}$ (kPa)	$q_{cs}$ (kPa)	$(\delta\varepsilon_p / \delta\varepsilon_a)_{max}$	$B$
O63-100	100	42%	50%	63%	39	39	1.45	255	403	0.000	0.98
O76-100	100	66%	69%	76%	41	39	1.44	254	400	0.059	0.99
O102-100	100	98%	98%	102%	42	38	1.39	264	429	0.113	0.99
O726-200	200	41%	49%	71%	38	37	1.42	441	661	0.000	0.98
O83-200	200	69%	69%	83%	40	38	1.38	463	705	0.021	0.98
O95-200	200	85%	85%	95%	40	36	1.37	430	629	0.057	0.99
O87-400	400	44%	53%	87%	38	36	1.34	829	1222	0.000	0.98
O96-400	400	65%	69%	96%	39	36	1.33	830	1228	0.000	0.99
O105-400	400	85%	86%	105%	39	35	1.31	785	1110	0.047	0.99

### 5.3 Particle Strength

Point load strengths of the unoxidized and oxidized *MWR* were determined using rock pieces retained on the 75 mm (1.5 in) sieve according to ASTM D5731-08 (Table 5.3). Due to the sedimentary nature of the *MWR*, planes of weakness were identified as being parallel to the bedding planes noted by Jory (1999) and Albino (1993). With this in mind,  $I_{s(50)}$  was determined perpendicular and parallel to the planes of weakness in order to determine the point load anisotropy index  $I_{a(50)}$  for each *MWR* type.

Table 5.3 Point load strength values of unoxidized and oxidized *MWR* determined according to ASTM D 5731-08

	$I_{s(50)}$ (MPa)	$I_{a(50)}$
Oxidized	1.02	1.43
Unoxidized	10.24	1.36

### 5.4 Particle Breakage

Particle breakage was quantified in this study by performing a particle size distribution analysis on each specimen after testing according to ASTM D 6913-04 Method B.

Results are presented in Figure 5.12 for an unoxidized and oxidized specimen which were isotropically compressed to the same state in terms of  $p'$  and  $D_R$  before drained axisymmetric compression. Results for all particle size distributions before and after testing are presented in Appendix B.

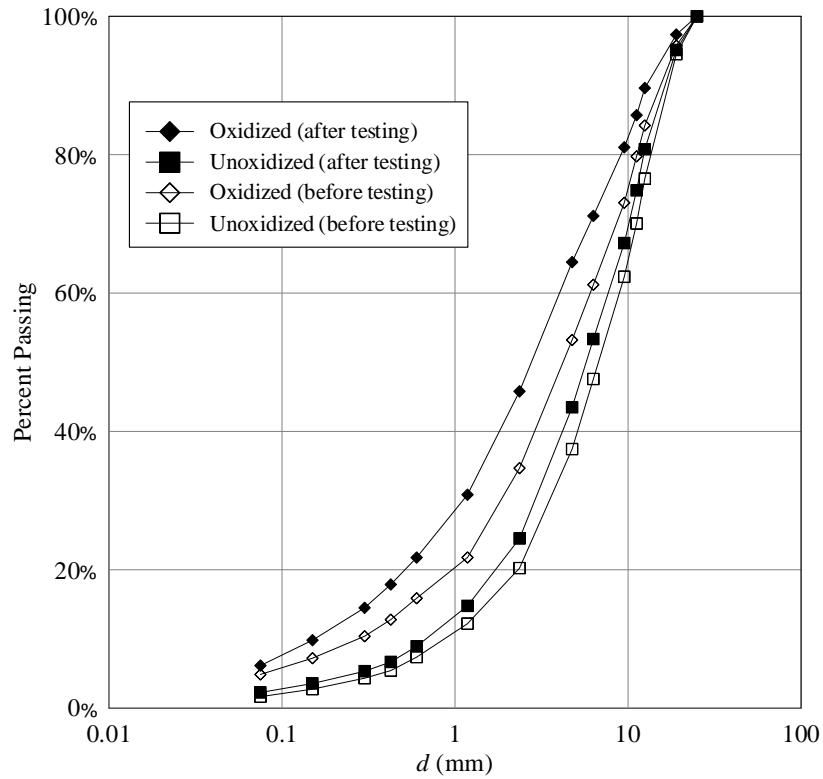


Figure 5.12 Changes in particle size distributions of unoxidized and oxidized specimens due to the combined effect of isotropic and axisymmetric compression. These two specimens were isotropically compressed to identical levels of  $D_R = 83\%$  and  $p' = 200$  kPa before drained axisymmetric compression.

### 5.5 Fractal Dimension

The fractal dimension  $D$  was determined for each sample after testing. The initial  $D$  for all unoxidized specimens was equal to 2.53 and the initial fractal dimension of all oxidized specimens was 2.79. Tables 5.4 and 5.5 demonstrate the evolution of  $D$  after testing at various levels of  $D_R$  and  $p'$  where  $D_f$  = final fractal dimension and  $\Delta D$  = the

change in the fractal dimension due to the combined effects of isotropic and axisymmetric compression. Appendix C presents plots used to determine  $D$  for each test.

Table 5.4 Values of  $D$  for unoxidized specimens after testing.

Test	$D$	$\Delta D$
U36-100	2.56	0.04
U59-100	2.57	0.04
U76-100	2.58	0.05
U38-200	2.59	0.07
U63-200	2.60	0.08
U83-200	2.60	0.07
U48-400	2.64	0.12
U65-400	2.64	0.12
U85-400	2.63	0.11

Table 5.5 Values of  $D$  for oxidized specimens after testing.

Test	$D$	$\Delta D$
O63-100	2.91	0.11
O76-100	2.91	0.11
O102-100	2.91	0.12
O72-200	2.95	0.16
O83-200	2.95	0.15
O95-200	2.94	0.15
O87-400	2.98	0.19
O96-400	2.99	0.20
O105-400	3.00	0.20

### 5.6 Acid Base Accounting

The neutralizing potential ( $NP$ ) and acid producing potential ( $AP$ ) values were determined according to the standardized EPA methodology (Sobek et al. 1972) (Table 5.6). These values are typically reported in units of mass of  $\text{CaCO}_3$  per 1000 equivalent units of mass of material. In other words, a sample with an  $NP = 12$  will contain 12 equivalent kilograms of  $\text{CaCO}_3$  per 1000 kilograms of material. Results (Table 5.6) are

quantified in terms of the net neutralization potential (*NNP*), Neutralization Potential Ratio (*NPR*) and Neutralization Potential (*NP*).

Table 5.6 Acid-base accounting results.

	Oxidized	Unoxidized
<i>AP</i> (kg CaCO <sub>3</sub> /Mg)	36	40
<i>NP</i> (kg CaCO <sub>3</sub> /Mg)	12	329
<i>NNP</i> (kg CaCO <sub>3</sub> /Mg)	-24	289
<i>NPR</i>	0.33	8.23

## CHAPTER 6: ANALYSIS OF RESULTS

While the geologic origin and specimen particle size distributions of the unoxidized and oxidized *MWR* tested in this study were shown to be similar (Fig. 5.12), the mechanical response of the two materials has a number of interesting differences. This chapter will discuss some of the differences in the intrinsic mechanical parameters of the unoxidized and oxidized *MWR* tested in triaxial compression as a part of this systematic study.

### 6.1 Specimen Preparation and Uniformity

Results presented in Tables 4.2 and 4.3 show relatively uniform and repeatable large scale triaxial (*LSTX*) specimens in terms of relative density ( $D_R$ ) for the two half-specimen lifts. The greatest lack of uniformity was shown to exist in the “loose” specimens. For these specimens, the largest average coefficient of variation between two lifts was equal to 19% considering four trials reconstituting specimens with initial  $D_R \approx 30\%$  (Table 4.2). The “dense” specimens were shown to be much more uniform and repeatable (Table 4.3) in terms of the  $D_R$  of two half-specimen lifts. Also noted in Tables 4.2 and 4.3, the final  $D_R$  of the top lift seems to be systematically higher than the final  $D_R$  of the bottom lift. This observed difference is thought to be due to the use of a flat platen on the top of each lift to assess the height (and corresponding  $D_R$ ) of each lift within the vacuum split mold. The large 25-mm particle sizes tested lead to large void spaces on the top of a given lift. When the height of the bottom lift is measured using a flat platen, these void spaces are calculated to be a part of the volume of the bottom lift. Placement

of the top lift on top of the bottom lift leads to some soil particles which are calculated to be a part of the top lift filling in the void spaces at the top of the bottom lift. When the final height of the top lift is measured, the actual soil mass within the measured volume is less than would be calculated using the entire half-specimen mass. This leads to a value of  $D_R$  which is calculated to be higher than the actual  $D_R$  of the top lift. Similarly, the actual  $D_R$  of the bottom lift is slightly higher than the values calculated in Tables 4.2 and 4.3. With these experimental limitations in mind, the specimen preparation technique was shown to create levels of specimen uniformity which were sufficient for axisymmetric element testing.

## 6.2 Isotropic Compression

Isotropic compression data for all unoxidized and oxidized specimens are presented in Figures 5.1 and 5.2, respectively. In this systematic study, the mechanical response of two *MWR* types was evaluated in axisymmetric compression at a  $p' = 100, 200, \text{ and } 400$  kPa over a wide range of target  $D_R$  which were considered to be “loose” ( $25\% < D_R < 40\%$ ), “medium” ( $50\% < D_R < 70\%$ ), and “dense” ( $75\% < D_R < 100\%$ ). These levels of  $p'$  were not sufficiently high to establish a unique normal compression line (NCL) for the two *MWR* materials. Therefore, specimens are observed to follow an unloading-reloading line (*URL*) in  $\ln(p') - v$  space during isotropic compression which is dependent upon the specimens initial  $D_R$  (McDowell et al. 2002, Been and Jefferies 2000, Muir-Wood 1990). The slope and intercept at  $p' = 1$  kPa of the *URL* may be determined using Eq. 3.7. The values for  $\kappa$  and  $v_\kappa$  are each observed to decrease with increasing initial  $D_R$  for each

*MWR* type. The values of  $\kappa$  and  $v_{\kappa}$  are systematically higher for the oxidized specimens indicating higher compressibility.

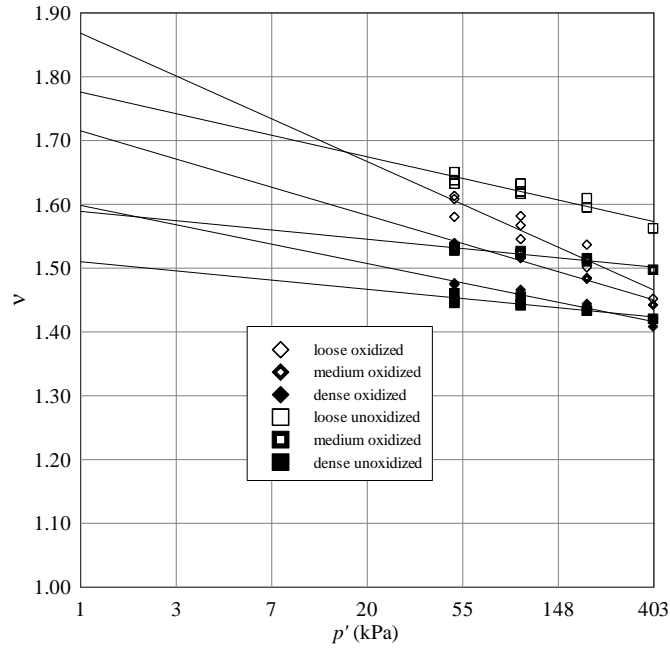


Figure 6.1 Unloading-reloading lines for each range of initial  $D_R$ .

Table 6.1 Critical state parameters during isotropic compression determined for each range of initial  $D_R$ .

	$D_R$	$\kappa$	$v_{\kappa}$	$R^2$
Unoxidized	loose	0.034	1.78	0.88
	medium	0.015	1.59	0.91
	dense	0.014	1.51	0.91
Oxidized	loose	0.067	1.87	0.89
	medium	0.044	1.72	0.98
	dense	0.030	1.60	0.94

## 6.3 Drained Monotonic Loading

### 6.3.1 Typical Stress-Strain-Volumetric Response

While results from all 18 triaxial tests performed in this study are presented in Chapter 5, this section will focus on a few specific tests in order to focus on the differences in the mechanical response of the unoxidized and oxidized specimens. During triaxial testing, one of the unoxidized and one of the oxidized specimens were isotropically compressed to identical levels of  $D_R = 83\%$  at  $p' = 200$  kPa. This allows comparison of the mechanical response of the two *MWR* materials before peak as shown in Figures 6.2 and 6.3.

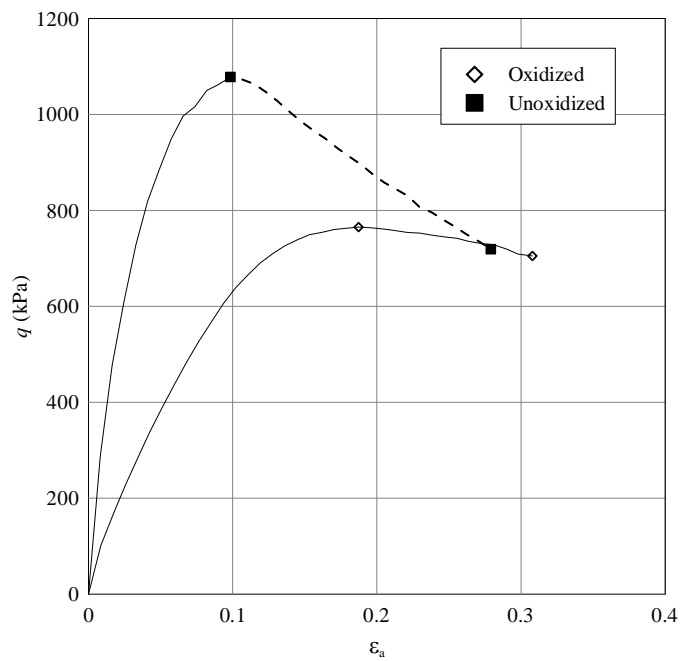


Figure 6.2 Deviatoric stress  $q$  versus axial strain  $\epsilon_a$  for and unoxidized and oxidized specimen consolidated to an identical initial state in terms of  $D_R$  and  $p'$  (data points correspond to measured values of peak and critical state  $q$ ).

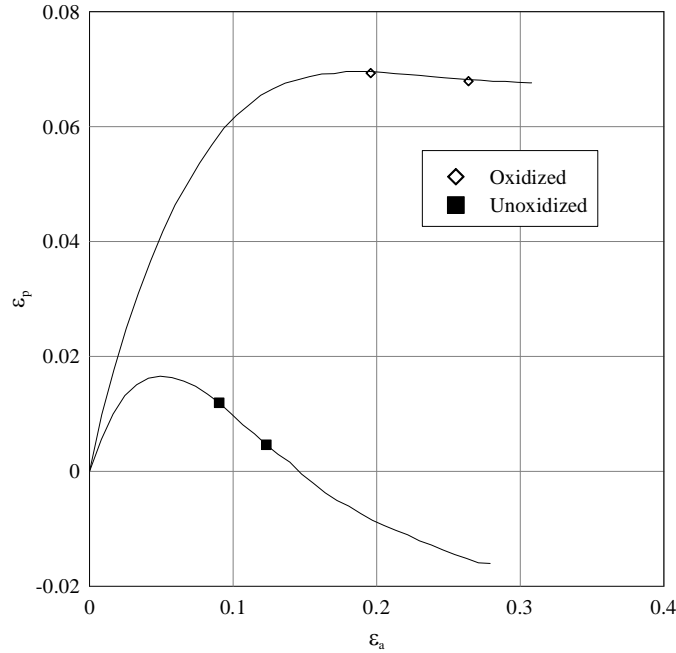


Figure 6.3 Volumetric strain  $\epsilon_p$  versus axial strain  $\epsilon_a$  for unoxidized and oxidized specimen consolidated to an identical initial state in terms of  $D_R$  and  $p'$  (data points correspond to ranges of maximum dilatancy rate).

The mechanical response of the two *MWR* types is observed to be quite different before peak in Figures 6.2 and 6.3 during drained axisymmetric compression. Under identical initial states of  $D_R$  and  $p'$  the materials have a nearly opposite response in terms of strain-hardening and possibly, strain-softening behavior (Fig. 6.2). The peak dilatancy rate in the unoxidized specimens is observed to be more than ten times greater than the peak dilatancy rate of the oxidized specimen (Tables 5.1 & 5.2). The difference in peak dilatancy rate lead to an observed value of  $(\phi_p - \phi_c)$  which was equal to  $7^\circ$  for the unoxidized specimen, while the value of  $(\phi_p - \phi_c)$  for the oxidized specimen was equal to  $4^\circ$ .

### 6.3.2 Critical State Friction Angle

Critical state values for  $p'$ ,  $q$  and  $v$  are all defined for each specific test at the point of maximum axial strain ( $\epsilon_a$ ). The location of the critical state line (*CSL*) may be estimated from the data points corresponding to the critical states of unoxidized and oxidized specimens for tests which did not exhibit shear bands in  $\ln(p')$  -  $v$  space (Figure 6.4) and in  $p'$  -  $q$  space (Figure 6.5). The *CSL* in  $p'$  -  $q$  space has a coefficient of determination ( $R^2$ ) greater than 0.995 for each *MWR* material. On the other hand, the  $R^2$  for the *CSL* in  $\ln(p')$  -  $v$  space are much lower at 0.71 and 0.78 for the unoxidized and oxidized specimens, respectively. These results are similar to those presented in the literature for granular geomaterials tested under these levels of  $p'$  (Been and Jefferies 2000). The *CSL* in  $\ln(p')$  -  $v$  space indicates the values of the critical state soil parameters  $\lambda_{cs}$  and  $\Gamma_{cs}$  as the slope and  $v$  intercept at  $p' = 1$  kPa of the *CSL* (Muir-Wood 1990). The critical state soil parameter  $M$  was estimated from the plot of the *CSL* in  $p'$  -  $q$  space for all tests exhibiting bulging failure. The value of  $M$  is also related to the value of  $\phi_c$  for all tests for a given material. Results are presented in Figure 6.5 where the critical state values of  $p'$  -  $q$  are plotted for all tests exhibiting bulging failure. This approach indicates that the value of  $\phi_c$  of the oxidized material is equal to  $36.7^\circ$  while the  $\phi_c$  of the unoxidized material is equal to  $38.3^\circ$ . Values determined for critical state parameters ( $\Gamma_{cs}$ ,  $M$ , and  $\lambda_{cs}$ ) are summarized in Table 6.2 for each *MWR* material.

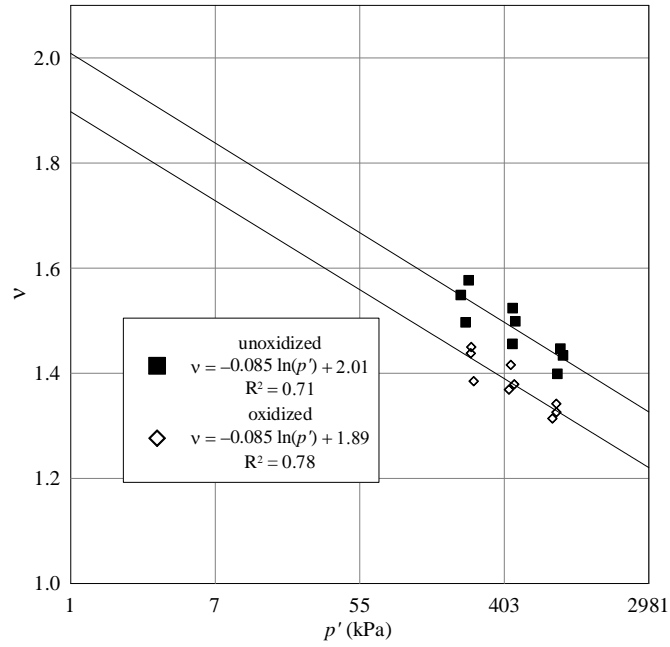


Figure 6.4 *CSL* in  $\ln(p')$  –  $v$  space for unoxidized and oxidized specimens used to determine the critical state parameters  $\Gamma_{cs}$  and  $\lambda_{cs}$ .

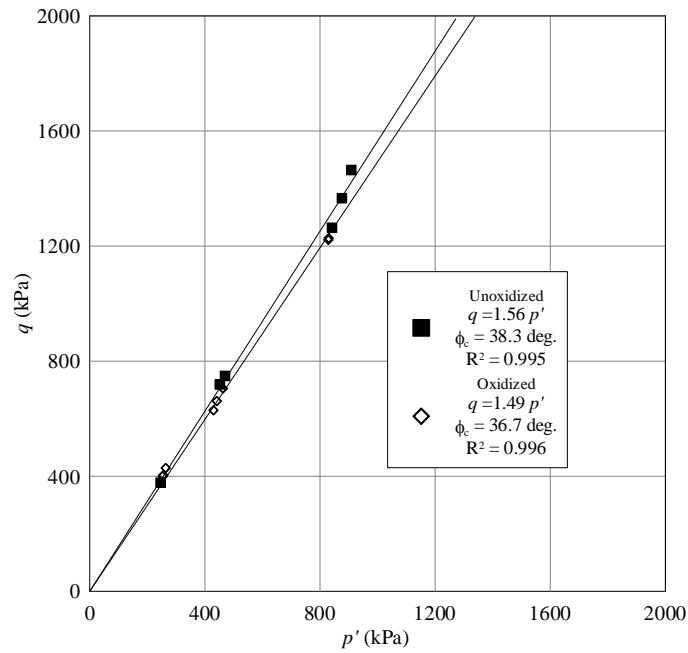


Figure 6.5 *CSL* in  $p'$ - $q$  space for unoxidized and oxidized specimens with a linear best-fit value of  $M$  and the corresponding value of  $\phi_c$

Table 6.2 Critical state parameters determined from the *CSL* in  $p' - q$  space and  $\ln(p') - v$  spaces.

	M	$\Gamma_{cs}$	$\lambda_{cs}$
Unoxidized	1.56	2.01	0.085
Oxidized	1.49	1.89	0.085

As discussed previously, the apparent critical state friction angle observed at the highest levels of axial strain in the triaxial apparatus may still contain components of shearing resistance due to (1) dilatancy and (2) particle breakage. This occurrence may be more apparent for tests in which the criteria for critical state ( $\delta v / \delta \varepsilon_a = \delta p' / \delta \varepsilon_a = \delta q / \delta \varepsilon_a = 0$ ) are not necessarily met. In geomaterials that experience particle breakage during shearing, the apparent critical state friction angle mobilized at the highest levels of  $\varepsilon_a$  may contain both frictional and clastic components (Tarantino and Hyde 2005). Particle breakage may continue in some geomaterials with weak grains (such as calcareous Dog's Bay sand) up to shear strains equal to 11,000% (Coop et al. 2004), which will further influence the estimated value of  $\phi_c$ . If a stable fractal dimension is achieved at the highest levels of  $p'$ , particle breakage levels off and the value of  $\phi_c$  estimated from these tests may most accurately represent the intrinsic frictional characteristics of the geomaterial (Tarantino and Hyde 2005) at critical state. In tests reconstituted to the loosest  $D_R$  and consolidated to the highest  $p'$ , the specimen states at the highest levels of axial strain come very close to meeting the critical state criteria. The value of the fractal dimension ( $D$ ) for these specimens was also shown to level off after testing at this highest level of level of  $p'$  (Fig. 6.6). The low density, high stress state tests exhibited only bulging failure mechanisms, making membrane and area corrections more reliable as the presence of shear planes severely complicates the proper membrane and area corrections to be made.

With this in mind, the values of  $\phi_c$  for the unoxidized and oxidized *MWR* were determined by evaluating tests at the critical state which (1) most nearly met the critical state criteria ( $\delta v/\delta \epsilon_a = \delta p'/\delta \epsilon_a = \delta q/\delta \epsilon_a = 0$ ) and (2) were reconstituted to the loosest  $D_R$  and isotropically compressed to the highest  $p'$  in order to achieve the highest and most stable value of  $D$  after drained axisymmetric compression (Figure 6.6). Tests U48-400 and O87-400 in Tables 5.1 and 5.2 met these two criteria and were therefore used to determine final values of  $\phi_c$  equal to  $38^\circ$  and  $36^\circ$  for the unoxidized and oxidized materials, respectively. From a physical point of view, a stable value of  $D$  suggests that particle breakage has leveled off while meeting the critical state criteria suggests that the dilatancy rate has approached zero, thus the friction angle mobilized in these tests may best represent truly intrinsic frictional characteristics of a geomaterial (Tarantino and Hyde 2005, Coop et al. 2004).

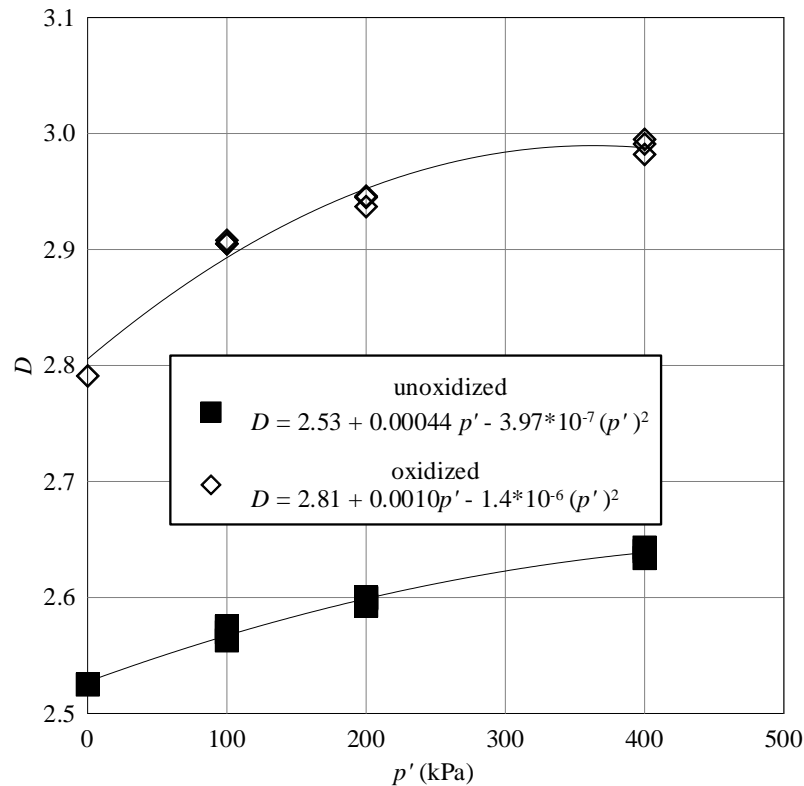


Figure 6.6 Evolution of the  $D$  after triaxial shearing at various levels of  $p'$  including 2<sup>nd</sup> order polynomial lines of best fit.

### 6.3.3 Stress-Dilatancy Relationship

Bolton (1986) evaluated the stress-dilatancy relationship for various types of clean sands and developed Eq. 6.1 which relates  $\phi_p$  mobilized under axisymmetric loading to the state variables  $D_R$  and  $p'_p$  and the intrinsic parameters of the soil  $\phi_c$ ,  $Q$ , and  $R$  through the relative dilatancy index  $I_R$ .

$$I_R = \frac{\phi_p - \phi_c}{3} = I_D [Q - \ln(p'_p)] - R \quad (6.1)$$

where  $I_D = D_R(\%)/100 =$  relative density after isotropic compression and  $Q$  and  $R$  are intrinsic material parameters. This relationship is presented in Figure 6.7 in a slightly modified format as presented by Salgado et al. (2000) where  $Q$  and  $R$  may be determined for each material from the slope and intercept of the best fit lines going through the data plotted in  $I_R + I_D \ln(p'_p)$  versus  $I_D$  space . The critical state friction angle ( $\phi_c$ ) and Bolton's (1986) fitting parameters  $Q$  and  $R$  are summarized in Table 6.3 for the two *MWR* materials tested.

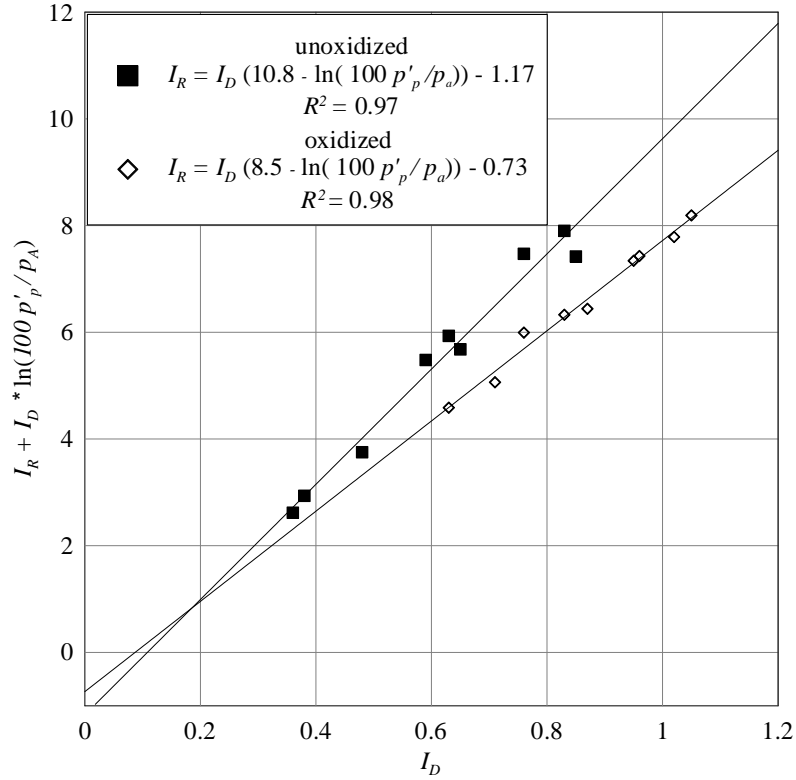


Figure 6.7 Dilatancy response of unoxidized and oxidized *MWR*

Table 6.3 Critical state friction angle and Bolton’s (1986)  $\phi_p$ -correlation fitting parameters  $Q$  and  $R$ .

	$\phi_c$ (°)	$Q$	$R$
Oxidized	36	8.5	0.73
Unoxidized	38	10.8	1.17

Eq. 6.1 was shown to predict  $\phi_p$  very accurately for each *MWR* material. This point is illustrated in Tables 6.4 and 6.5 where  $\phi_p$  measured in each test is compared to the  $\phi_p$  predicted using Eq. 6.1 and Table 6.3 data for the unoxidized and oxidized *MWR* tested in this study. The term  $\Delta\phi_p$  shown in Tables 6.4 & 6.5 represents the difference between the measured and predicted values of  $\phi_p$  for each test. Results show a maximum absolute

difference in the predicted values of  $\phi_p$  which is less than 2 deg. for the *MWR* materials tested in this study.

Table 6.4 Comparison of values of  $\phi_p$  predicted using Eq. 6.1 with values of  $\phi_p$  measured in individual tests for the unoxidized *MWR*.

		$\phi_c$	$Q$	$R$		
		38	10.8	1.17		
Test	$p_p'$ (kPa)	$I_D$	$\phi_p$ (predicted)	$\phi_p$ (calculated)	$\Delta\phi_p$	
U36-100	249	0.36	40.2	39.9	0.3	
U59-100	287	0.59	43.6	44.4	-0.8	
U76-100	315	0.76	46.0	47.3	-1.3	
U38-200	472	0.38	39.8	39.8	0.0	
U63-200	537	0.63	43.0	43.9	-0.9	
U83-200	571	0.83	45.6	45.9	-0.3	
U48-400	902	0.48	40.2	39.5	0.8	
U65-400	965	0.65	42.1	41.6	0.5	
U85-400	991	0.85	44.4	42.7	1.8	

Table 6.5 Comparison of values of  $\phi_p$  predicted using Eq. 6.1 with values of  $\phi_p$  measured in individual tests for the oxidized *MWR*.

		$\phi_c$	$Q$	$R$		
		36	8.5	0.73		
Test	$p_p'$ (kPa)	$I_D$	$\phi_p$ (predicted)	$\phi_p$ (calculated)	$\Delta\phi_p$	
O63-100	257	0.63	39.3	39.3	0.0	
O76-100	265	0.76	40.4	41.3	-0.9	
O102-100	282	1.02	42.4	42.1	0.3	
O72-200	452	0.71	38.8	38.2	0.6	
O83-200	477	0.83	39.5	39.6	-0.1	
O95-200	478	0.95	40.3	40.4	-0.1	
O87-400	856	0.87	38.2	37.7	0.5	
O96-400	881	0.96	38.6	38.8	-0.1	
O105-400	890	1.05	39.0	39.2	-0.1	

## 6.4 Particle Strength

Values of  $I_{s(50)}$  for the unoxidized specimens classified as Very High to Extremely High according to ASTM D5731-08, while the values of  $I_{s(50)}$  for oxidized specimens classified as Medium to High. The average values of  $I_{s(50)}$  including tests parallel and perpendicular to the planes of weakness fall almost directly on the border between Very High and Extremely High (10 MPa) for the unoxidized specimens and similarly near the border between Medium and High (1 MPa) for the oxidized specimens.  $I_{s(50)}$  determined for the unoxidized *MWR* particles are approximately ten times greater than  $I_{s(50)}$  determined for the oxidized specimens (Table 5.3).

The unoxidized *MWR* also returns a higher value of  $Q = 10.8$  relative to the oxidized *MWR* where  $Q = 8.5$ . Billam (1972) reported values of  $I_{s(50)}$  equal to 0.76 MPa for granulated chalk, 8.96 MPa for crushed anthracite, 21.37 MPa for limestone sand and 139.3 MPa for Ham River sand along with drained axisymmetric compression results. Based on the stress-dilatancy behavior observed by Billam (1972), Bolton (1986) suggested a value of  $Q$  equal to 5.5 for chalk, 8 for limestone, 7 for anthracite, and 10 for quartz. These different values of  $Q$  are somewhat related to the grain tensile strength and the  $p'$  required to suppress dilatancy for a given geomaterial (McDowell and Bolton 1998, Bolton 1986). Lee (1992) also noted that the difference ( $\phi_p - \phi_c$ ) is linearly dependent on the logarithm of  $p'$  normalized by grain tensile strength for specimens tested at the same initial  $D_R = 87\%$  (Fig. 2.12). Similar observations are made regarding particle strength, dilatancy and the calculated value of  $Q$  for each *MWR* type tested in this study (Fig. 6.8). Since specimens in this study were isotropically compressed to over a

wide range of  $D_R$ , the slope of  $(\phi_p - \phi_c)$  vs.  $p'/I_{s(50)}$  is dependent upon the value of  $D_R$  and results are presented in Figure 6.8 for “loose”, “medium” and “dense” specimens.

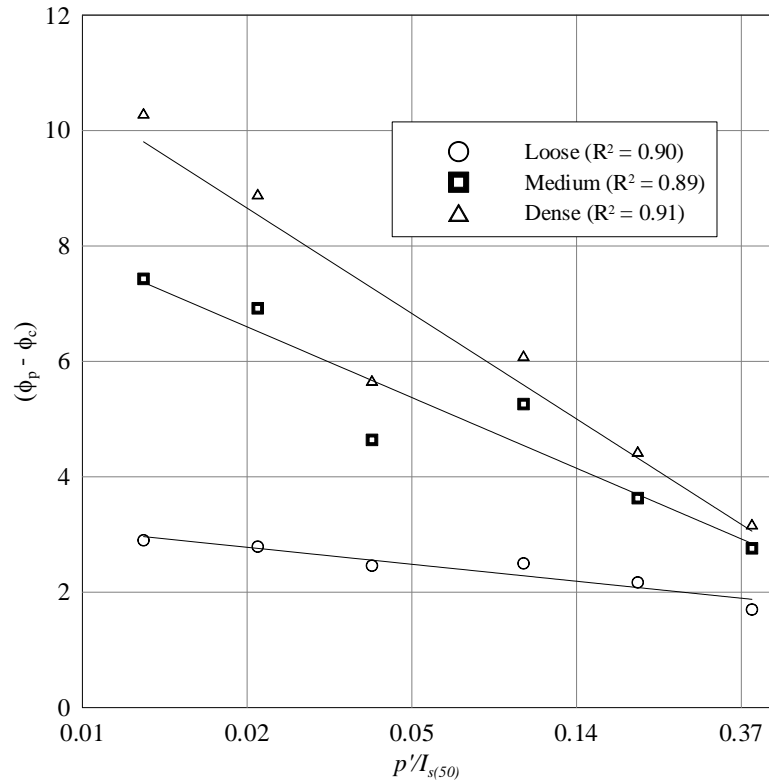


Figure 6.8  $(\phi_p - \phi_c)$  vs.  $p'/I_{s(50)}$

Since dilatancy will decrease as  $D_R$  decreases from 100% to 0%, all else being the same, the values of  $(\phi_p - \phi_c)$  may be normalized by  $D_R$  in order to make a more general comparison with the values of  $p'/I_{s(50)}$  (Figure 6.9). This approach gives a reasonable correlation ( $R^2 = 0.79$ ) for this trend, although there is no mechanistic justification for the normalization of  $(\phi_p - \phi_c)$  by the value of  $D_R$  after isotropic compression at the start of axisymmetric compression.

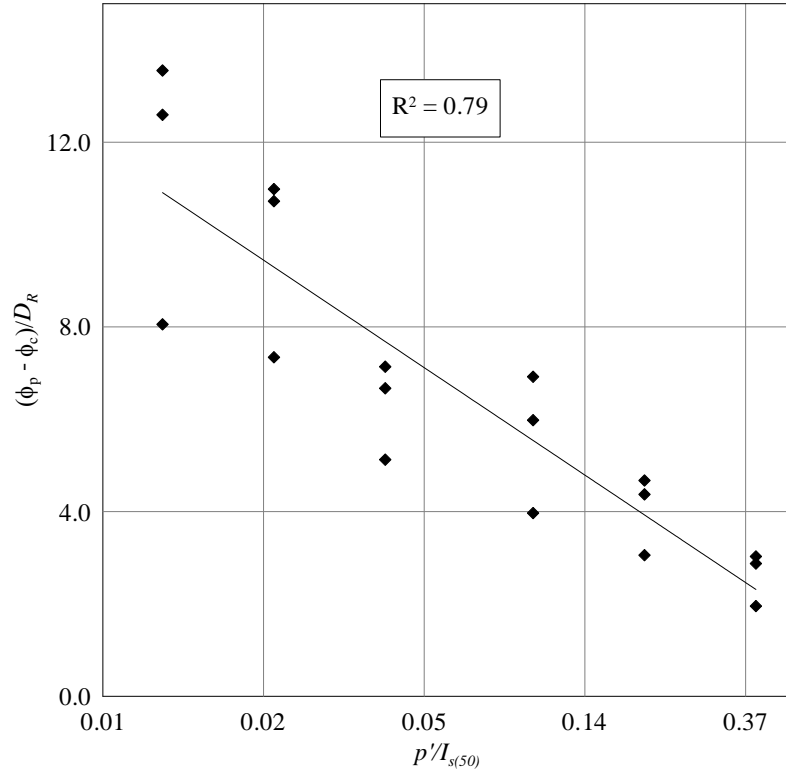


Figure 6.9  $(\phi_p - \phi_c)/D_R$  vs.  $p'/I_{s(50)}$

### 6.5 Particle Breakage

Particle size distributions were completed after testing in order to determine the combined particle breakage effects of isotropic compression and drained axisymmetric compression. Particle breakage was not determined after isotropic compression alone. Particle breakage was found to increase with the  $p'$  that the specimen was isotropically compressed to before drained axisymmetric compression. On the other hand, the level of  $D_R$  achieved after isotropic compression was shown to have a negligible effect on particle breakage. This point is demonstrated in Tables 5.6 and 5.7 as well as in Figure 6.6 and 5.12. Particle size distributions determined before and after each test are presented in Appendix B. As seen in Figure 5.12, oxidized samples experienced more particle

breakage than the unoxidized samples tested at identical levels of  $D_R$  and  $p'$ . Dilatancy was also suppressed in the oxidized specimen to a tenth of that of the unoxidized specimen tested at identical levels of  $D_R$  and  $p'$ . These observations help confirm that the reduced values of  $Q$  may indeed be related to the reduced dilatancy and increased particle breakage in particles with weaker grain tensile strengths.

## 6.6 Fractal Dimension

The initial fractal dimension ( $D$ ) for all unoxidized specimens was equal to 2.53 and the initial  $D$  of all oxidized specimens was 2.79. Figure 6.6 and Tables 5.5 and 5.6 demonstrate the evolution of  $D$  after testing at various levels of  $p'$ . The data points in Figure 6.6 corresponding to  $p' = 0$  kPa represent the initial  $D$  of the material before testing. There are actually three data points at each level of  $p'$  which correspond to the “loose”, “medium”, and “dense”  $D_R$  states (see Tables 5.3 & 5.4 for exact values of  $D_R$  and  $D$ ). Figure 6.6 shows the relatively minor effect that  $D_R$  has on the evolution of  $D$  relative to the impact of  $p'$  on the evolution of  $D$  for the *MWR* types tested. The best-fit lines in Figure 6.6 suggest that a stable fractal dimension is approached at the highest levels of  $p'$  for the oxidized material. Larger  $p'$  levels may be required to clearly identify a similar trend for the unoxidized material. Thus, the ‘true’ critical state may be systematically evaluated in triaxial tests which (1) meet the critical state criteria ( $\delta v / \delta \varepsilon_a = \delta p' / \delta \varepsilon_a = \delta q / \delta \varepsilon_a = 0$ ) at the highest levels of axial strain (2) approach a stable  $D$  for the material and (3) do not contain shear bands. Thus, for materials tested in the present study, this approach may be valid for the oxidized material. The unoxidized *MWR* may

require larger  $p'$  levels to fully allow identification of a true critical state due to its stronger grains.

## 6.7 Surface Energy

In an attempt to validate the modified work equation (Eq. 3.20), particle size distributions were determined for each specimen after shearing allowing for the change in total surface area ( $dS$ ) of a specimen to be estimated. The surface energy of solid materials ( $\Gamma_{se}$ ) is the parameter in Eq. 3.20 that is most difficult to accurately determine. With this in mind, values of the surface energy ( $\Gamma_{se}$ ) of each triaxial specimen were calculated by integrating Eq. 3.20 during drained monotonic loading over the range of  $\varepsilon_q$  achieved during the test and solving for  $\Gamma_{se}$  with the values of  $\beta_s$ ,  $\beta_v$  and  $dS$  determined from the particle size distributions before and after testing. These calculated values of  $\Gamma_{se}$  (5-24 J/m<sup>2</sup>) are of similar magnitude as those presented in the literature (3-50 J/m<sup>2</sup>) for various rock types (Ashby and Jones 1986, Friedman et al. 1972). While understanding the significant limitations associated with accurate determination of  $\Gamma_{se}$ , Eq. 3.20 has been employed with apparent success for materials tested in this study given that the value of  $\Gamma_{se}$  does in fact lie in the range of values reported in the literature for common rock types. Values of  $\Gamma_{se}$  calculated using Eq. 3.20 are presented for each individual test in Table 6.7 and 6.8. A detailed example of how  $\Gamma_{se}$  was calculated for a select specimen is provided in Appendix A. Values of  $dS$  may be of limited accuracy due to the assumed values of  $\beta_s$  and  $\beta_v$ , which may explain the differences in the calculated values of  $\Gamma_{se}$ .

Table 6.6 Values of  $\Gamma_{se}$  and  $dS$  determined for each unoxidized *LSTX* specimen

Test	$\Gamma_{se}$ (J/m <sup>2</sup> )	$dS$ (m <sup>2</sup> )
U36-100	8	3
U59-100	8	3
U76-100	13	3
U38-200	22	4
U63-200	19	5
U83-200	20	5
U48-400	21	7
U65-400	24	8
U85-400	13	8

Table 6.7 Values of  $\Gamma_{se}$  and  $dS$  determined for each oxidized *LSTX* specimen

Test	$\Gamma_{se}$ (J/m <sup>2</sup> )	$dS$ (m <sup>2</sup> )
O63-100	8	8
O76-100	9	9
O102-100	5	14
O72-200	15	6
O83-200	6	18
O95-200	9	18
O87-400	7	21
O96-400	9	20
O105-400	8	22

The physical meaning of  $\Gamma_{se}$  is related to the external energy required to propagate a stable tensile fracture through a rock (Freidman et al. 1972). An increase in  $\Gamma_{se}$  is related to an increase in the energy required to fracture a rock of a given size. Ductile and brittle failure mechanisms also affect the energy required to fracture a rock. Average values of  $\Gamma_{se}$  are calculated as 16 J/m<sup>2</sup> and 9 J/m<sup>2</sup> for the unoxidized and oxidized specimens, respectively, suggesting that the unoxidized material requires more energy to fracture than the oxidized material if the particle failure mechanisms are similar in terms of brittle vs. ductile failure. This result seems reasonable considering that the unoxidized material

has a grain tensile strength which is ten times greater than the grain tensile strength of the oxidized material.

### 6.8 Acid-base Accounting

Acid-base accounting was used in order to (1) justify the oxidized-unoxidized terminology used in the study to differentiate between two *MWR* materials and (2) give an indication of the effects that *in situ* weathering by oxidation may have on the intrinsic strength properties of *MWR* derived from more or less oxidized zones of a sedimentary rock deposit overlying a sediment-hosted precious metal deposit. While the focus of the present study is mechanical behavior of *MWR*, further study of more intrinsic differences in the mineralogy and weathering history are needed before further claims can be made. Acid-base accounting is nothing more than an indicator of current mineralogical differences between the two materials and no claim can be made that the two materials were initially identical before oxidation.

Results from the acid-base accounting (Table 5.7) show a marked difference in the *NP* between the two materials with the unoxidized value equal to 329 kg of  $\text{CaCO}_3/\text{Mg}$  and the oxidized value equal to 12 kg of  $\text{CaCO}_3/\text{Mg}$  suggesting that the presence of water, oxygen, pyrite and other minerals may be responsible for the depletion of the  $\text{CaCO}_3$  in the oxidized material relative to the unoxidized material. On the other hand, the *AP* of the two materials is quite similar at 40 kg of  $\text{CaCO}_3/\text{Mg}$  and 36 kg of  $\text{CaCO}_3/\text{Mg}$  for the unoxidized and oxidized specimens, respectively. *AP* values are less indicative of a difference between the two materials due to weathering by oxidation.

While this is a relatively limited set of data, results suggest that *in situ* oxidation may have significantly reduced the  $NP$  of the ‘unoxidized’ material to that of the ‘oxidized’ material. The  $AP$  of the oxidized material was just slightly less than that of the unoxidized material. There is no indication that the original rock types were exactly identical, making direct comparison of these values difficult. Direct comparisons could be made with a more rigorous and fundamental description of the mineralogy and weathering that has occurred in the two  $MWR$  materials. With a more complete description of the history and mineralogy of these materials, a relationship between weathering by oxidation and intrinsic shear strength parameters (such as  $\phi_c$ ,  $Q$  and  $R$ ) may be developed.

## CHAPTER 7: CONCLUSIONS

### 7.1 Summary

A systematic study was conducted to study the mechanical behavior of unoxidized and oxidized *MWR* material. The unoxidized and oxidized *MWR* was taken from the same geologic formation. Hydrogeologic conditions led to one sample being heavily weathered by oxidation while the other was less weathered. Particle size distributions were modeled to be parallel to the collected field gradations, which were quite similar, although the oxidized samples contained a slightly higher fines content and had more well-graded (or less uniform) particle size distributions. The intrinsic shear strength parameters  $\phi_c$ ,  $Q$ , and  $R$  of the *MWR* materials were determined and particle strength was evaluated through point load strength testing. Evidence from a variety of experimental protocols suggest that the observed differences in the mechanical response may be linked to differences in particle strength and particle breakage between the two materials during compressive loading. Main conclusions taken from this study are summarized in the following sections.

#### 7.1.1 Specimen Preparation and Uniformity

A method of reconstituting repeatable and uniform *LSTX* specimens was developed and implemented in this study. The method is based on a slight modification of the initial sample placement procedure outlined by the ASTM standards used to determine the maximum void ratio ( $e_{max}$ ) of granular geomaterials. The method was shown to lead to reconstituted specimens which were uniform and repeatable in terms of  $D_R$ , with initial

values of  $D_R$  varying by less than 10% between the top and bottom lifts for all levels of  $D_R$  tested (Tables 4.2 & 4.3).

## 7.1.2 Drained Monotonic Response

### 7.1.2.1 Critical State Friction Angle

The critical state friction angle ( $\phi_c$ ) of the unoxidized *MWR* was found to be just  $2^\circ$  greater than  $\phi_c$  of the oxidized *MWR* (Table 6.3). These values were determined by evaluating specimens reconstituted to the loosest state in terms of  $D_R$  before being isotropically consolidated to the highest levels of  $p'$ . Tests U48-400 and O87-400 in Tables 5.1 and 5.2 met the critical state criteria and were therefore preferably used to estimate  $\phi_c$ . These results agree well with the plots of the *CSL* in  $p' - q$  space which gives a value of  $M$  which is related to the value of  $\phi_c$  determined for each test exhibiting bulging failure.

### 7.1.2.2 Stress-Dilatancy Relationship

The peak dilatancy rate  $(-\delta\varepsilon_p / \delta\varepsilon_a)_{\max}$  of the unoxidized *MWR* is ten times greater than that of the oxidized *MWR* for two specimens which were consolidated to identical levels of  $p'$  and  $D_R$ . More generally, the average  $(-\delta\varepsilon_p / \delta\varepsilon_a)_{\max}$  observed in all unoxidized specimens was equal to 0.13 while the average  $(-\delta\varepsilon_p / \delta\varepsilon_a)_{\max}$  observed in all oxidized specimens was equal to 0.03. These differences in peak dilatancy rate agree well with the reduced values of  $(\phi_p - \phi_c)$  and  $Q$  in the oxidized *MWR* relative to the unoxidized *MWR*. Values of  $Q$  were determined to be equal to 10.8 and 8.5 for the unoxidized and oxidized

*MWR*, respectively. Values of  $R$  were determined to be equal to 1.17 and 0.73 for the unoxidized and oxidized *MWR*, respectively. These values of  $Q$  and  $R$  are similar to the values presented by Bolton (1986) for geomaterials with similar grain tensile strengths. These values of  $Q$  and  $R$  also give an accurate estimation ( $\pm 2$  deg.) of the peak friction angle for each *MWR* material at a given state in terms of  $D_R$  and  $p'$ .

### 7.1.2.3 General Stress-Strain-Volumetric Response

The mechanical response of the two materials is shown to be quite different in many ways. The oxidized *MWR* exhibited much more contractive behavior than the unoxidized *MWR* for all ranges of  $p'$  and  $D_R$  tested in the study. Net contraction (meaning the specimen volume decreased during the axisymmetric compression stage) was observed in all oxidized specimens, while three unoxidized specimens exhibited net expansion (meaning the specimen volume increased during the axisymmetric compression stage). These observations go hand-in-hand with the values of  $(\phi_p - \phi_c)$ ,  $Q$ , and  $(-\delta\varepsilon_p / \delta\varepsilon_a)_{\max}$  determined for each *MWR* material.

### 7.1.3 Particle Breakage and Fractal Dimension

Particle breakage is also shown to be more pronounced in the oxidized *MWR* by evaluating the fractal dimension ( $D$ ) before and after testing. This was done by determining the particle size distribution before the isotropic and axisymmetric compression stages and after the isotropic and axisymmetric compression stages. Particle size distributions were not determined after isotropic compression alone. Changes in the values of  $D$  for the oxidized *MWR* were typically twice that of the unoxidized *MWR* at a

given level of  $p'$ .  $D_R$  was shown to have a somewhat negligible effect on the changes in  $D$  relative to the effect of  $p'$ . Particle strength was quantified through point load strength testing to provide an estimate of the unoxidized grain tensile strength (10.2 MPa), which is ten times greater than the grain tensile strength of the oxidized *MWR* (1.02 MPa). For geomaterials exhibiting particle breakage during compressive loading, the dilatancy angle ( $\psi$ ) has been shown to have a linear dependence on  $p'$  only when the value of  $p'$  is normalized by grain tensile strength and  $D_R$  remains constant (Lee 1992). In this study, the linear relationship between  $\psi$  and  $p'$  normalized by grain tensile strength was shown to also depend on the level of  $D_R$  at the start of axisymmetric compression (Figures 6.8 and 6.9). If  $\psi$  is normalized by the level of  $D_R$  at the start of axisymmetric compression, a linear trend is observed for all specimens (Figure 6.9).

#### 7.1.4 Surface Energy

A constant fractal dimension ( $D$ ) was approached for each *MWR* material after testing at the highest levels of  $p'$ , which validates the underlying assumptions of the modified work equation (Eq. 3.20) presented by McDowell et al. (1996). The surface energy of solid materials ( $\Gamma_{se}$ ) is a parameter that is extremely difficult to accurately determine. In an attempt to validate the modified work equation (Eq. 3.20), values of the surface energy ( $\Gamma_{se}$ ) of each triaxial specimen were calculated (Tables 6.6 and 6.7). A detailed example of how  $\Gamma_{se}$  was calculated for a select specimen is provided in Appendix C. These calculated values (3-22 J/m<sup>2</sup>) are of similar magnitude as those presented in the literature (3-50 J/m<sup>2</sup>) for various rock types.

### 7.1.5 Acid-Base Accounting

The relative degree of weathering by oxidation between the unoxidized and oxidized *MWR* was investigated using acid-base accounting. Results show a reduced neutralization potential (*NP*) and acid producing potential (*AP*) in the oxidized material. *In situ* weathering by oxidation is shown to strongly influence the mechanical behavior of *MWR*. While the  $\phi_c$  of the oxidized material ( $36^\circ$ ) is quite similar to that of the unoxidized material ( $38^\circ$ ), the dilatancy angle is generally greater for the unoxidized material than for the oxidized material. This may be due to the suppression of dilatancy that may occur when particles are too weak to dilate and break instead. Acid-base accounting results suggest that weaker particle strengths may have a direct correlation with *in situ* weathering by oxidation.

### 7.2 Suggestions for Future Work

Based on results from this systematic study, the following topics are suggested for future study involving the mechanical behavior of *MWR*:

1. Future studies attempting to address strength degradation must be based on a mechanistically-sound framework such as the one used in this study. Analyses based on an empirical, conceptual framework such as those associated with a  $\phi'$ - $c'$  model are inadequate and should be discontinued if the true causes of mechanical degradation of *MWR* are to be properly understood.

2. Further investigation of the differences in mechanical behavior between parallel gradations of geomaterials used to model specimens with particle sizes that are appropriate for a given testing apparatus.
3. Further study on the limiting ranges of the shape and volume factors,  $\beta_s$  and  $\beta_v$  for a variety of particle shapes in order to accurately assess the  $dS$  term of the modified work equation presented by McDowell et al. (1996).
4. Further study regarding proper evaluation of the surface energy ( $\Gamma_{se}$ ) of solid materials in order to further validate the modified work equation presented by McDowell et al. (1996).
5. Further study on the evolution of the fractal dimension  $D$  for the *MWR* materials at higher levels of  $p'$ . The establishment of a constant fractal dimension for a geomaterials will allow further validation of the modified work equation presented by McDowell et al. (1996), which assumes that an assembly of breakable particles will develop fractal characteristics during compressive loading.
6. Further commentary on the changes in surface area during isotropic loading. In this study, particle breakage was measured after the combined effects of isotropic compression and axisymmetric shearing. Quantifying particle breakage during isotropic loading will allow for a more accurate assessment of  $dS$  and  $\Gamma_{se}$  by satisfying the modified work equation presented by McDowell et al. (1996) during axisymmetric compression alone.
7. Further study of the mineralogy, weathering and geochemistry characteristics of the unoxidized and oxidized *MWR* in order to gain a better understanding of the

specific weathering processes that may lead to the observed differences in the mechanical behavior between the two *MWR* types. A better understanding of the weathering characteristics may provide a more clear understanding of the relationship between *in situ* weathering and the systematic strength degradation analysis carried out in this study.

## APPENDIX A – EVALUATING THE MODIFIED WORK EQUATION

### A.1 Introduction

In an attempt to validate the modified Cam Clay work equation presented by McDowell et al. (1996), each triaxial test presented in this manuscript was evaluated during the axisymmetric compression stage according to Eq. A.1. The equation is based on conservation of energy within a soil element by balancing the plastic work done with the internal energy dissipation due to (1) friction between soil particles and (2) particle breakage. The origin of this equation is thoroughly described in Section 3.3, however this appendix serves as a step by step example of how values of  $\Gamma_{se}$  reported in Tables 6.6 and 6.7 were calculated in this study.

$$q\delta\varepsilon_q^p + p'\delta\varepsilon_p^p = Mp'\delta\varepsilon_q^p + \frac{\Gamma_{se}dS}{V_s(1+e)} \quad (\text{A.1})$$

where  $q$  = deviatoric stress invariant (kPa),  $\delta\varepsilon_q^p$  = deviatoric strain increment (%),  $p'$  = octahedral mean stress invariant (kPa),  $\delta\varepsilon_p^p$  = octahedral mean strain increment (%),  $M = (q/p')_{cs} = 1.56$  (Unoxidized *MWR*) or 1.49 (Oxidized *MWR*),  $\Gamma_{se}$  = surface energy (J/m<sup>2</sup>), and  $dS = S_f - S_i$  is the change in surface area (m<sup>2</sup>) of a volume of solids,  $V_s$  (m<sup>3</sup>), distributed throughout a total specific volume of  $(1+e)$ .  $V_s$  is a constant throughout the test.

Stress invariants  $q$  and  $p'$  and strain increments  $\delta\varepsilon_q^p$  and  $\delta\varepsilon_p^p$  were determined as part of a typical triaxial testing program in order to develop an understanding of the stress-strain-volumetric response of a geomaterial. The value of  $V_s$  is known and constant throughout

testing, however the value of  $(1+e)$  deviates with  $\beta_s$  and  $\beta_v$ . As mentioned in Section 3.3, the value of the initial surface area ( $S_i$ ) was estimated by assuming shape and volume factors ( $\beta_s$  and  $\beta_v$ ) equal to those reported by Marsal (1973) for angular rockfill and by knowing the particle size distribution of each specimen before testing. The final surface area ( $S_f$ ) of the specimen was determined by completing a particle size distribution after testing and assuming that values of  $\beta_s$  and  $\beta_v$  remain constant. This allows Eq. A.1 to be evaluated over the strain increments where  $dS$  is known in order to calculate  $\Gamma_{se}$  as constant throughout a given test by integrating Eq. A.1 in an attempt to satisfy the principle of conservation of energy within a triaxial specimen during axisymmetric compression.

## A.2 Rearrangement of the Work Equation

Evaluating  $\Gamma_{se}$  through the modified work equation (Eq. A.1) requires simple algebraic manipulation:

$$q\delta\varepsilon_q^p + p'\delta\varepsilon_p^p = Mp'\delta\varepsilon_q^p + \frac{\Gamma_{se}dS}{V_s(1+e)} \quad (\text{A.1})$$

$$\frac{\Gamma_{se}dS}{V_s(1+e)} = [q\delta\varepsilon_q^p + p'\delta\varepsilon_p^p] - [Mp'\delta\varepsilon_q^p] \quad (\text{A.2})$$

$$\Gamma_{se}dS = V_s(1+e)\left[(q\delta\varepsilon_q^p + p'\delta\varepsilon_p^p) - (Mp'\delta\varepsilon_q^p)\right] \quad (\text{A.3})$$

$$\int_0^{\Delta S} \Gamma_{se}dS = \int_0^{\varepsilon_q^p} [V_s(1+e) \cdot q]d\varepsilon_q + \int_0^{\varepsilon_p^p} [V_s(1+e) \cdot p']d\varepsilon_p - \int_0^{\varepsilon_q^p} [V_s(1+e) \cdot M \cdot p']d\varepsilon_q \quad (\text{A.4})$$

$$\sum_{i=1}^{36} [\Gamma_{se}\Delta S] = \sum_{i=1}^{36} [V_s(1+e)(q\Delta\varepsilon_q^p + p'\Delta\varepsilon_p^p)] - \sum_{i=1}^{36} [V_s(1+e)(Mp'\Delta\varepsilon_q^p)] \quad (\text{A.5})$$

### A.3 Example Calculation for an Unoxidized Specimen (U59-200)

Knowing that  $V_s = 0.00359\text{-m}^3$  is constant throughout the test used for this example, for  $i$

= 1 (See Table A.1):

$$\Gamma_{se} dS = V_s (1 + e) \left[ (q \delta \varepsilon_q^p + p' \delta \varepsilon_p^p) - (M p' \delta \varepsilon_q^p) \right]$$

$$\begin{aligned} \Gamma_{se} \Delta S &= 0.00359 \text{ m}^3 \cdot (1.51) \cdot [264.4 \text{ kPa} \cdot (0.0063 - 0.000) + 285.5 \text{ kPa} \cdot (0.0061 - 0.000)] \\ &\quad - 0.00359 \text{ m}^3 \cdot (1.51) \cdot [1.56 \cdot 285.5 \text{ kPa} \cdot (0.0063 - 0.000)] \end{aligned}$$

$$\Gamma_{se} \Delta S = 0.00272 \text{ kN-m} = 2.72 \text{ N-m}$$

for  $i = 2$  (See Table A.1):

$$\Gamma_{se} dS = V_s (1 + e) \left[ (q \delta \varepsilon_q^p + p' \delta \varepsilon_p^p) - (M p' \delta \varepsilon_q^p) \right]$$

$$\begin{aligned} \Gamma_{se} \Delta S &= 0.00359 \text{ m}^3 \cdot (1.50) \cdot [393.7 \text{ kPa} \cdot (0.0130 - 0.0063) + 336.0 \text{ kPa} \cdot (0.0113 - 0.0061)] \\ &\quad - 0.00359 \text{ m}^3 \cdot (1.50) \cdot [1.56 \cdot 336.0 \text{ kPa} \cdot (0.013 - 0.0063)] \end{aligned}$$

$$\Gamma_{se} \Delta S = 0.00467 \text{ kN-m} = 4.67 \text{ N-m}$$

For the sum from  $i = 1$  to 36 (see the bottom of Table A.1):

$$\sum_{i=1}^{36} [\Gamma_{se} \Delta S] = 0.0889 \text{ kN-m} = 88.9 \text{ N-m}$$

Estimating  $\Delta S = 4.61 \text{ m}^2$  from particle size distributions before and after testing allows

calculation of  $\Gamma_{se}$ :

$$\Gamma_{se} = \frac{\sum_{i=1}^{36} [\Gamma_{se} \Delta S]}{\sum_{i=1}^{36} [\Delta S]} = \frac{88.9 \text{ N-m}}{4.61 \text{ m}^2} = 19.3 \text{ J/m}^2$$

Table A.1 Example Calculation of  $\Gamma_{se}$

i	$\varepsilon_a$ (%)	$\varepsilon_p$ (%)	$\varepsilon_q$ (%)	(1+e)	$p'$ (kPa)	$q$ (kPa)	$q\delta\varepsilon_q+p'\delta\varepsilon_p$ (kPa)	$Mp'\delta\varepsilon_q$ (kPa)	$\Gamma dS$ (N-m)
0	0.00%	0.00%	0.00%	1.51	200.0	0.0	0.0	0.0	0.0
1	0.84%	0.62%	0.63%	1.50	285.7	246.9	3.32	2.81	2.72
2	1.67%	1.13%	1.29%	1.49	336.3	394.6	4.36	3.48	4.67
3	2.51%	1.55%	1.99%	1.48	376.3	511.3	5.13	4.09	5.57
4	3.34%	1.87%	2.72%	1.48	410.8	612.1	5.78	4.67	5.86
5	4.18%	2.10%	3.48%	1.48	436.8	687.7	6.22	5.18	5.49
6	5.02%	2.29%	4.25%	1.47	457.3	747.0	6.64	5.51	6.01
7	5.85%	2.39%	5.06%	1.47	473.4	793.2	6.84	5.93	4.78
8	6.69%	2.46%	5.87%	1.47	489.8	840.5	7.19	6.19	5.30
9	7.52%	2.49%	6.69%	1.47	500.9	872.2	7.34	6.47	4.62
10	8.36%	2.48%	7.53%	1.47	509.2	895.5	7.48	6.65	4.34
11	9.19%	2.44%	8.38%	1.47	520.6	928.1	7.66	6.91	3.99
12	10.03%	2.39%	9.23%	1.47	527.6	947.6	7.82	7.01	4.24
13	10.87%	2.33%	10.09%	1.47	530.2	953.8	7.85	7.07	4.10
14	11.70%	2.25%	10.95%	1.47	533.0	960.9	7.85	7.18	3.55
15	12.54%	2.15%	11.82%	1.47	534.8	965.0	7.86	7.25	3.23
16	13.37%	2.05%	12.69%	1.48	536.9	970.2	7.90	7.28	3.31
17	14.21%	1.91%	13.57%	1.48	537.7	971.2	7.82	7.40	2.25
18	15.05%	1.81%	14.44%	1.48	533.7	958.0	7.79	7.24	2.89
19	15.88%	1.71%	15.31%	1.48	528.6	941.6	7.65	7.18	2.51
20	16.72%	1.56%	16.20%	1.48	523.5	925.2	7.43	7.22	1.12
21	17.55%	1.47%	17.06%	1.49	519.5	911.8	7.41	7.04	1.98
22	18.39%	1.34%	17.94%	1.49	516.0	900.5	7.26	7.06	1.08
23	19.22%	1.23%	18.81%	1.49	509.2	878.8	7.10	6.94	0.85
24	20.06%	1.12%	19.69%	1.49	499.4	848.5	6.86	6.79	0.36
25	20.90%	1.02%	20.56%	1.49	497.1	840.4	6.81	6.74	0.38
26	21.73%	0.93%	21.42%	1.49	493.8	829.7	6.74	6.67	0.42
27	22.57%	0.86%	22.28%	1.49	491.2	820.9	6.70	6.59	0.58
28	23.40%	0.79%	23.14%	1.50	484.7	800.5	6.53	6.51	0.13
29	24.24%	0.73%	24.00%	1.50	481.6	790.2	6.48	6.43	0.27
30	25.08%	0.68%	24.85%	1.50	475.0	769.5	6.32	6.32	0.05
31	25.91%	0.66%	25.69%	1.50	471.8	758.8	6.30	6.20	0.53
32	26.75%	0.63%	26.54%	1.50	472.2	759.0	6.29	6.22	0.40
33	27.58%	0.60%	27.38%	1.50	470.5	753.3	6.22	6.22	0.01
34	28.42%	0.58%	28.23%	1.50	469.2	748.3	6.21	6.17	0.25
35	29.25%	0.58%	29.06%	1.50	469.9	749.7	6.26	6.14	0.64
36	30.09%	0.57%	29.90%	1.50	469.9	748.7	6.23	6.15	0.43
					<b><math>\Sigma(i=1 \text{ to } 36)</math></b>		<b>243.6</b>	<b>226.9</b>	<b>88.9</b>

A graphical representation of the work balance between external work imparted on the specimen and the internal energy dissipation within the soil element is presented in Figure A.1 where the three components of Eq. A.2 are plotted as a function of  $\epsilon_a$ .

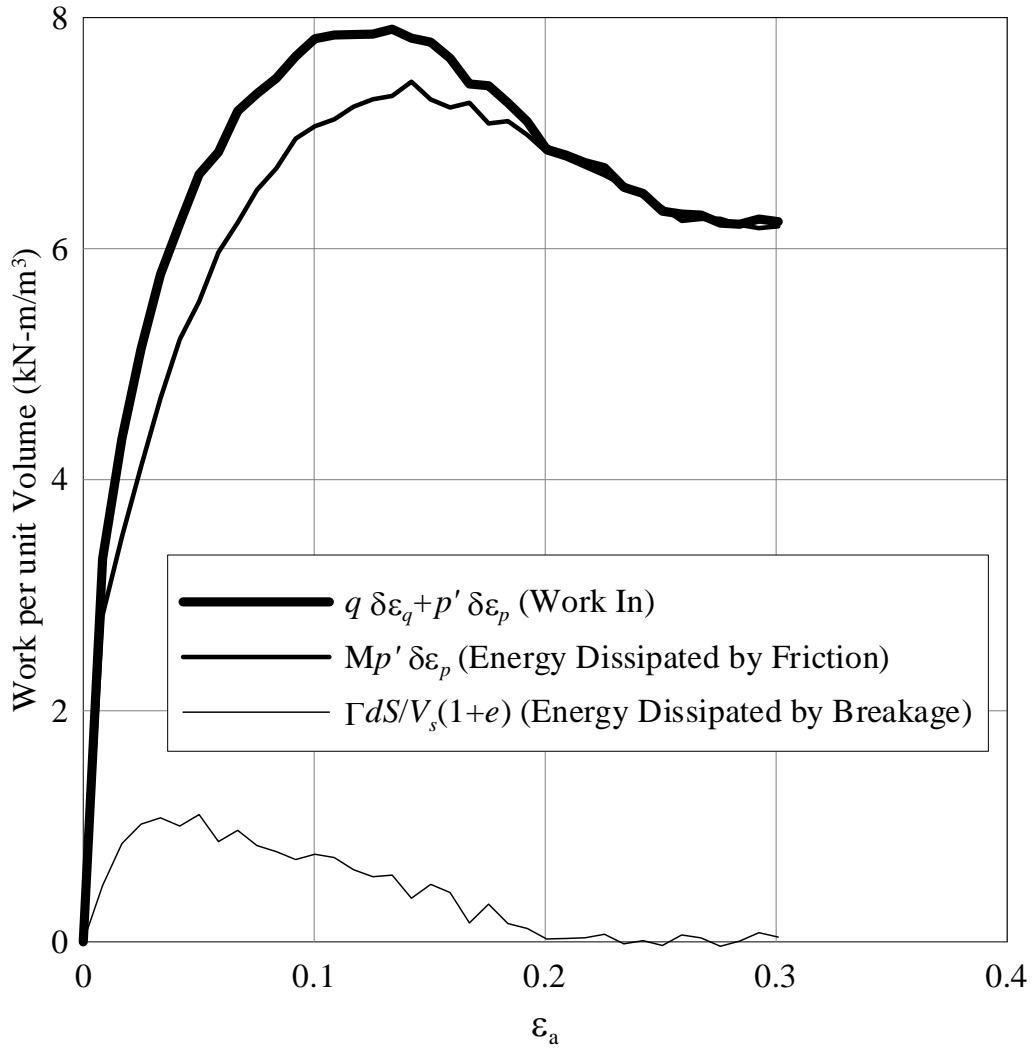


Figure A.1 Energy dissipation within the soil element according to Eq. A.2

## APPENDIX B – PARTICLE SIZE DISTRIBUTIONS

As mentioned in Chapter 4, the initial particle size distributions of triaxial specimens of unoxidized and oxidized *MWR* were modeled to be parallel to the field gradation. This led to identical initial particle size distributions between specimens of a given *MWR* type. Particle size distributions were determined after testing in order to understand the changes in the particle size distribution due to the combined effects of isotropic compression and drained axisymmetric compression. Particle size distributions before and after testing are presented in this appendix. Figures B.1, B.2, and B.3 present the particle size distributions of unoxidized specimens before and after testing, while Figures B.4, B.5, and B.6 present the particle size distributions of oxidized specimens before and after testing. Specimens are classified according to their “loose”, “medium”, or “dense” initial state in terms of  $D_R$  before drained axisymmetric compression. Values of  $D_R$  presented in Figures B.1-B.6 represent the  $D_R$  of each specimen after isotropic compression.

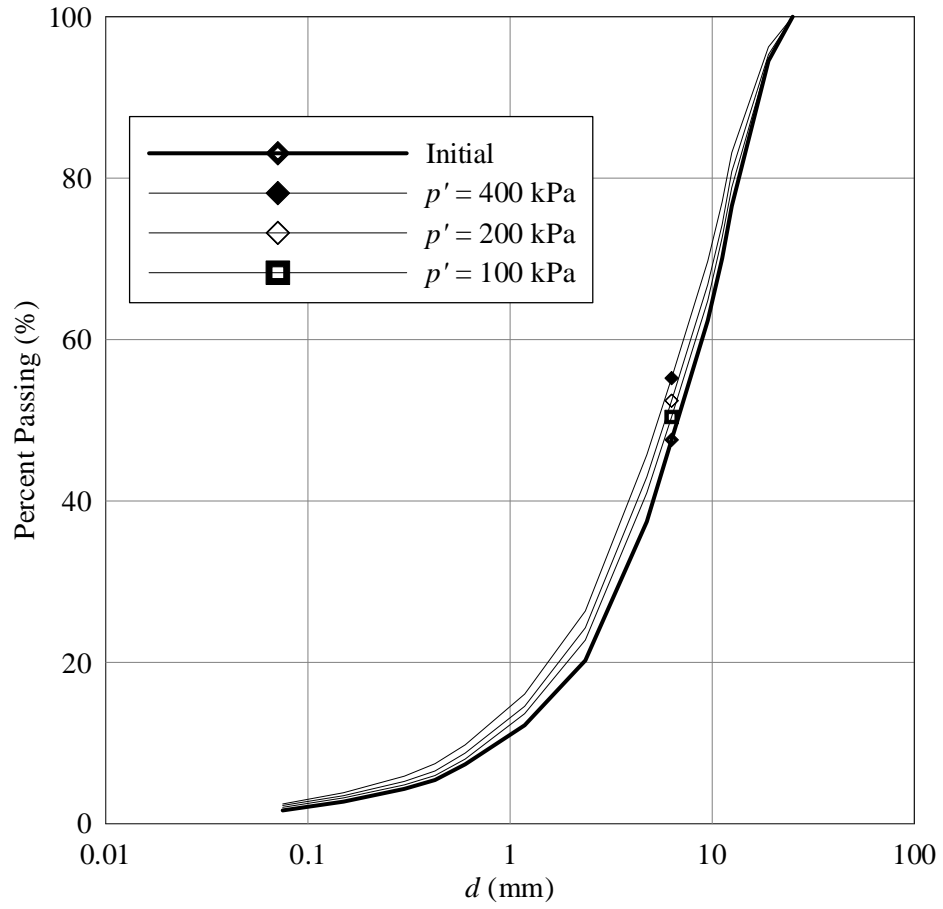


Figure B.1 Particle size distributions of unoxidized *MWR* isotropically compressed to a “loose” state ( $36\% < D_R < 48\%$ ) before drained axisymmetric compression.

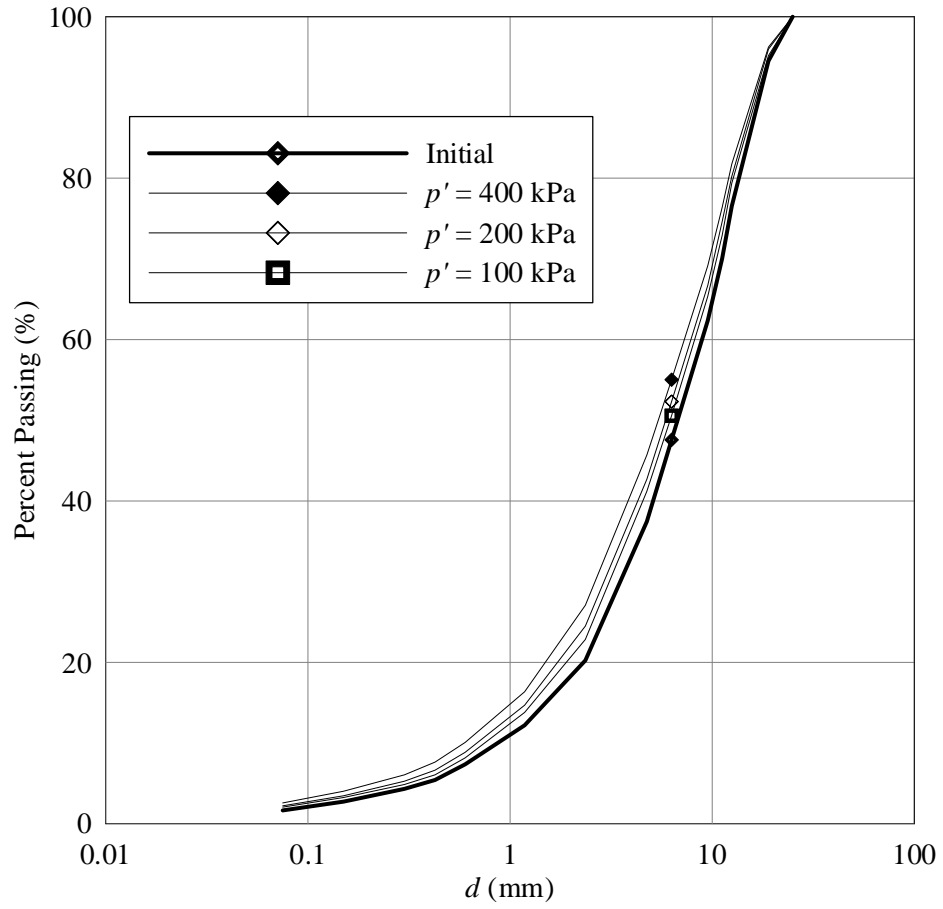


Figure B.2 Particle size distributions of unoxidized *MWR* isotropically compressed to a “medium” state ( $59\% < D_R < 65\%$ ) before drained axisymmetric compression.

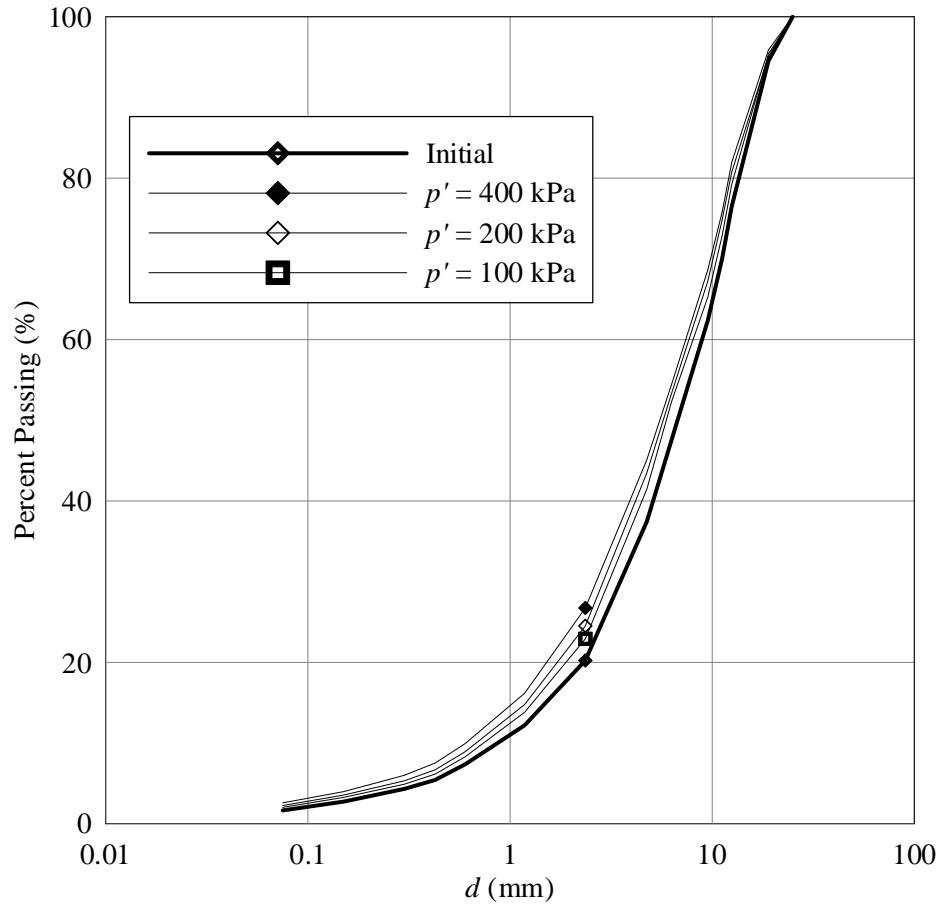


Figure B.3 Particle size distributions of unoxidized *MWR* isotropically compressed to a “dense” state ( $76\% < D_R < 85\%$ ) before drained axisymmetric compression.

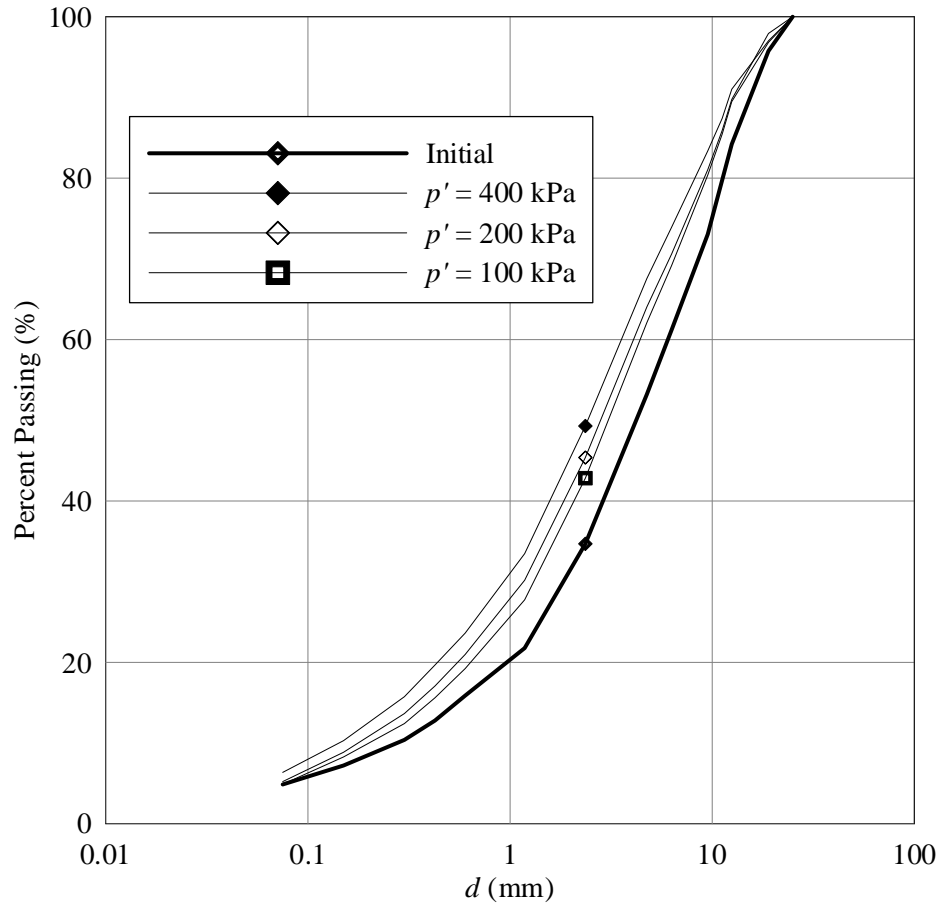


Figure B.4 Particle size distributions of oxidized *MWR* isotropically compressed to a “loose” state ( $42\% < D_R < 87\%$ ) before drained axisymmetric compression.

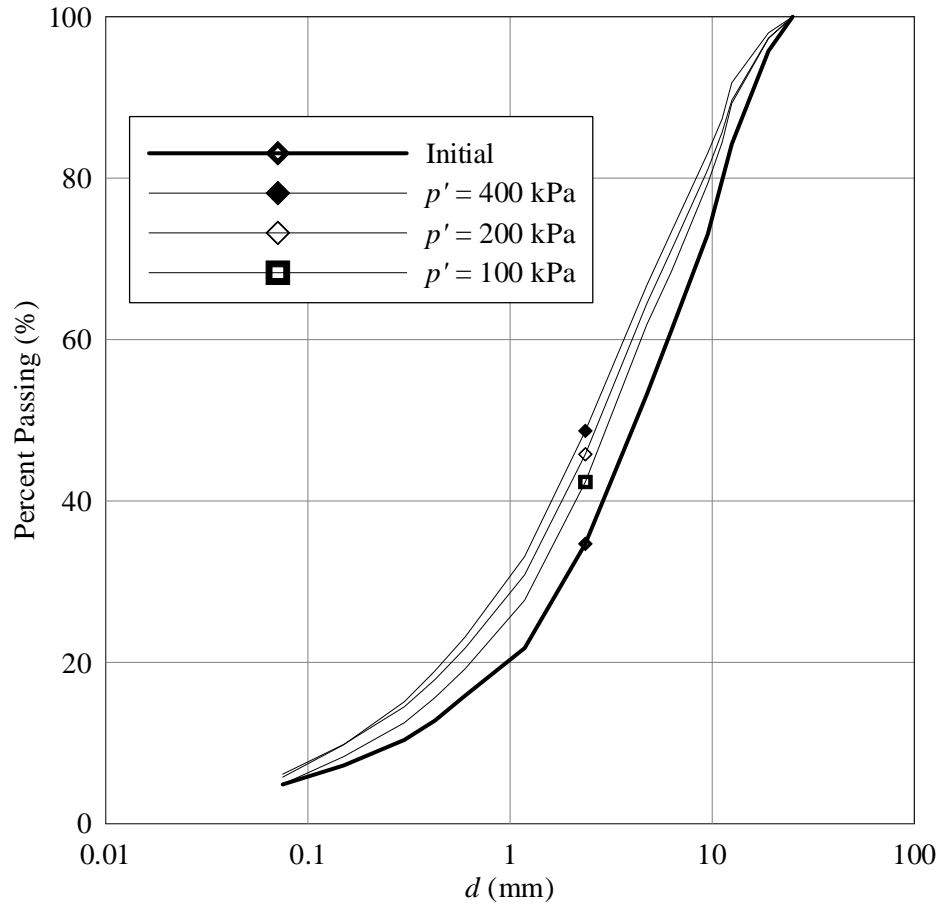


Figure B.5 Particle size distributions of oxidized *MWR* isotropically compressed to a “medium” state ( $76\% < D_R < 85\%$ ) before drained axisymmetric compression.

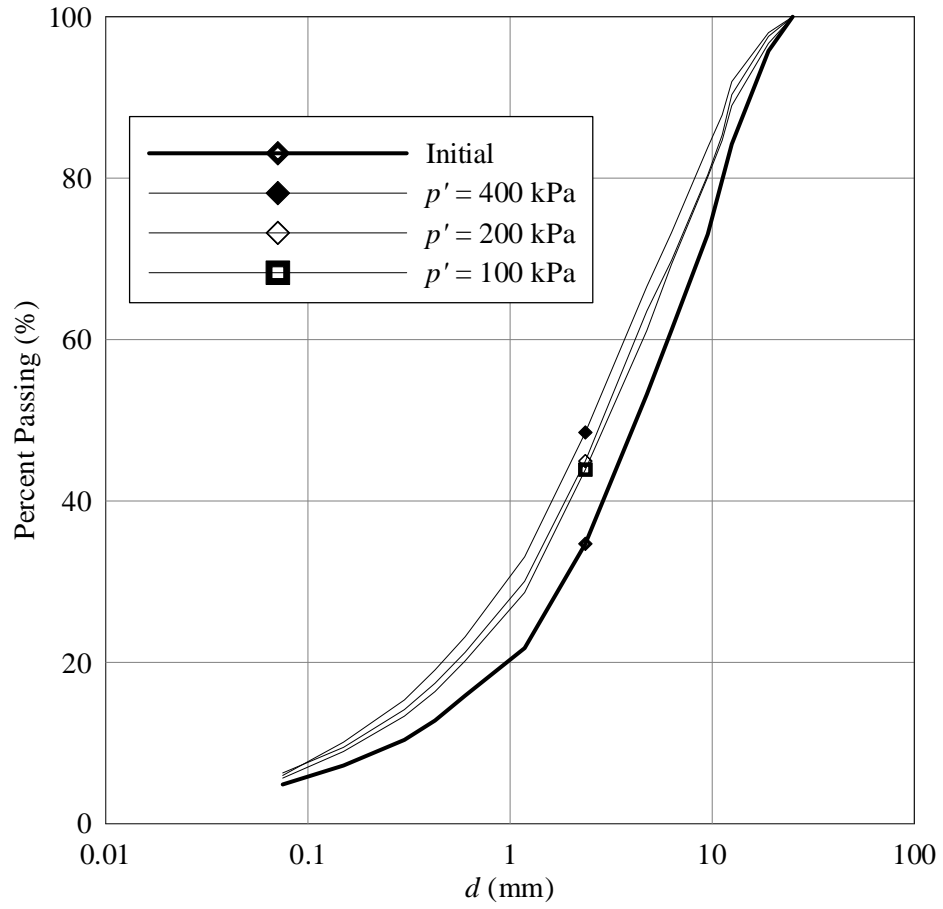


Figure B.6 Particle size distributions of oxidized *MWR* isotropically compressed to a “dense” state ( $95\% < D_R < 105\%$ ) before drained axisymmetric compression.

## APPENDIX C – FRACTAL DIMENSION

As mentioned in Chapter 3, the fractal dimension ( $D$ ) was determined for each triaxial specimen before and after testing. Determining  $D$  requires measurement or assumption of the values of the shape and volume factors ( $\beta_s$  and  $\beta_v$ , respectively) for the geomaterial in question (Please see Section 3.3 for an in depth discussion on determination of  $D$ ). Since the modeled particle size distributions of specimens before testing were constant for a given  $MWR$  type, the initial fractal dimension before testing was also constant for a given  $MWR$  material (Oxidized = 2.79, Unoxidized = 2.53). Although final values of  $D$  after testing are presented in Tables 5.3 and 5.4, the plots including the best-fit lines used to satisfy Eq. 3.23 and determine  $D$  are presented in Figures C.1, C.2, and C.3 for unoxidized specimens isotropically compressed to “loose”, “medium”, or “dense” initial state in terms of  $D_R$  before drained axisymmetric compression, respectively. Plots used to determine  $D$  for the oxidized  $MWR$  are presented in Figures C.4, C.5, and C.6 for specimens isotropically compressed to “loose”, “medium”, or “dense” initial state in terms of  $D_R$  before drained axisymmetric compression, respectively. As mentioned in Section 3.3,  $D$  may be determined as the slope of the power series trend lines in log-log space shown in Figures C.1-C.6.

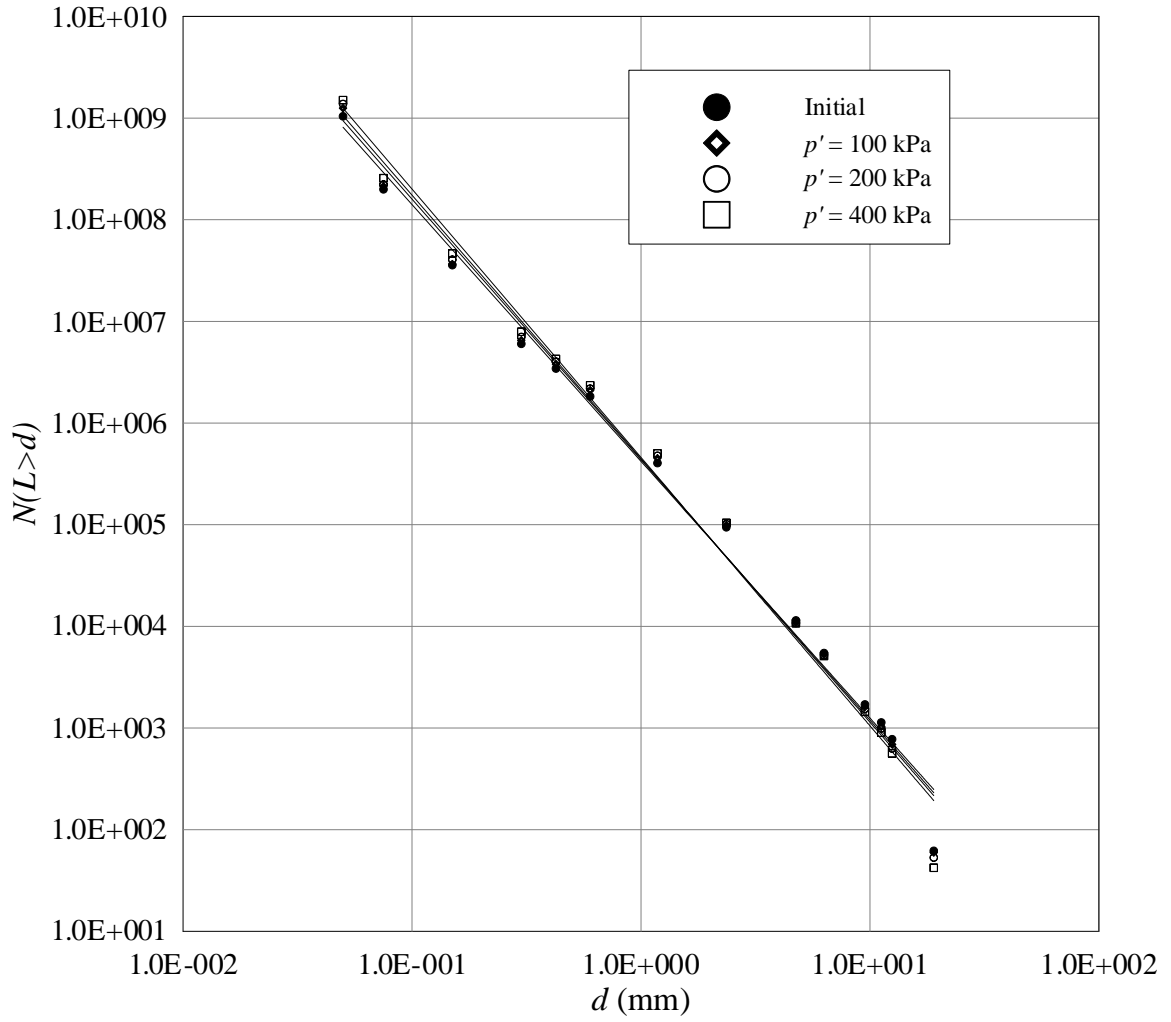


Figure C.1 Fractal dimension ( $D$ ) of unoxidized specimens isotropically compressed to a “loose” state ( $36\% < D_R < 48\%$ ) before drained axisymmetric compression.

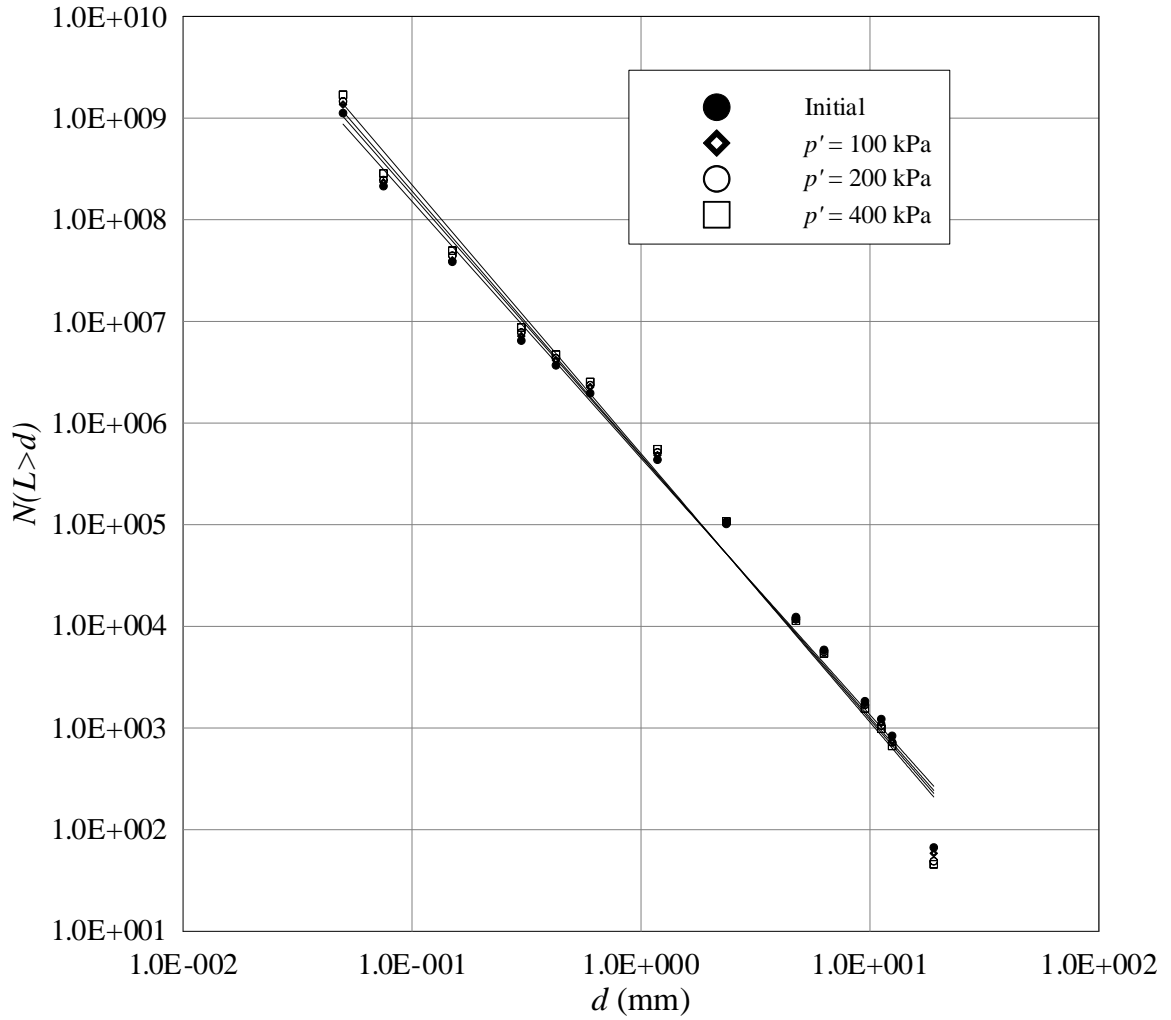


Figure C.2 Fractal dimension ( $D$ ) of unoxidized specimens isotropically compressed to a “medium” state ( $59\% < D_R < 65\%$ ) before drained axisymmetric compression.

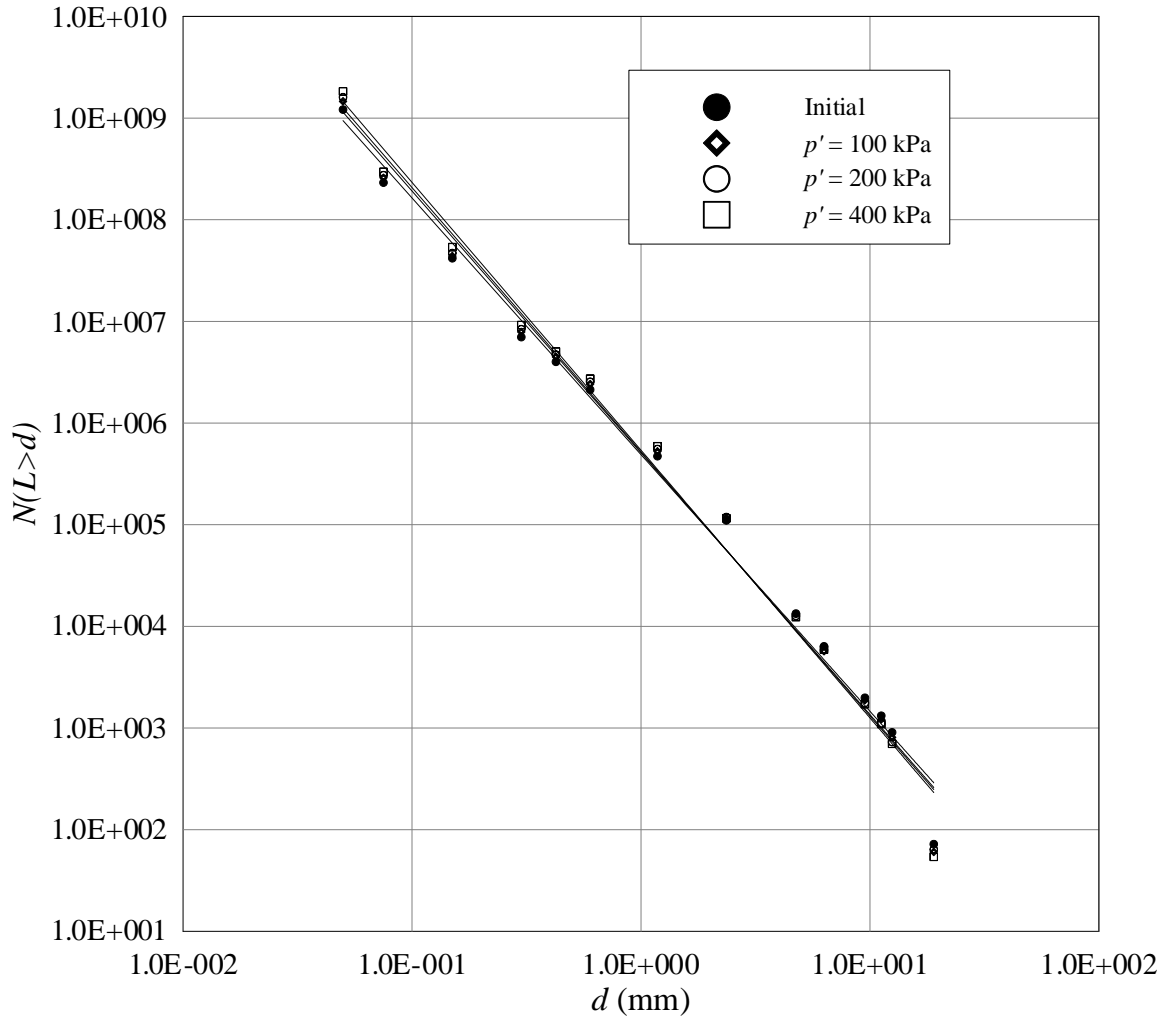


Figure C.3 Fractal dimension ( $D$ ) of unoxidized specimens isotropically compressed to a “dense” state ( $76\% < D_R < 85\%$ ) before drained axisymmetric compression.

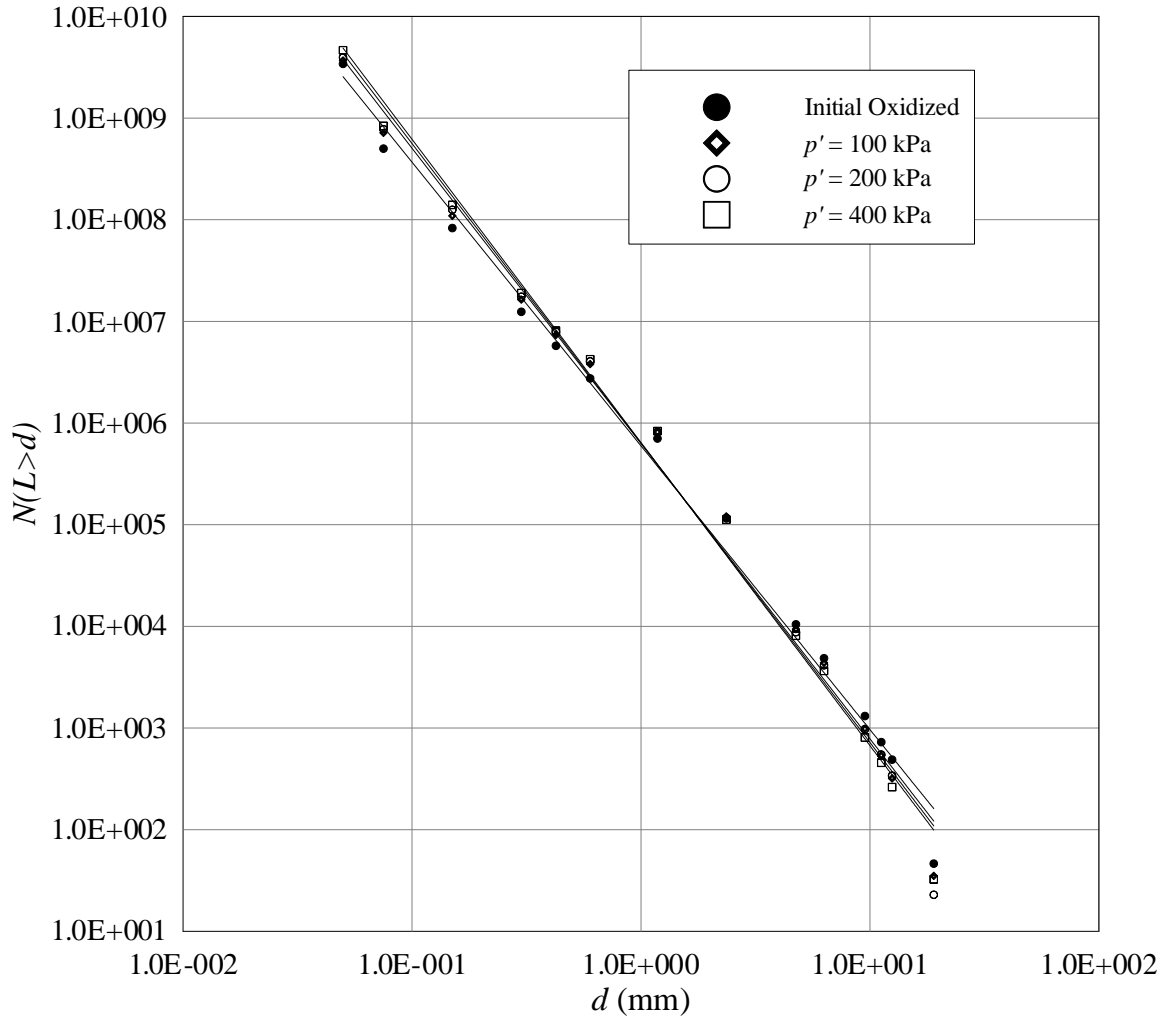


Figure C.4 Fractal dimension ( $D$ ) of oxidized specimens isotropically compressed to a “loose” state ( $42\% < D_R < 87\%$ ) before drained axisymmetric compression.

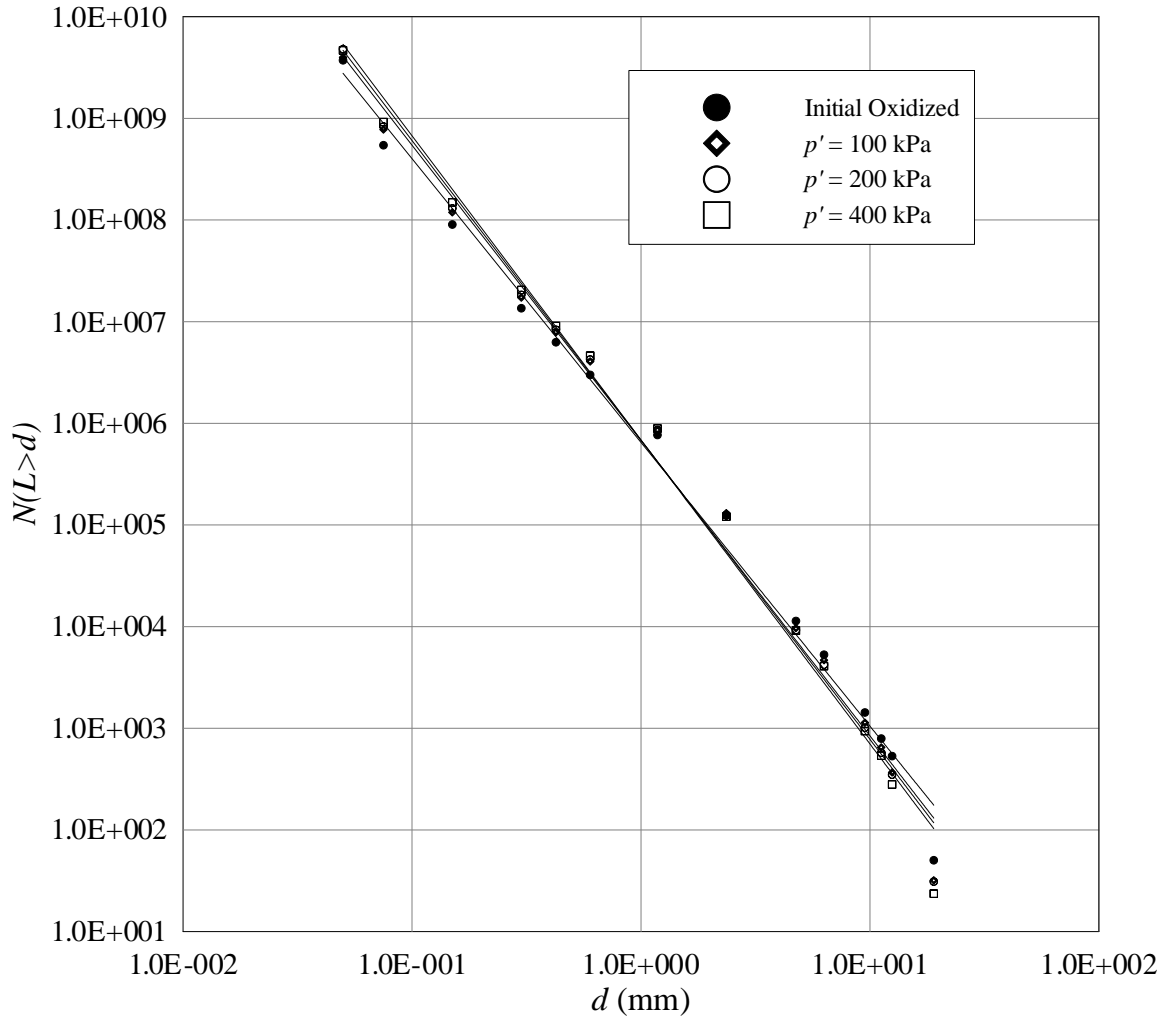


Figure C.5 Fractal dimension ( $D$ ) of oxidized specimens isotropically compressed to a “medium” state ( $76\% < D_R < 85\%$ ) before drained axisymmetric compression.

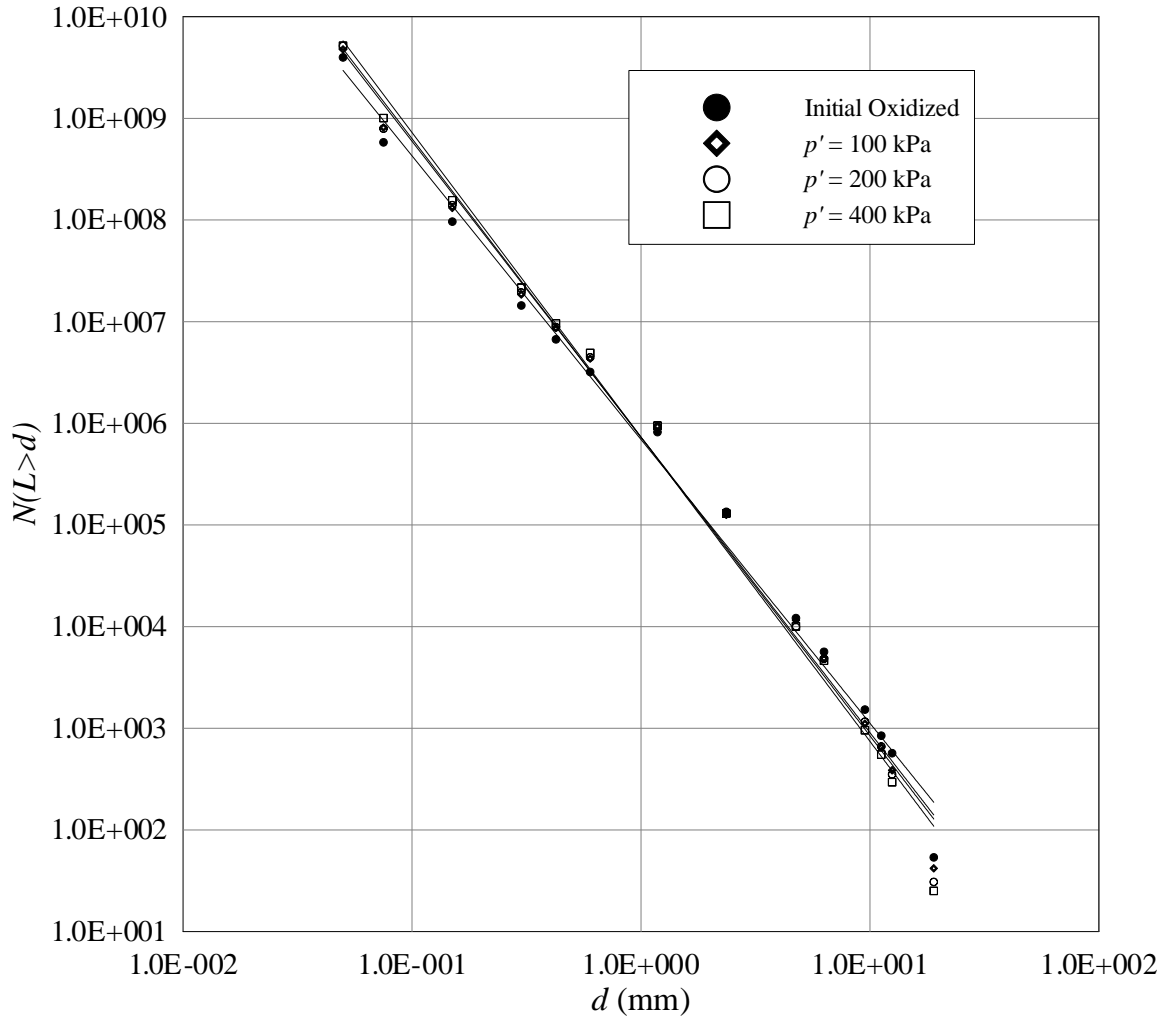


Figure C.6 Fractal dimension ( $D$ ) of oxidized specimens isotropically compressed to a “dense” state ( $95\% < D_R < 105\%$ ) before drained axisymmetric compression.

## APPENDIX D – TRANSDUCER CALIBRATION

Knowledge of the accuracy and precision of the instruments used to carry out the tests described in this manuscript is essential to understanding the reliability of the results. Before the testing program began, a thorough calibration program was carried out to ensure the highest quality results would be obtained with the equipment used. A summary of calibration results is presented in Table 4.4 while this appendix presents all data and results from this calibration program.

### D.1 Pressure Transducers

Two pressure transducers were used in all triaxial tests presented in this manuscript. The cell water pressure transducer was used to measure of total confining stress ( $\sigma_c$ ) and the pore-pressure transducer was used to measure back-pressure ( $u_b$ ) and pore-water pressure ( $u$ ) in all triaxial tests. Figures D.1 and D.2 present the relationship between signal voltage normalized by excitation voltage ( $V_s/V_e$ ) and the pressure applied by a standard pressure measurement device (See D.5.1). Table D.1 presents accuracy, resolution, excitation voltage, and calibration factors determined for each transducer.

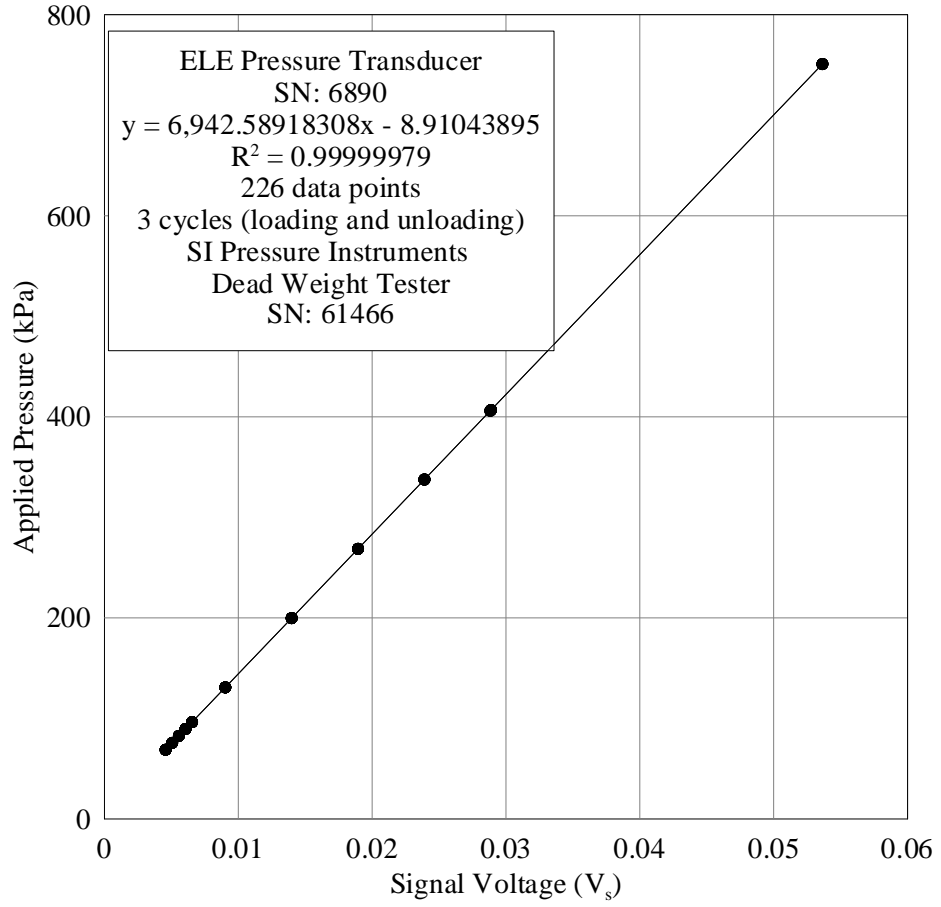


Figure D.1 Calibration plot for cell pressure transducer

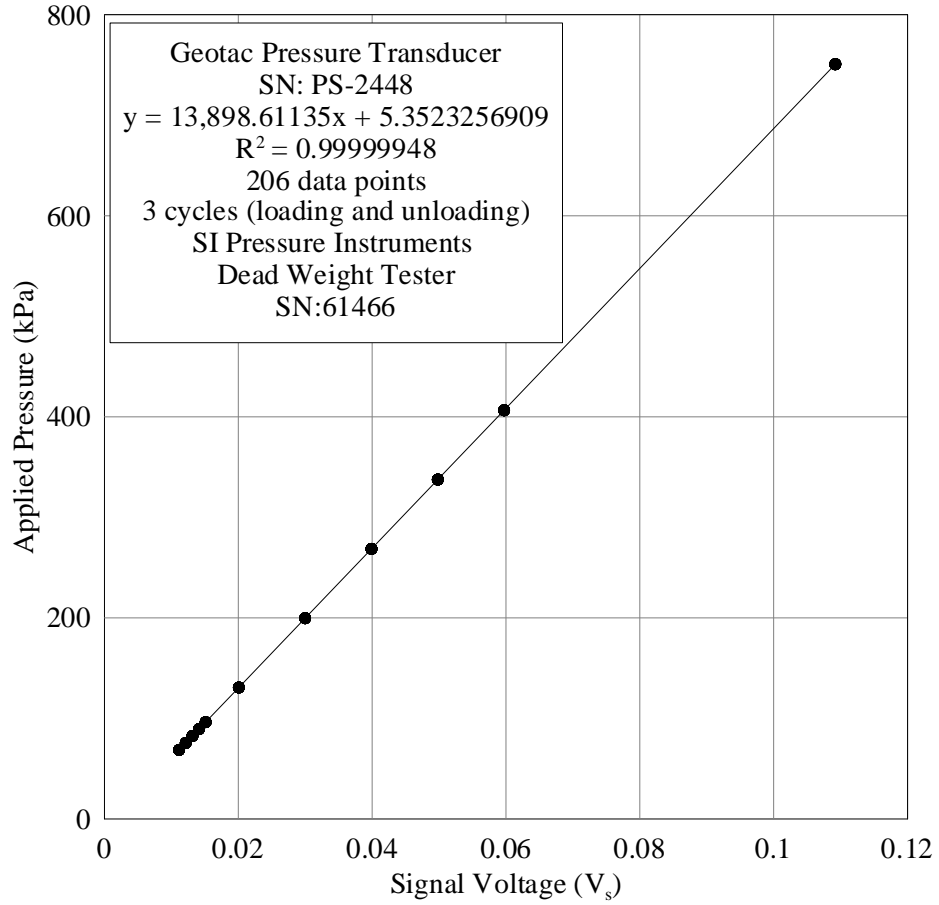


Figure D.2 Calibration plot for pore water pressure transducer

Table D.1 Pressure transducer calibration results

	Cell Pressure Transducer	Pore Water Pressure Transducer
Accuracy (%)	0.073	0.092
Resolution (kPa)	0.499	0.628
Excitation Voltage, $V_e$	9.9593	9.9593
Calibration Factor (kPa/ $V_s/V_e$ )	69280.77	138420.44

### D.2 Force Transducer

A force transducer was used to measure deviatoric loads applied to specimens during axisymmetric compression. Figure D.3 presents the relationship between signal voltage

normalized by excitation voltage ( $V_s/V_e$ ) and the load applied by a 50-kN proving ring (See D.5.2). Table D.2 presents accuracy, resolution, excitation voltage, and calibration factors determined for the load transducer by the manufacturer (Tovey Inc., Phoenix, AZ). The accuracy of the instruments used by Tovey Inc. to complete the calibration was greater than the accuracy of the proving ring used to complete the check. Therefore the calibration data from Tovey Inc. was used for all tests. This data is presented in Table D.2, while the check completed with the proving ring is presented in Figure D.3.

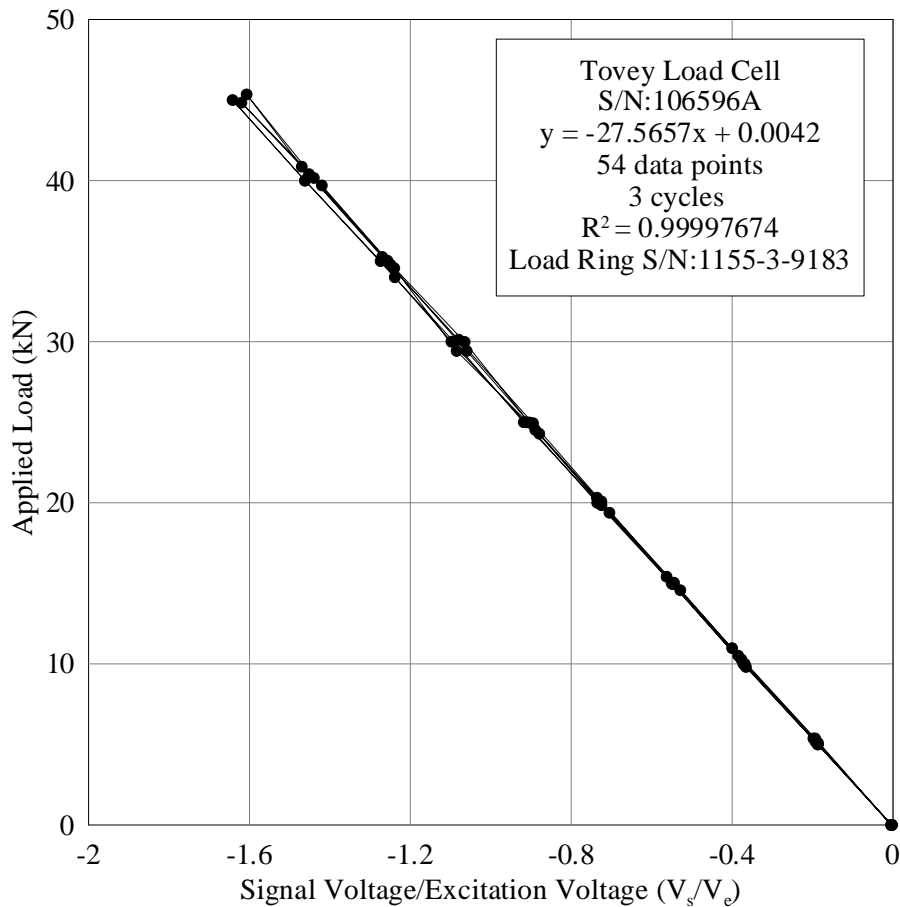


Figure D.3 Calibration plot for the deviatoric load transducer

Table D.2 Calibration Information for the Deviatoric Load Transducer

Accuracy (%)	0.59
Resolution (kN)	0.29
Excitation Voltage, $V_e$	3.00
Calibration Factor ( $\text{kN}/V_s/V_e$ )	-26.5657

### D.3 Displacement Transducer

Axial displacements were measured throughout testing for all triaxial specimens presented in this manuscript using an LVDT (linear variable differential transformer). Figure D.4 presents the relationship between signal voltage normalized by excitation voltage ( $V_s/V_e$ ) and displacement (mm) measured by a standard displacement measurement device (See D.5.3). Table D.3 presents accuracy, resolution, excitation voltage, and calibration factors determined for the load transducer.

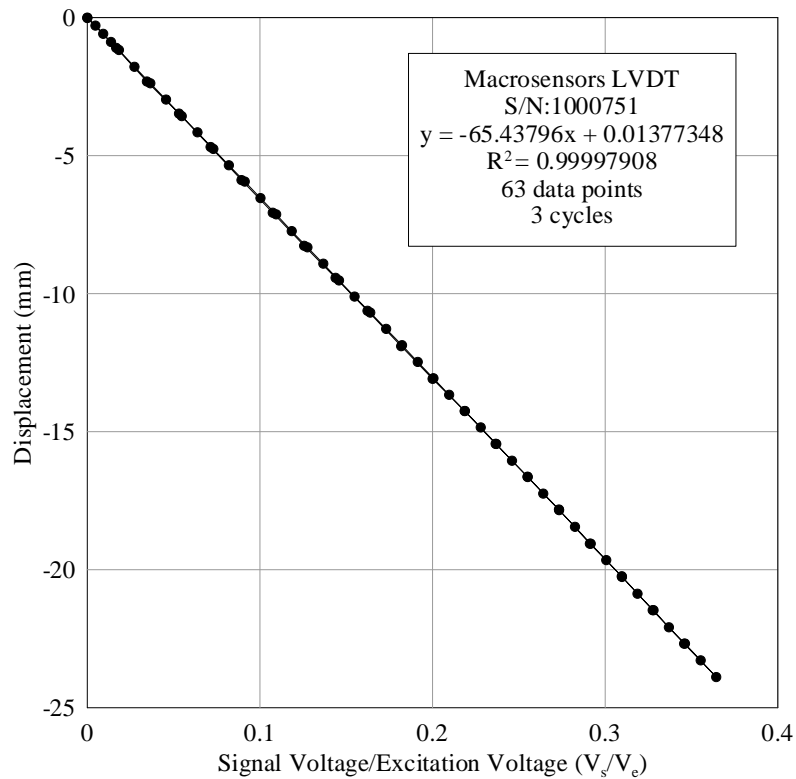


Figure D.4 Calibration plot for the axial displacement transducer

Table D.3 Calibration Information for the Axial Displacement Transducer

Accuracy (%)	0.27
Resolution (mm)	0.07
Excitation Voltage, $V_e$	10.00
Calibration Factor (mm/ $V_s/V_e$ )	65.4379

#### D.4 Volume Change Transducers

Specimen volume changes during isotropic and axisymmetric compression were measured using volume change burettes. The volumes of the burettes were calibrated at pressures of 0, 300, and 600 kPa to evaluate the effect of pressure on the volume of the burette. These tests show that change in the measured volume change due to changes in pressure applied to the burette through the air-pressure regulators described in Section 4.2.4 is less than 0.01% of a typical specimen volume (~5500 mL). Measurements were also taken over a period of 63 hours at the highest pressure levels to understand how the time dependent creep may influence volume changes in the burette due to applied pressures. This data also suggests that creep in the burettes is less than 0.01% of a typical specimen volume (~5500 mL).

#### D.5 Standard Measuring Devices Used for Transducer Calibrations

A calibration is only as good as the standard measuring device used to complete the calibration. The following standard measuring devices were used to complete the calibrations described in Sections D.1-D.4.

#### D.5.1 Standard Measuring Device for Pressure Transducer Calibration

Pressure transducer calibration was carried out using a 3500 kPa capacity dead weight tester manufactured by SI Pressure Instruments, UK. The accuracy of this dead weight tested is reported by the manufacturer as being equal 0.025%.

#### D.5.2 Standard Measuring Device for Force Transducer Calibration

Force transducer calibration was checked using a 50-kN proving ring manufactured by ELE, UK. The accuracy and resolution of this proving ring reported by the manufacturer as being equal to 0.5 kN and 1.0%, respectively. Due to the low accuracy and resolution of the load ring, an independent calibration was completed by the manufacturer of the load cell (Tovey Engineering, Phoenix, AZ) and this calibration information was compared to that determined from the 50 kN load ring. The accuracy of the instruments used by Tovey Inc. to complete the calibration were greater than the accuracy of the proving ring and therefore the calibration data from Tovey Inc. was used for all tests. This data is presented in Table D.2, while the check completed with the proving ring is presented in Figure D.3.

#### D.5.3 Standard Measuring Device for Displacement Transducer Calibration

Displacement transducer calibration was carried out using a micrometer manufactured by Mitutoyo Corporation, USA. The accuracy and resolution of this micrometer are reported by the manufacturer as being equal to 0.004 % and 0.001 mm, respectively.

#### D.5.4 Standard Measuring Device for Volume Transducer Calibration

Volume change burettes were calibrated by determining the mass of water exiting the burette for each measurement increment. The temperature of this mass of water was noted and the volume of water was determined from the specific gravity of water at the measured temperature. The volume change burettes contain 250 total increments and the measurement increments for calibration were 50 burette increments over the entire range of the burette (i.e. 5 data points for each burette). A linear best fit through these 5 data points gives a calibration factor which was used to convert a change in water level measured in terms of burette increments into a change in the volume of water in the burette. If this change in volume was measured for the back pressure burette, the measured volume change would directly correspond to a change in the volume of a saturated triaxial specimen.

#### D.6 Elastic Modulus of Triaxial Specimen Membranes

The modulus of elasticity of was determined for the two membrane types used for each triaxial specimen according to the procedure outlined in Head (1986). Table D.4 presents the relevant dimensions of the membrane strips tested. Tables D.5 and D.6 present the calibration data for the small and large membrane, respectively. Values of normal strain ( $\epsilon$ ) and normal stress ( $\sigma$ ) were determined in the direction of membrane elongation.

Table D.4 Dimensions of membrane strips used to evaluate the elastic modulus of the membranes

	Large Membrane	Small Membrane
Thickness (mm)	5.00	0.64
Width (mm)	14.95	15.02
Area (mm <sup>2</sup> )	0.075	0.019
Membrane Diameter (mm)	149.95	151.44

Table D.5 Data used to determine the modulus of elasticity for the small membrane

		Small Membrane				
		Mass Applied (g)	Length (mm)	E (kPa)	$\epsilon$ (%)	$\sigma$ (kPa)
Trial 1		0	77.58	-	0	0
		70.28	80.44	981.7	3.7	36.2
		174.28	85.32	899.6	10.0	89.7
		278.48	90.91	834.6	17.2	143.4
Trial 2		0	78.30	-	0	0
		104.20	82.55	988.6	5.4	53.7
		208.20	88.26	842.9	12.7	107.2
		278.48	91.37	859.1	16.7	143.4
Trial 3		0	76.50	-	0	0
		104.20	81.52	817.7	6.6	53.7
		174.48	85.08	1052.9	11.2	89.9
		278.48	88.41	1210.6	15.6	143.4
Trial 4		0	78.12	-	0	0
		104.20	81.62	1197.7	4.5	53.7
		208.20	87.54	889.1	12.1	107.2
		278.48	91.62	829.8	17.3	143.4

Table D.6 Data used to determine the modulus of elasticity for the large membrane

		Large Membrane				
		Mass Applied (g)	Length (mm)	E (kPa)	$\epsilon$ (%)	$\sigma$ (kPa)
Trial 1		0	87.51	-	0	0
		449.30	88.31	1339.3	0.9	12.2
		938.00	89.84	960.0	2.7	25.6
		1409.47	90.30	1204.7	3.2	38.4
		1906.57	90.80	1381.9	3.8	52.0
		2264.77	91.94	1219.1	5.1	61.7
Trial 2		0	87.90	-	0	0
		449.30	88.70	1345.2	0.9	12.2
		938.00	89.90	1123.4	2.3	25.6
		1409.47	90.74	1188.8	3.2	38.4
		1906.57	91.81	1168.0	4.4	52.0
		2264.77	92.46	1189.6	5.2	61.7
Trial 3		0	88.47	-	0	0
		449.30	89.13	1641.2	0.7	12.2
		938.00	89.64	1932.8	1.3	25.6
		1409.47	90.51	1665.7	2.3	38.4
		1906.57	91.08	1761.1	3.0	52.0
		2264.77	92.25	1444.4	4.3	61.7
Trial 4		0	88.34	-	0	0
		449.30	89.40	1020.4	1.2	12.2
		938.00	90.07	1305.2	2.0	25.6
		1409.47	90.52	1556.4	2.5	38.4
		1906.57	91.21	1599.2	3.2	52.0
		2264.77	91.89	1535.7	4.0	61.7

## LIST OF REFERENCES

- Albino, G. V. (1993) Geology and lithochemistry of the Ren gold prospect, Elko County, NV – the role of rock sampling in exploration for deep Carlin-type deposits, *Journal of Geochemical Exploration*, Vol. 51, 37-58.
- Ansal, A. M. and Erken, A. (1996) Posttest Correction Procedure for Membrane Compliance Effects on Pore Pressure, *Journal of Geotechnical Engineering*, Vol. 122, No. 1, 27-38.
- Ardua, C., Blowes, D. W., and Ptacek, C. J. (2008) Comparison of laboratory testing protocols to field observations of weathering of sulfide-bearing mine tailings, *Journal of Geochemical Exploration*, Vol. 100, 182-191.
- Ashby, M. F. and Jones, D. R. H. (1986) *Engineering Materials II*, Oxford: Pergamon Press.
- Ashby, M. F. and Jones, D. R. H. (1980) *Engineering Materials I*, Oxford: Pergamon Press.
- ASTM D 4767-04 *Standard Test Method for Undrained Triaxial Compression Test on Cohesive Soils*. ASTM International.
- ASTM D 2487-10 *Standard Practice for Classification of Soil for Engineering Purposes (Unified Soil Classification System)* ASTM International.
- ASTM D 2488-09 *Standard Practice for Description and Identification of Soils*. ASTM International.
- ASTM D 6913-04 *Standard Test Method for Particle-size Distribution of Soils Using Sieve Analysis* ASTM International.
- ASTM D 4253-00 *Standard Test Method for Maximum Index Density and Dry Unit Weight of Soils Using a Vibratory Table*. ASTM International.
- ASTM D 4254-00 *Standard Test Method for Minimum Index Density and Dry Unit Weight of Soils and Calculation of Relative Density*. ASTM International.
- ASTM D 854-02 *Standard Test Method for Specific Gravity of Solids by Water Pycnometer*. ASTM International.
- ASTM C 127-07 *Standard Test Method for Density, Relative Density and Absorption of Coarse Aggregate*. ASTM International.

- ASTM D 5731-08 *Standard Test Method for the Determination of Point Load Strength Index of Rocks and Application to Rock Strength Classifications*. ASTM International.
- Baldi, G. and Nova, R. (1984) Membrane Penetration Effects in Triaxial Testing, *Journal of Geotechnical Engineering*, Vol. 110, No. 3, 403-420.
- Barenblatt, G. I. (1962) *Advances in Applied Mechanics*, New York: Academic, Vol. 7, 55-129.
- Been, K. and Jefferies, M. G. (2000) Implications for critical state theory from isotropic compression of sand, *Geotechnique*, Vol. 50, No. 4, 419-429.
- Been, K. and Jefferies, M. G. (1985) A state parameter for sands, *Geotechnique*, Vol. 35, No. 2, 99-112.
- Billam, J. (1972) Some aspects of the behavior of granular materials at high pressures, *Stress-strain behavior of soils*, 69-80, ed. R. H. G. Parry, London: Foulis.
- Bolton, M. D., Nakata, Y., and Chen, Y. P. (2008) Micro- and macro-mechanical behavior of DEM crushable materials, *Geotechnique*, Vol. 58, No. 6, 471-480.
- Bolton, M. D. (1986) The strength and dilatancy of sands, *Geotechnique*, Vol. 36, No. 1, 65-78.
- Broch, E. and Franklin, J. A. (1972) The Point Load Strength Test, *International journal of Rock Mechanics and Mining Sciences*, Vol. 9, 669-697.
- Carraro, J. A. H., Prezzi, M., and Salgado, R. (2009) Shear Strength and Stiffness of Sands Containing Plastic and Nonplastic Fines, *Journal of Geotechnical and Geoenvironmental Engineering*, Vol. 135, No. 9, 1167-1178.
- Coop, M. R., Sorensen, K. K., Bodas Freitas, T., and Georgoutsos, G. (2004) Particle breakage during shearing of a carbonate sand, *Geotechnique*, Vol. 54, No. 3, 157-163.
- Chakraborty, T. and Salgado, R. (2010) Dilatancy and shear strength of sand at low confining pressures, *Journal of Geotechnical and Geoenvironmental Engineering*, Vol. 136, No. 3, 527-532.
- Choi, J.W. and Ishibashi, I. (1992) An Experimental Method for Determining Membrane Penetration, *Geotechnical Testing Journal*, Vol. 15, No. 4, 413-417.
- De Josselin de Jong, G. (1976) Rowe's Stress-Dilatancy Relation Based on Friction, *Geotechnique*, Vol. 26, No. 3, 527-534.

- Dendani, H., Flavigny, E., and Fry, J.J. (1988) Test for Embankment Dams: Interpretation and Validity, *Advanced Triaxial Testing of Soils and Rock*, ASTM, STP 977, 486–500.
- Essington, M. E. (2004) *Soil and Water Chemistry*, New York: CRC Press.
- Fabre, G. and Pellet, F. (2006) Creep and time-dependent damage in argillaceous rocks, *International Journal of Rock Mechanics and Mining Sciences*, Vol. 43, 950-960.
- Franke, W. A. (2009) The durability of rocks – developing a test of rock resistance to weathering, *American Journal of Science*, Vol. 309, 711-730.
- Franklin, J. A. and Chandra, R. (1972) The slake-durability test, *International Journal of Rock Mechanics and Mining Sciences*, Vol. 9, 325-341.
- Frost, R. J. (1973) Some testing experiences and characteristics of boulder-gravel fill in earth dams, *ASTM STP 523*, 207-233.
- Frydman, S., Zeitlen, J.G., and Alpan, I. (1973) The Membrane Effect in Triaxial Testing of Granular Soils, *Journal of Testing and Evaluation*, Vol. 1, No. 1, 37-41.
- Fuller and Thompson (1907) The laws of proportioning concrete, *Journal of Transportation Engineering, ASCE*, Vol. 59, 67-172.
- Fumagalli, E. (1969) Tests on cohesionless materials for rockfill dams, *Journal of Soil Mechanics and Foundations, ASCE*, Vol. 95, No. 1, 313-332.
- Golithy, C. R. (1989) Engineering properties of carbonate sands. *Ph.D. Thesis*, University of Bradford, UK.
- Grant, W. H. (1969) Abrasion pH – an index of chemical weathering, *Clays and Clay Minerals*, Vol. 17, 151-155.
- Griffith, A. A. (1920) The phenomena of rupture and flow in solids, *Philosophical Transactions of the Royal Society*, A63, 163-198.
- Hardin, B. O. (1985) Crushing of soil particles, *Journal of Geotechnical Engineering*, Vol. 111, No. 10, 1177-1192.
- Harr, M E. (1977) *Mechanics of particulate media*, McGraw Hill: New York.
- Head, K. H. (1986). *Manual of Soil Laboratory Testing* Vol. 3, Pentech Press Limited: London.

- Holtz, W. G., and Gibbs, H. J. (1956) Triaxial shear tests on pervious gravelly soils, *Journal of Soil Mechanics and Foundations Division, ASCE*, Vol. 82, No. SM1, Proceedings Paper 867, 1-22.
- Indraratna, B. and Salim, W. (2002) Modelling of particle breakage of coarse aggregate incorporating strength and dilatancy *Geotechnical Engineering*, Vol. 155, No. 4, 243-252.
- Indraratna, B., Ionescu, D., and Christie, H.D. (1998) Shear Behavior of Railway Ballast Based on Large-scale Triaxial Tests, *Journal of Geotechnical and Geoenvironmental Engineering*, Vol. 124, No. 5, 439-449.
- Indraratna, W. B., Wijewardena, L.S.S., and Balasubramaniam, A.S. (1993) Large-scale Testing of Grewacke Rockfill, *Geotechnique*, Vol. 43, No. 1, 37-51.
- Jaeger, J. C. (1967) Failure of rocks under tensile conditions, *International Journal of Rock Mechanics and Mining Sciences*, Vol. 4, 219-227.
- Jory, J (1999) Stratigraphy and host-rock controls of gold deposits in the northern carlin trend. *Gold Deposits of the Carlin Trend*, 20-34.
- Kargbo, C. M., and He, J. (2004) A simple accelerated rock weathering method to predict acid generation kinetics, *Environmental Geology*, Vol. 46, 775-783.
- Karimpour, H. and Lade, P. V. (2010) Time effects relate to crushing in sand, *Journal of Geotechnical and Geoenvironmental Engineering*, Vol. 136, No. 9, 1209-1219.
- Kendall, K., Alford, N. M., and Birchall, J. D. (1987) A new method for measuring the surface energy of solids, *Nature*, Vol. 325, No. 26, 794-796.
- Kramer, S.L., Sivaneswaran, N., and Davis, R.O. (1990) Analysis of Membrane Penetration in Triaxial Test, *Journal of Engineering Mechanics*, Vol. 116, No. 4, 773-789.
- Lade, P. V. (2007) Experimental study and analysis of creep and stress relaxation in granular materials, *Advances in the Measurement and Modelling of Soil Behavior, ASCE Geo-Denver: New Peaks in Geotechnics*, GSP 173, 1-11.
- Lade, P. V. (1994) Creep effects on static and cyclic instability of granular soils, *Journal of Geotechnical Engineering*, Vol. 120, No. 2, 404-419.
- Lade and Overton (1985) Cementation effects in frictional materials, *Journal of Geotechnical Engineering*, Vol. 115, No. 10, 1373-1387.

- LaRochelle, P., Leroueli, S., Trak, B., Blais-Leroux, L., and Tavenas, F. (1988) Observational Approach to Membrane and Area Corrections in Triaxial Tests, *Advanced Triaxial Testing of Soils and Rock*, ASTM, STP 977, 715-731.
- Lee, D. M. (1992) The angles of friction of granular fills, Ph.D. dissertation, *Cambridge University*, UK.
- Lee, K. L., and Farhoomand, I. (1967) Compressibility and crushing of granular soil in anisotropic triaxial compression, *Canadian Geotechnical Journal*, Vol. 4, No. 1, 68-86.
- Leps, T. M. (1970) Review of Shearing Strength of Rockfill, *Journal of Soil Mechanics and Foundations Division*, ASCE, Vol. 96, No. SM 4, 1159-1170.
- Leslie, D. D. (1969) Relationships between Shear Strength, Gradation, and Index Properties on Rockfill Materials *Proceedings, 7<sup>th</sup> International Conference on Soil Mechanics and Foundation Engineering*, Mexico City, 201-210.
- Lowe, J. (1964) Shear strength of coarse embankment dam materials, *Proceedings from the 8<sup>th</sup> International Congress on Large Dams*, Vol. 3, 745-761.
- Mandelbrot, B. B. (1982) *The fractal geometry of nature*, W. H. Freeman.
- Marachi, N. D., Chan, C. K., and Seed, H. B. (1972) Evaluation of Properties of Rockfill Materials, *Journal of Soil Mechanics and Foundation Engineering*, ASCE, Vol. 98, No. SM1, 95-114.
- Marachi, N. D. (1969) "Strength Characteristics of Rockfill Materials" *Seventh International Conference on Soil Mechanics and Foundation Engineering*, Mexico City, 217-224.
- Marsal, R. J. (1973) Mechanical Properties of Rockfill, *Embankment-dam Engineering*, John Wiley & Sons: New York.
- Marsal, R. J. (1969) Particle Breakage in Coarse Granular Soils, *Proceedings, 7<sup>th</sup> International Conference on Soil Mechanics and Foundation Engineering*, Mexico City, 155-166.
- Marsal, R. J. (1969) Shear Strength of Rockfill Samples, *Proceedings, 7<sup>th</sup> International Conference on Soil Mechanics and Foundation Engineering*, Mexico City, 225-234.
- Marsal, R. J. (1967) Large Scale Testing of Rockfill Materials, *Journal of Soil Mechanics and Foundation Engineering Division*, ASCE, Vol. 93, SM2, 27-43.

- McDowell, G. R. (2003) Micromechanics of creep in granular materials, *Geotechnique*, Vol. 53, No. 10, 915-916.
- McDowell, G. R. and Khan, J. J. (2003) Creep of granular geomaterials, *Granular Matter*, Vol. 5, 115-120.
- McDowell, G. R. and Harireche, O. (2002) Discrete element modeling of soil particle fracture, *Geotechnique*, Vol. 52, No. 2, 131-135.
- McDowell, G. R., Nakata, Y., and Hoyodo, M. (2002) On the plastic hardening of sand, *Geotechnique*, Vol. 52, No. 5, 349-358.
- McDowell, G. R. and Bolton, M. D. (1998) On the micromechanics of crushable aggregates, *Geotechnique*, Vol. 48, No. 5, 667-679.
- McDowell, G. R., Bolton, M. D., and Robertson, D. (1996) The Fractal Crushing of Granular Materials, *Journal of Mechanical Physics of Solids*, Vol. 44, No. 12, 2079-2102.
- Miura, N. and O-hara, S. (1979) Particle crushing of decomposed granite soil and shear stresses, *Soils and Foundations*, Vol.19, No. 4, 1-14.
- Molenkamp, F. and Luger, H. J. (1981) Modeling and minimization of membrane penetration effects in tests of granular soils, *Geotechnique*, Vol. 31, No. 4, 471-486.
- Muir-Wood, D. (1990) Soil behavior and critical state soil mechanics, Cambridge University Press: Cambridge.
- Nicholson, P. G., Seed, H. B., and Anwar, H. A. (1992) Elimination of membrane penetration compliance in undrained triaxial testing, *Canadian Geotechnical Journal*, Vol. 30, 727-738.
- Nitchiporovitch, A. A. (1969) Shearing Strength of Coarse Shell Materials *Proceedings, 7<sup>th</sup> International Conference on Soil Mechanics and Foundation Engineering*, Mexico City, 211-216.
- Oldecorp, L. A. and Alonso, E. E. (2007) Theoretical investigation of the time dependent behavior of rockfill, *Geotechnique*, Vol. 57, No. 3, 289-301.
- Ollier, C. D. (1969) *Weathering*, American Elsevier Publishing Company: New York.
- Quine, R. L. (1993) Stability and deformation of mine waste dumps in North-central Nevada, Ph.D. Thesis, University of Nevada, Reno.

- Reynolds, O. (1885) On the dilatancy of media composed of rigid particles in contact, with experimental illustrations, *Philosophical Magazine*, Series 5, Vol. 20, 469-481.
- Robertson, D. N. and Wiles, T. T. (1990) Shale durability rating system based on loss of shear strength, *Journal of Geotechnical Engineering*, Vol. 116, No. 12, 1864-1880.
- Roscoe, K. H., Schofield, A. N. and Thurairajah, A. (1963) Yield of clays on states wetter than critical, *Geotechnique*, Vol. 13, 211-240.
- Rowe, P. W. (1962) The Stress-Dilatancy Equation for an Assembly of Particles in Contact, *Proceedings of the Royal Society of London. Series A. Mathematical and Physical Sciences*, Vol. 269, No. 1339, 500-527.
- Salgado, R. (2008) *The Engineering of Foundations*, McGraw-Hill Book Company: New York.
- Salgado, R., Bandini, P., and Karim, A. (2000) Strength and Stiffness of Silty Sand, *Journal of Geotechnical and Geoenvironmental Engineering*, Vol. 126, No. 5, 451-462.
- Schofield, A. N. and Wroth, C. P. (1968) *Critical State Soil Mechanics*, McGraw-Hill Book Company: New York.
- Shaevich, R. B. (2007) Measurement of the specific free surface energy of solids. *Measurement Techniques*, Vol. 50, No. 10, 1121-1123.
- Sitharam, T. G. and Nimbkar, M. S. (2000) Micromechanical modeling of granular materials: effect of particle size and gradation, *Geotechnical and Geological Engineering*, Vol. 18, 91-117.
- Sivathayalan, S., and Vaid, V. P. (1998) Truly undrained response of granular soils with no membrane penetration effects, *Canadian Geotechnical Journal*, Vol. 35, 730-739.
- Sobek, A. A., Schuller, W. A., Freeman, J. R., and Smith, R. M. (1972) Field and laboratory methods applicable to overburdens and minesoils, *United States Environmental Protection Agency*, Report No. 600/2-78/054.
- Taylor, D. W. (1948) *Fundamentals of Soil Mechanics*, John Wiley and Sons: New York.
- Tarantino, A. and Hyde, A. F. L. (2005) An experimental investigation of work dissipation in crushable materials, *Geotechnique*, Vol. 55, No. 8, 575-584.

- Turcotte, D. L. (1986) Fractals and fragmentation, *Journal of Geophysical Research*, Vol. 91, No. B2, 921-926.
- Ueng, T. S. and Chen T. J. (2000) Energy Aspects of Particle Breakage in Drained Shear of Sands, *Geotechnique*, Vol. 50, No. 1, 65-72.
- Vallerga, B. A., Seed, H. B., Monismith, C. L., and Cooper, R. S. (1957) "Effect of Shape, Size and Surface Roughness of Aggregate Particles on the Shear Strength of Granular Materials" *ASTM, STP 212*, 63-74.
- Vaid, Y. P., Sivathayalan, S., and Stedman, D. (1999) Influence of specimen reconstitution method on the undrained response of sand, *Geotechnical Testing Journal*, Vol. 22, No. 33, 187-196.
- Varadarajan, A., Sharma, K. G., Venkatachalam, K., and Gupta, A. K. (2003) Testing and modeling two rockfill materials, *Journal of Geotechnical and Geoenvironmental Engineering*, Vol. 129, No. 3, 206-218.
- Vesic, A. S. and Clough, G. W. (1968) Behavior of granular materials under high stresses, *Journal of Soil Mechanics and Foundations ASCE*, Vol. 94, No. SM3, 661-688.
- Yudin, M. and Hughes, B. D. (1994) Surface energy of solids, *Physical Review B*, Vol. 49, No. 8, 5638-5642.
- Zeller, J. and Wulliman, R. (1957) The shear strength of the shell materials for the GoSchenenalp Dam, Switzerland, *Proceedings of the 4<sup>th</sup> Institution of the Journal of Soil Mechanics and Foundation Engineering*, London, 2, 399-404.